Aeroradiometric Measurements in the Framework of the Swiss Exercise ARM20

Gernot Butterweck, Benno Bucher, David Breitenmoser, Ladislaus Rybach,
Cristina Poretti, Stéphane Maillard, Malgorzata Kasprzak, Giovanni Ferreri,
André Gurtner, Markus Astner, Fabian Hauenstein, Marietta Straub,
Martin Bucher, Christine Harm, Gerald Scharding, Sabine Mayer

Aeroradiometric Measurements in the Framework of the Swiss Exercise ARM20

Gernot Butterweck[1], Benno Bucher[2], David Breitenmoser[1], Ladislaus Rybach[3],
Cristina Poretti[4], Stéphane Maillard[5], Malgorzata Kasprzak[1], Giovanni Ferreri[8],
André Gurtner[8], Markus Astner[6], Fabian Hauenstein[6], Marietta Straub[7],
Martin Bucher[5], Christine Harm[1], Gerald Scharding[4], Sabine Mayer[1]

1   Department of Radiation Safety and Security, Logistics Division, Paul Scherrer Institute (PSI),
Forschungsstrasse 111, 5232 Villigen PSI, Switzerland

2   Swiss Federal Nuclear Safety Inspectorate (ENSI),
Industriestrasse 19, 5201 Brugg, Switzerland

3   Institute of Geophysics, Swiss Federal Institute of Technology Zürich (ETHZ),
8092 Zürich, Switzerland

4   Swiss National Emergency Operations Center (NEOC),
3003 Bern, Switzerland

5   NBC-EOD Centre of Competence (Nuclear Biological Chemical Defense and Explosive Ordnance Disposal),
3700 Spiez, Switzerland

6   Spiez Laboratory, Austrasse, 3700 Spiez, Switzerland

7   Institut de Radiophysique, Rue du Grand-Pré 1, 1007 Lausanne, Switzerland

8   Radiation Protection Division, Federal Office of Public Health (FOPH), Schwarzenburgstrasse 157,
3003 Berne, Switzerland

Abstract

The flights of the civil part ARM20c of the exercise were performed between June 12th and June 19th, 2020. According to the alternating schedule of the annual ARM exercises, the environs of the nuclear power plants Beznau (KKB) and Leibstadt (KKL) and the nuclear facilities of the Paul Scherrer Institute (PSI) and the Zwischenlager Würenlingen AG (Zwilag) were surveyed. The measurements showed no artificial radionuclides outside of the plant premises. Additional measurements were performed between Brugg and Zurich, over the lakeshore of Lake Zurich and over the town of St. Gallen. An altitude profile over Lake Thun was used to quantify the influence of cosmic rays and the helicopter background on the measurement system. A source search exercise and an intercomparison with ground measurements was performed on Thun military training ground. A short report of the measurement results of ARM20c was placed on the NEOC website `https://www.naz.ch/` on June 19th, 2020.

The flights of the military part ARM20m of the exercise were performed from November 9th to November 13th. ARM20m focused on a fine-meshed survey of a large area north of Lake Geneva, adding to the aeroradiometric coverage of Switzerland. The radiological maps show the influence of attenuating water layers and the underlying geology on the measurement results. A flight near Mont Pelé checked on the ^{137}Cs activity remaining after the Chernobyl accident in 1986.

Several changes were bundled into the present report. The data evaluation was performed with a new software developed in the .net environment. Raw data, evaluated data and parameters used in the evaluation for each measuring area are stored together in a single text file using the ERS 2.0 format description (see PSI report 18-04). The colour gradient scale used in previous reports was replaced with a discrete colour scale defined by the Swiss Expert Group for Aeroradiometrics (FAR). The reference soil mass was switched from dry weight to wet weight, as the importance of radio-analytical laboratory measurements as reference is diminished in comparison with in-situ gamma-spectrometric ground measurements.

Contents

List of Figures

List of Tables

1 Introduction

Swiss airborne gamma spectrometry measurements started in 1986. Methodology and software for calibration, data acquisition and mapping were developed at the Institute of Geophysics of the Swiss Federal Institute of Technology Zurich (ETHZ). Between 1989 and 1993 the environs of Swiss nuclear installations were measured annually on behalf of the Swiss Federal Nuclear Safety Inspectorate (ENSI) during exercises performed as system check and drill for the operators. This schedule was changed to biannual inspections in 1994, together with an organizational inclusion of the airborne gamma-spectrometric system (ARM) into the Emergency Organization Radioactivity (EOR) of the Federal Office for Civil Protection (FOCP). The deployment of the airborne gamma-spectrometric system is organized by the National Emergency Operations Centre (NEOC). NEOC is also responsible for the recruitment and instruction of the measurement team and the operational readiness of the system. Aerial operations are coordinated and performed by the Swiss Air Force with Super Puma helicopters. The gamma-spectrometric equipment is stationed at the military airfields of Dübendorf and Payerne. The gamma-spectrometry system can be airborne within four hours. Responsibility for scientific support, development and maintenance of the aeroradiometric measurement equipment passed from ETHZ to the Radiation Metrology Section of the Paul Scherrer Institute (PSI) in 2003 in cooperation with ENSI. General scientific coordination and planning of the annual measuring flights is provided by the Expert Group for Aeroradiometrics (FAR). FAR was a working group of the Swiss Federal Commission for NBC protection (ComNBC) and consists of experts from all Swiss institutions concerned with aeroradiometry. FAR was re-organized as an expert group of the NEOC in 2008. Additional information can be found at `https://far.ensi.ch/`.

In 2018 the ARM measuring system used by the NEOC in the past exercises was replaced with the RLL (Radiometrie Land-Luft) system owned by the Swiss armed forces. Of the four systems available, under normal circumstances two systems are operated by staff of the NBC-EOD Centre of Competence (NBC-EOD) for measurement tasks with military character and two systems are assigned to NEOC for the deployment in case of civil emergencies with a radiological component. Since 2018 the scientific report includes as before measuring flights of the NEOC (ARM20c) together with measuring flights performed by the NBC-EOD (ARM20m).

This report focuses on methodological aspects and thus complements the short report of NEOC about ARM20c (available from the NEOC website `https://www.naz.ch`).

1.1 Measuring System RLL

The measuring system RLL (Radiometrie Land-Luft) used both for civil and military measurements consists of a radiation detector with four NaI(Tl) scintillation crystals with a total volume 16.8 litres, associated photo-multipliers and multichannel analysers for low level measurements and one Geiger-Müller tube and associated electronics for high-level dose rate measurement. Detectors, Geiger-Müller tube and associated electronics are installed in an aluminium case with thermal insulation foam. The detection container is mounted in the cargo bay below the centre of the helicopter. The RLL system uses position, air pressure, air temperature and radar altitude data provided by the helicopter via the internal ARINC bus. Figure 1 shows the complete system packaged for storage. The equipment control, data acquisition and storage are performed with a rugged computer working as a data server. Two further rugged redundant client computers are used as operator interface for real-time evaluation, data mapping and communication. All computers are installed in an equipment rack including a battery backed-up power supply. Both operators can operate the system with their associated client computer, display, keyboard and trackball. The additional third central display of the operator's console is mirrored on a screen in the cockpit located between both pilots and is used for information exchange with the pilots and general radiological situation awareness (figure 2). The measuring system RLL is mounted in an Aerospatiale AS 332 Super Puma helicopter (TH 06) of the Swiss Air Forces (figure 3). This helicopter has excellent navigation properties and allows emergency operation during bad weather conditions and night time.

Figure 1: Components of the RLL system. 1. Lifting platform for the installation of the detection container. 2. Floor plates and accessories case. 3. Monitors and operator console. 4. Detection container. 5. Operator seats and equipment rack.

Figure 2: Operator console of the RLL system. 1. Displays of the client computers. 2. Common display (mirrored in the cockpit). 3. Control panel with switches for power, lighting and communication and USB ports for file exchange.
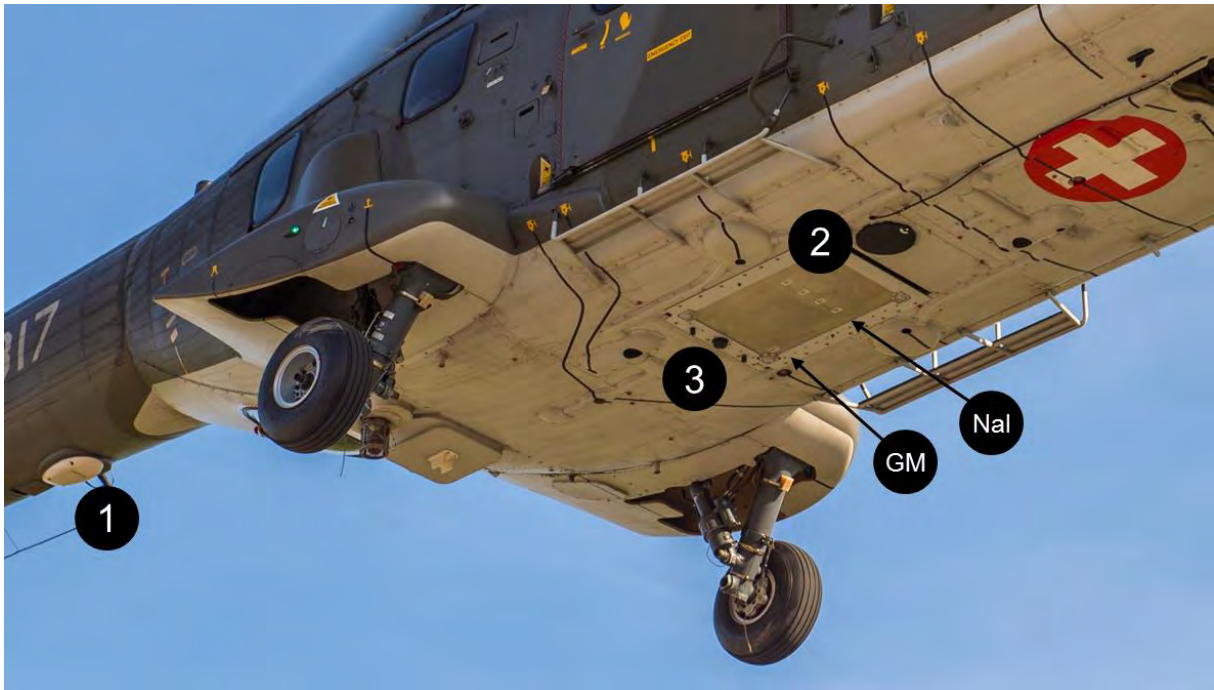
Figure 3: RLL detector mounted in the cargo bay of a Super Puma helicopter. 1. Radar altimeter. 2. Detection container marked with detector reference points. 3. UMTS antenna for data upload.

1.1.1 Quality issues

After the RLL measuring system was put into operation, quality issues with the spectrometric performance of the detectors were observed (see PSI-report 20-01). As a consequence, only one of the four available detectors was used during ARM20 after a maintenance by the manufacturer prior to exercise part ARM20c. The energy resolution of the four NaI crystals of the detector was checked twice each exercise day to test a possible influence of vibrations during the flights. During both exercise parts, no obvious deterioration of the energy resolution could be observed (Table 1). The energy resolution is the relative half-width at half maximum of the ^{137}Cs photo peak at 662 keV. Figure 4 shows the spectra measured with a ^{137}Cs source on June 19th, 10:30. A count rate per channel of zero cannot be displayed in a logarithmic scale, thus points are missing from the plots at low count rates. A quick check of spectral quality was introduced displaying the spectra of the four crystals averaged over each flight similar to figure 4.

Date and time	Energy resolution [%]			
	Crystal 1	Crystal 2	Crystal 3	Crystal 4
12.03.2020	7.5	7.6	7.4	7.9
02.06.2020	9.0	8.0	8.1	7.5
15.06.2020 7:50	8.4	7.2	8.0	8.4
15.06.2020 17:00	7.6	7.6	7.6	7.4
16.06.2020 8:00	7.9	7.8	8.8	7.2
16.06.2020 16:30	7.2	7.7	7.7	7.7
17.06.2020 8:00	7.7	7.8	8.4	7.3
17.06.2020 16:00	9.5	9.2	8.6	8.2
18.06.2020 6:30	8.9	8.5	8.1	7.7
18.06.2020 17:00	8.9	7.8	8.0	7.6
19.06.2020 7:30	9.0	8.5	8.1	7.5
19.06.2020 10:30	8.7	8.2	7.8	8.3
03.09.2020	8.2	8.0	8.5	8.2
10.09.2020	8.3	8.0	8.5	8.1
09.11.2020 9:15	7.6	8.0	8.4	7.6
10.11.2020 7:30	8.5	7.7	7.9	7.6
11.11.2020 7:30	8.1	7.3	8.1	7.6
12.11.2020 8:00	7.6	7.6	8.0	8.1
13.11.2020 7:45	7.6	7.3	7.9	7.6
13.11.2020 17:00	8.0	7.8	7.8	7.7

Table 1: Energy resolution of Detector RLL001 for the ^{137}Cs peak at 661 keV during maintenance and exercise.
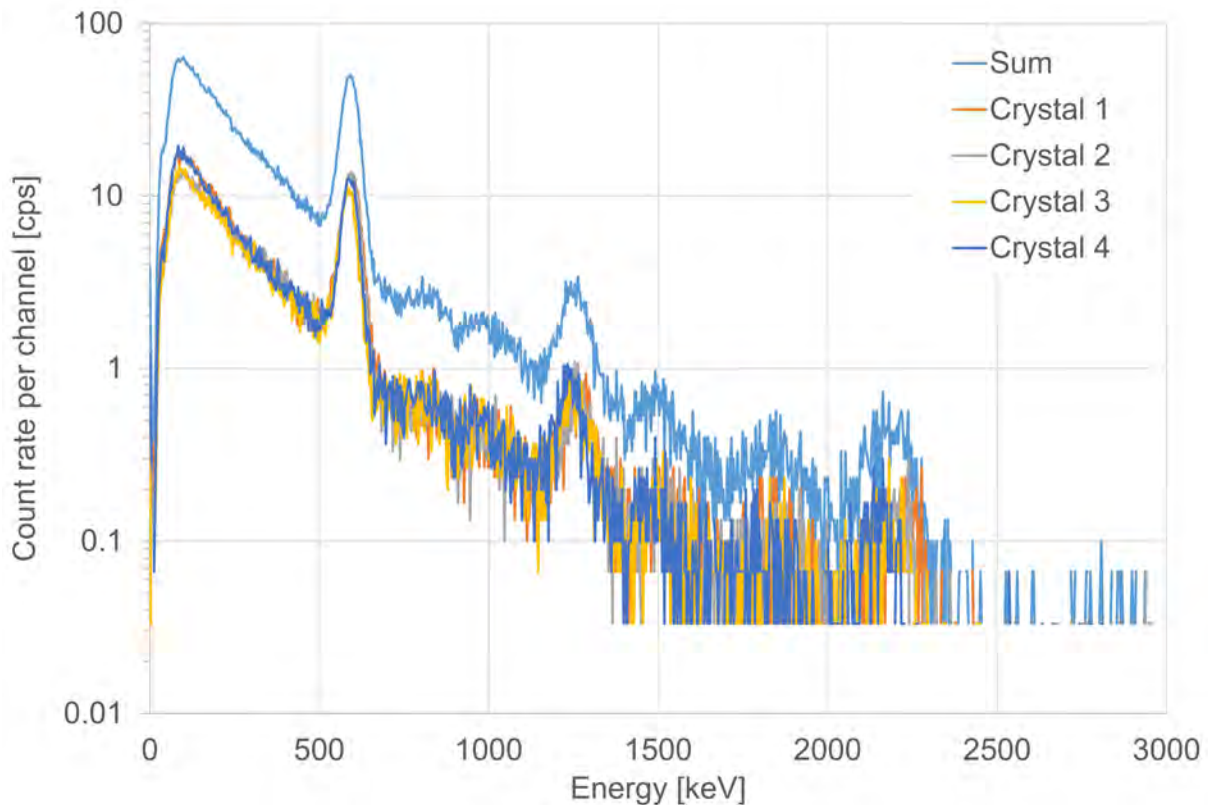
Figure 4: ^{137}Cs spectra measured with detector RLL001 on June 19th, 10:30.

Additionally, three different approaches to determine flight altitude are compared to obtain information on positioning quality. Figure 5 shows the comparison of altitude measured by the GPS system of the helicopter (PZ (geoid)), the altitude calculated from air pressure and temperature measured by the helicopter (Baroheight) and the altitude calculated by adding the measured radar height to the value of the Swiss digital elevation model DHM25 (DHM25+PH) for each point along a transversal measured in 2019. Starting with point number 800, an increasing deviation between GPS altitude and the altitudes derived from barometric pressure and digital elevation model with a sudden correction at point 1261 can be observed. This effect can be attributed to the loss of GPS satellite connections due to the mass of the adjacent mountain. The spectral and positioning quality checks are merged and visualised in an Excel spreadsheet yielding a basis for the choice of algorithms used in the following data evaluation. Figure 6 shows the corresponding diagram for a flight over Thun military training ground during this exercise, albeit with a smaller scale of the vertical axis. The deviations between measured GPS altitude (PZ) and altitude calculated from digital elevation model and radar height (DHM25+PH) visible in this magnification are associated with the measurement of radar height. Figure 7 highlights points of the flight line with DHM25+PH over 10 m higher (red) or more then 10 m lower (green) than PZ. The red points are located at the turning points, where the tilt of the helicopter is affecting the radar measurement. Green points are located over areas with trees, where the helicopter radar measures occasionally distance to the canopy instead of distance to ground. The deviation of the altitude calculated from air pressure and temperature to the measured GPS altitude shows the precision limit of the barometric method. It can be improved by calibrating the calculated barometric altitude with the measured GPS altitude averaged over a number of points (Bucher, 2001).

5
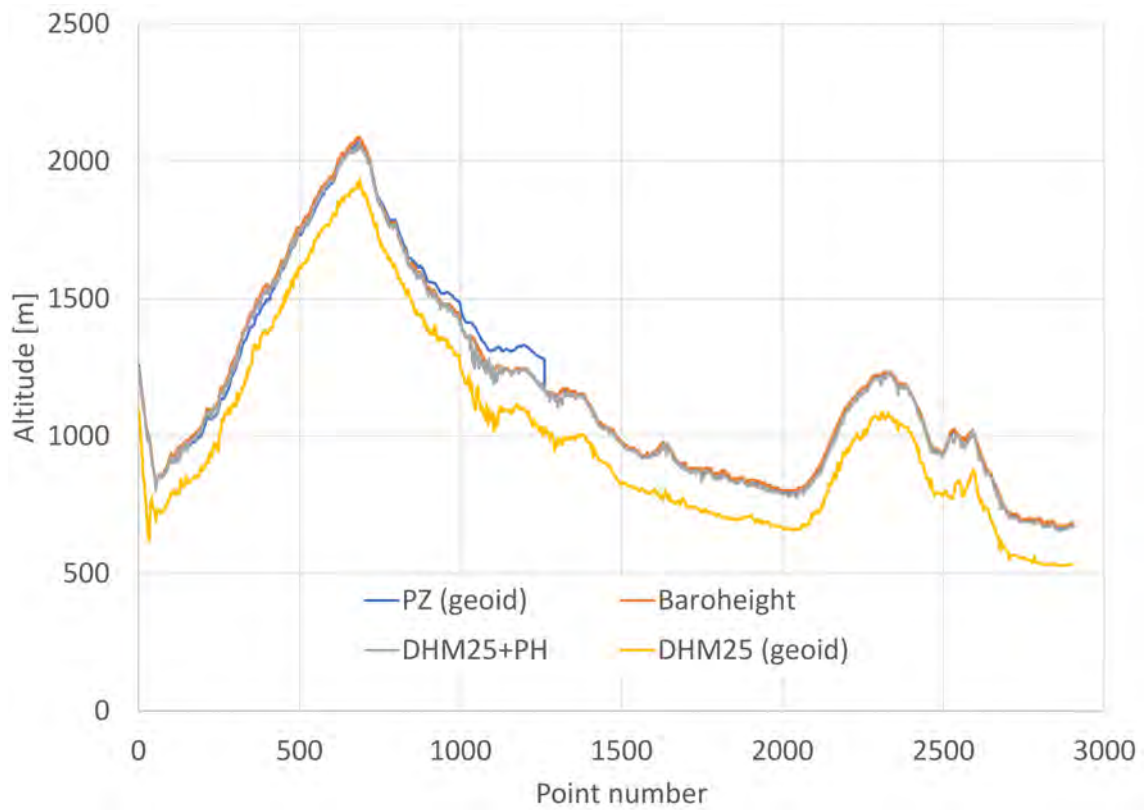
Figure 5: Comparison of three different approaches to determine flight altitude for a transversal measured in 2019.
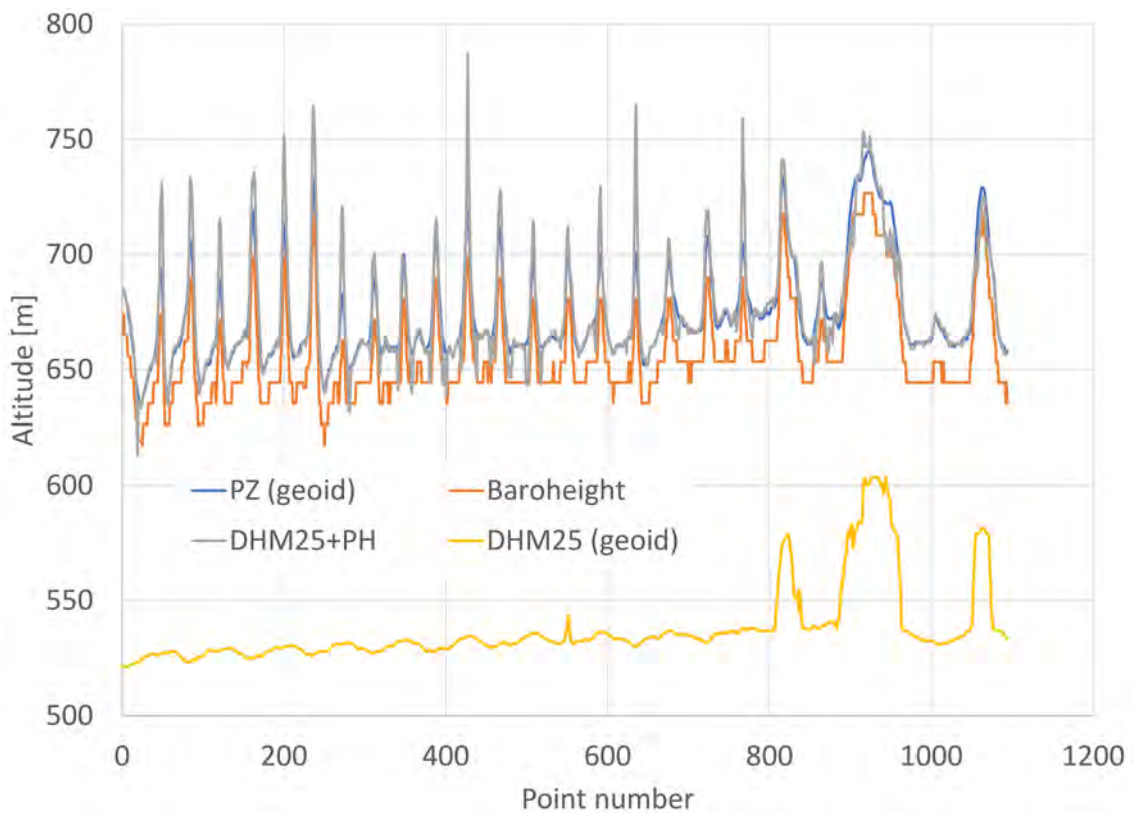
Figure 6: Comparison of three different approaches to determine flight altitude for a flight over Thun military training ground.

6
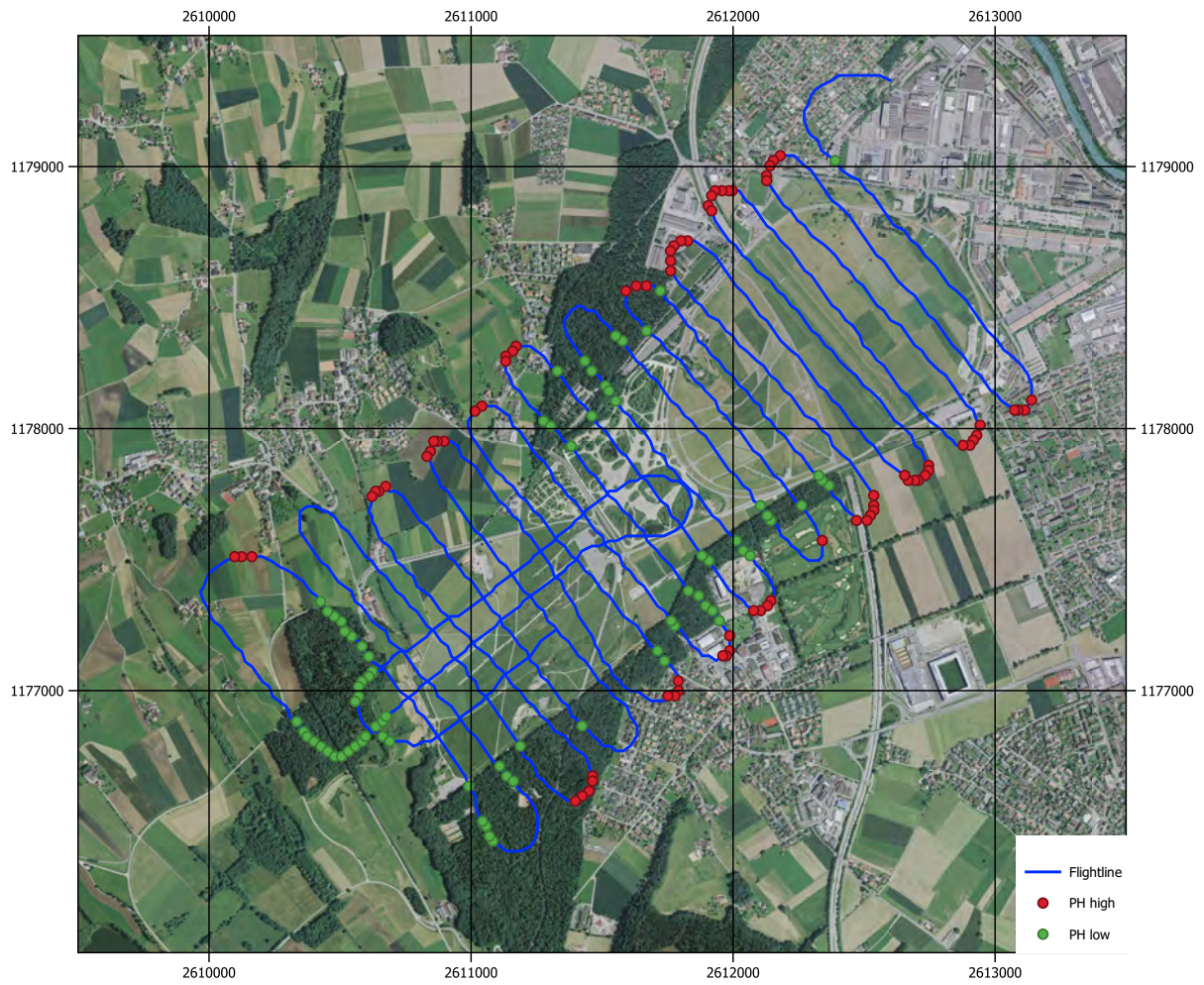
Figure 7: Location of points with altitude deviation larger 10 m for a flight over Thun military training ground. Swissimage©2020 swisstopo (JD100042)

1.2   Measuring flights

The advantage of aeroradiometric measurements lies in the high velocity of measurements in a large area, even over rough terrain. Uniform radiological information of an area is obtained from a regular grid of measuring points. This grid is composed from parallel flight lines which are 100 m to 500 m apart, depending on the scope of the measurement. The flight altitude above ground is aspired to be constant during the measuring flight. Typical values lie between 50 m and 100 m above ground. The spectra are recorded in regular time intervals of typical one second, yielding integration over 28 meters of the flight line at a velocity of 100 km/h.

1.3   Data evaluation

The data evaluation follows the methodology described in Schwarz (1991). Since 2000, the software MGS32 developed by the Research Group for Geothermics and Radiometry of the Institute of Geophysics of the Swiss Federal Institute of Technology Zurich (ETHZ) (Bucher, 2001) was used. The programming environment used for the development of this software (Add-on ESRI Mapobjects in Visual Basic 6.0) was discontinued in 2008 and 2010, respectively, making a replacement of the software necessary in the long term. Additionally, the data acquisition part of the software was rendered obsolete with the introduction of the RLL measuring system in 2018. The proprietary software for data evaluation provided by the manufacturer of the RLL system was tested sufficient for supplying data to support decisions in radiological emergencies. An outline of the algorithms used can be found in Butterweck et al., 2018. Thus, the requirement specification of the replacement software was narrowed to an evaluation performed off-line after the measurement with focus on scientific aspects and to provide a testing bed for new algorithms to evaluate airborne gamma-spectrometry data.

During 2019, the replacement evaluation software, named AGS_CH, was written in Visual Basic under the .net environment. For the reduction of development time, the new software still uses Microsoft Forms. The use of an additional mapping tool from a third party vendor was rejected to reduce dependencies of the code. The possibility of XAML-Islands in Microsoft Forms allowed to include a sufficient mapping functionality for a fast overview of results. Necessary geographic transformations and projections are programmed directly into the code. The results are exported in plain text formats readable by Geographic Information Systems (GIS), which are used for the production of final maps for publishing. Starting with the exercise of this year, the replacement software AGS_CH is used to produce the data presented in the PSI reports without further indication. Results derived with a different evaluation software are flagged accordingly in the text.

1.3.1   Determination of background and cosmic contribution

Altitude profiles over extended water bodies are used for the determination of the system background count rates and the cosmic contribution to the count rates in the different energy windows. The influence of cosmic radiation on the measured spectrum is related to a special counting channel for high energy photons. The count rate in the respective energy window is assumed as linear function of the cosmic count rate:

$$CR = CR_B + S_c CR_c \tag{1.3.1.1}$$

with:

CR: Count rate in the absence of the signal from terrestrial radionuclides [cps]
CR_B: Background count rate of detector and helicopter [cps]
CR_c: Count rate in cosmic window [cps]
S_c: Cosmic scattering factor [ ]

In the past, altitude profiles were measured keeping the helicopter for several minutes at few altitude plateaus. The counts in the different energy windows and the cosmic channel are then averaged over each altitude plateau. These averages were used to determine slope and intercept with linear regression. The quality of the linear regression was inspected visually. Figure 8 shows as an example the straight line fitted to the count rates in the Caesium and the cosmic energy window for three altitude plateaus measured over the Channel in 2002.
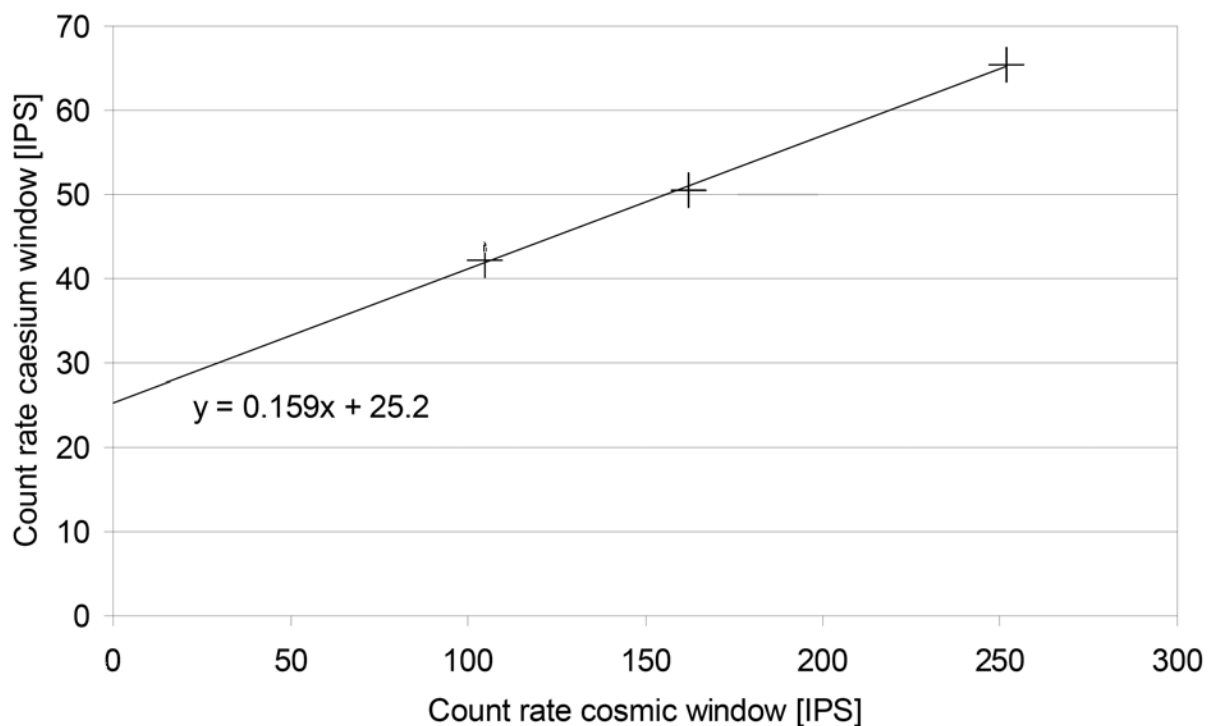
Figure 8: Count rate in Caesium energy window versus the count rate in cosmic window for different altitude plateaus.

The cosmic energy window used by the RLL system counts photons with energies between 2900 keV and 3500 keV. This cosmic window is small compared to the cosmic energy window of the previous ARM system between 3000 keV and 6000 keV. Due to the small cosmic energy window, the cosmic count rate is reduced by about a factor of four. The reduced count rate is linked with larger relative statistical scattering. The influence of the statistical fluctuations on the determined linear model is difficult to assess using the plateau method. Figure 9 shows a scatter-gram of the count rate in the total energy window versus the count rate in the cosmic energy window measured over Lake Thun during this exercise. As a first estimate of the uncertainties associated with each point, Poisson statistics can be used, taking a measuring time of one second into account. Accordingly, a count rate of 25 cps is associated with a count of 25 and a statistical uncertainty of 10 at a 95% confidence

level.

Four different methods to determine a linear model were applied to the point data. All methods have some basic statistical quantities in common, formulated in a general notation:

$$\bar{x} = \frac{1}{n} \sum_{i=1}^{n} x_i \qquad (1.3.1.2)$$

with:

$\bar{x}$:   Arithmetic average of x_i values

n: Number of points

x_i: x-value of point i

$$\bar{y} = \frac{1}{n} \sum_{i=1}^{n} y_i \qquad (1.3.1.3)$$

with:

$\bar{y}$:   Arithmetic average of y_i values

y_i: y-value of point i

$$s_{xx} = \frac{1}{n-1} \sum_{i=1}^{n} (x_i - \bar{x})^2 \qquad (1.3.1.4)$$

with:

s_{xx}:   Variance of x_i values

$$s_{yy} = \frac{1}{n-1} \sum_{i=1}^{n} (y_i - \bar{y})^2 \qquad (1.3.1.5)$$

with:

s_{yy}:   Variance of y_i values

$$s_{xy} = \frac{1}{n-1} \sum_{i=1}^{n} (x_i - \bar{x})(y_i - \bar{y}) \qquad (1.3.1.6)$$

with:

s_{xy}:   Covariance of x_i and y_i values

The very simplest linear interpretation of the data would be setting the background (intercept) in the respective energy window to zero ($\beta_0 = 0$). The slope of the straight line β_1 calculates thus to the ratio of averages

$$\beta_1 = \frac{\bar{y}}{\bar{x}} \qquad (1.3.1.7)$$

with:

β_1:   Slope of straight line

If a non-zero intercept is considered, representing in our application a signal due to radionuclides in detector and helicopter, standard linear regression can be applied:

$$\beta_1 = \frac{s_{xy}}{s_{xx}} \tag{1.3.1.8}$$

$$\beta_0 = \bar{y} - \beta_1 \bar{x} \tag{1.3.1.9}$$

The standard linear regression analysis still implies x_i values without uncertainties. A step further to a realistic estimate of slope and intercept would be using the orthogonal linear regression, where the straight line is optimised for minimal orthogonal distances from the line to the points x_i, y_i. The slope and intercept for the orthogonal regression are calculated by

$$\beta_1 = \frac{s_{yy} - s_{xx} + \sqrt{(s_{yy} - s_{xx})^2 + 4s_{xy}^2}}{2s_{xy}} \tag{1.3.1.10}$$

$$\beta_0 = \bar{y} - \beta_1 \bar{x} \tag{1.3.1.11}$$

In the orthogonal regression, the variation scale in both directions is assumed identical, which is not the case in our application. To take into account different variance scales, Deming regression uses the picture of true values of x and y, which are superposed with stochastically distributed measurement errors ϵ and η. Defining the ratio of variances of these measurement errors

$$\delta = \frac{s_{\epsilon\epsilon}}{s_{\eta\eta}} \tag{1.3.1.12}$$

with:

$s_{\epsilon\epsilon}$:   measurement error variance in x-direction
$s_{\eta\eta}$:   measurement error variance in y-direction
δ: ratio of measurement error variances

yields slope and intercept to

$$\beta_1 = \frac{s_{yy} - \delta s_{xx} + \sqrt{(s_{yy} - \delta s_{xx})^2 + 4\delta s_{xy}^2}}{2s_{xy}} \tag{1.3.1.13}$$

$$\beta_0 = \bar{y} - \beta_1 \bar{x} \tag{1.3.1.14}$$

In our application, both x and y values are counts during one second cycle time. Thus the measurement error variance in both directions can be assumed according to Poisson counting statistics, which yields

$$\delta = \frac{\bar{y}}{\bar{x}}. \tag{1.3.1.15}$$

Figure 9 shows a scattergram of the count rate in the total energy window in dependence on the cosmic count rate for an altitude profile measured over Lake Thun during this exercise. The different linear models derived from these values are included. The red dotted line shows the linear regression with zero intercept according to equation 1.3.1.7. The standard linear regression with non-zero intercept (equations 1.3.1.8 and 1.3.1.9) is depicted as

green dotted line. The orthogonal regression (equations 1.3.1.10 and 1.3.1.11, orange dotted line) and the Deming regression (equations 1.3.1.13, 1.3.1.14 and 1.3.1.15, blue dotted line) are closer to the simple linear regression with zero intercept compared to the standard linear regression. The large differences between the different regression approaches indicates a masking of the linear dependence due to large statistical variations of the measured signals.

Standard, orthogonal and Deming regression yield much closer results for the altitude profile measured over Lake Neuchâtel in 2019 (Figure 10). This profile covered a larger altitude range from 516 m to 2972 m compared to the profile over Lake Thun between 651 m and 1776 m, providing a smaller ratio of statistical variation to the assumed linear dependency. Unfortunately, the slope for the Thorium energy window leads to negative intercepts of the Deming regression. The ratio of error variances δ is lowest for the Thorium energy window, probably causing an overestimation of the slope. The underlying error variances were assumed equal to the average window counts in one second following Poisson statistics. An alternative determination of an empirical estimate for δ dependency on the count rates can be considered for the future, when more than three altitude profiles with sufficient altitude range are available. As a first measure to avoid negative intercepts, δ-values were limited to values above 1, averting slopes steeper than those derived from orthogonal regression.

Figure 9: Count rate in total energy window versus the count rate in cosmic window for altitude profile B measured over Lake Thun in 2020.
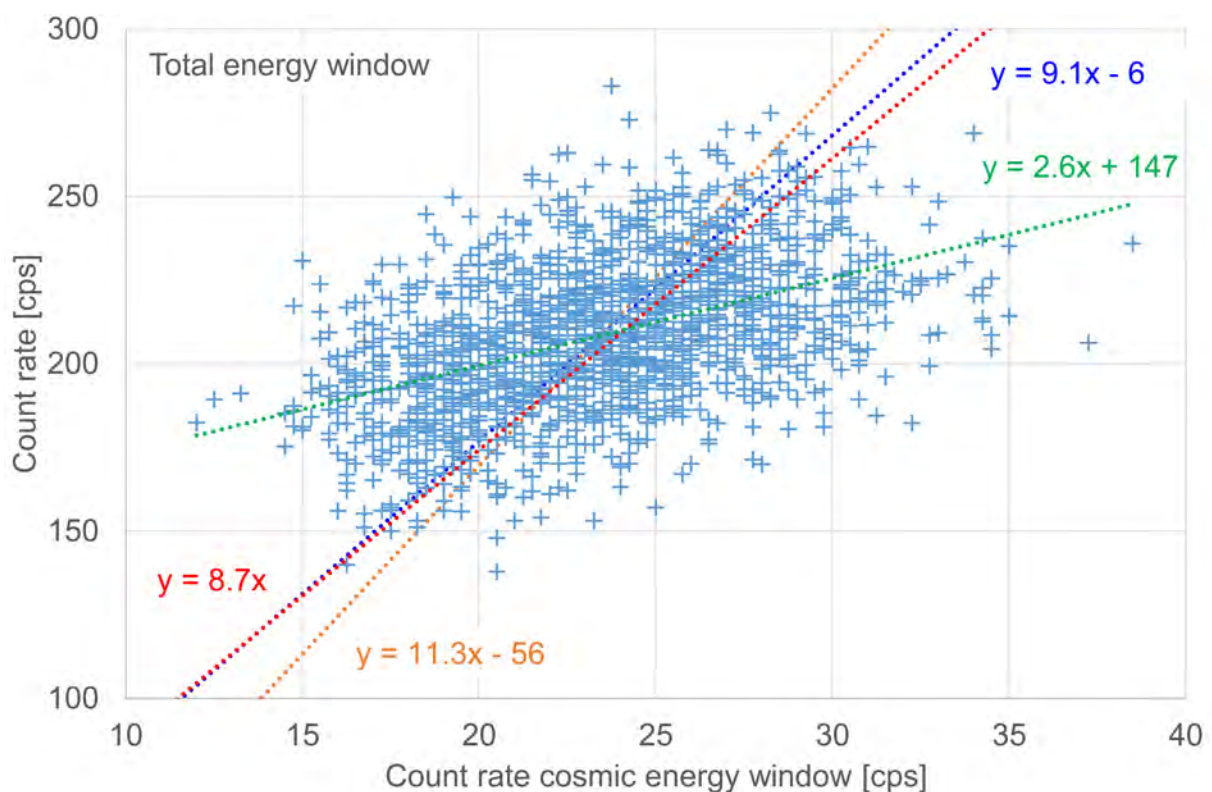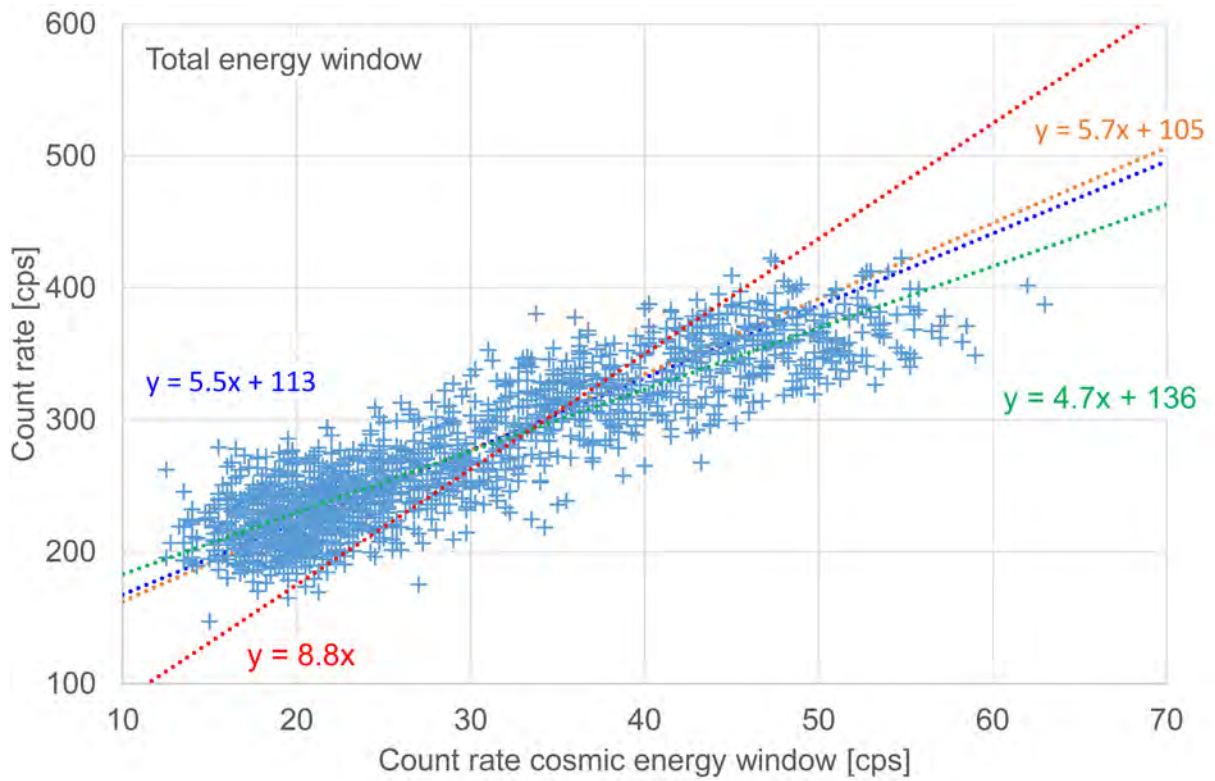
Figure 10: Count rate in total energy window versus the count rate in cosmic window for an altitude profile measured over Lake Neuchâtel in 2019.
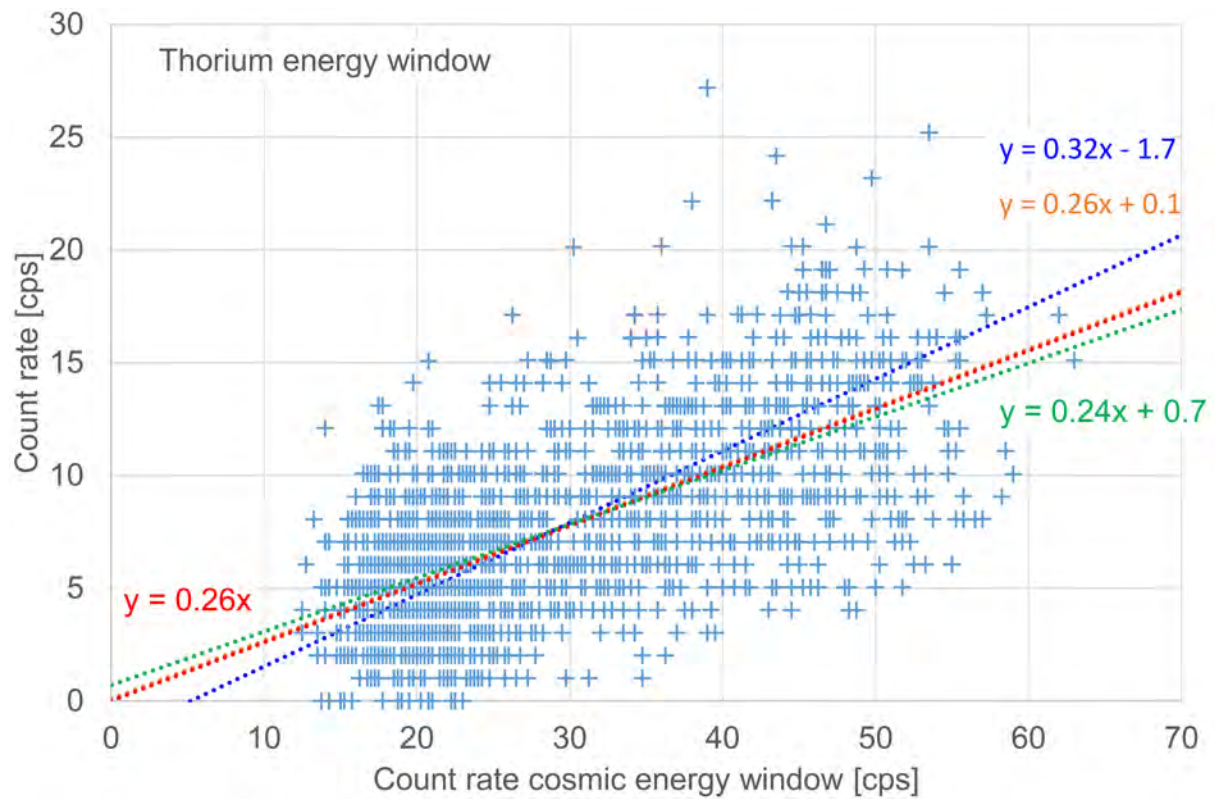

Figure 11: Count rate in Thorium energy window versus the count rate in cosmic window for an altitude profile measured over Lake Neuchâtel in 2019.

Three altitude profiles measured with the RLL system had more than 2 km between lowest and highest altitude and were selected to determine the slope of the cosmic correction using Deming regression with δ limited to values above 1 (Table 2). The determination of the uncertainty of the slope derived with Deming regression is not trivial. As the three selected altitude profiles can be assumed to have additional to the stochastic variations some unknown systematic differences, the standard deviation over the slopes of the three altitude profiles is given in Table 2 as an estimate of uncertainty.

The slope averaged over the three available altitude profiles with sufficient altitude range is used in a second step to calculate according to equation 1.3.1.9 the background count rates listed in Table 3 for each energy window. The use of unified slopes for all altitude profiles reduces the variation of background count rates. Nevertheless, the remaining variation cannot be neglected in the data evaluation. Assignment of higher background count rates to an individual RLL system or helicopter failed as detector-helicopter combinations have been repeated only once for the reported altitude profiles. A further possible source of the large variation could be the influence of airborne radon progeny. Attempts to derive an appropriate correction from the altitude profiles (see PSI-reports 19-01 and 20-01) did not yield convincing results up to now. In consequence, the background count rates are determined annually from flights over extended water bodies near the main measuring areas for the individual detector-helicopter combination. The background and slope for the current exercise are stored under identifiers ISWB_winname and ISWC_winname in the header section of all ERS 2.0 files (section 6) generated for ARM20 data.

Parameter	Lake Zug 2017	Lake Geneva 2018	Lake Neuchâtel 2019	Average	Standard deviation
Maximum Altitude [m]	2858	2859	2972	-	-
Minimum Altitude [m]	500	458	516	-	-
Altitude range [m]	2358	2401	2456	-	-
Average cosmic count rate [cps]	25.5	24.8	29.2	-	-
Energy window	Slope for cosmic correction				
Total	6.0	5.2	5.5	5.6	0.4
Potassium	0.31	0.28	0.31	0.30	0.02
Uranium	0.25	0.21	0.23	0.23	0.02
Thorium	0.29	0.29	0.26	0.28	0.02
Caesium	0.69	0.45	0.60	0.58	0.12
Cobalt	0.70	0.60	0.66	0.65	0.05
SDI	4.5	4.0	4.1	4.2	0.3

Table 2: Determination of the slope for cosmic correction from three altitude profiles.

Energy Window	Total	Potassium	Uranium	Thorium	Caesium	Cobalt	SDI
Altitude profile	Background count rate [cps]						
Lake Neuchâtel 2016	135	8.1	6.1	1.6	22	12	92
Lake Zug 2017	62	5.8	2.4	0.2	9.7	4.7	42
Lake Geneva 2018	153	11	7.5	0.7	24	17	104
North Sea 2018	38	4.8	0.6	0.1	5.8	2.5	24
Lake Neuchâtel 2019	111	9.0	5.4	−0.6	18	12	74
Lake Thun 2020A	78	6.4	3.7	0.0	12	7.0	51
Lake Thun 2020B	78	6.3	3.4	−0.1	13	7.2	52

Table 3: Determination of the background count rate.

1.3.2 Characterisation of spectral cross-talk

Several factors can lead to registering a photon emitted by a radionuclide on or in the ground in the energy window associated with a different radionuclide:

- Photons emitted from the soil are scattered due to the Compton effect in the soil, in buildings, in vegetation, in the air between surface and helicopter and in the detector. The associated energy loss may lead to a registration of the photon in a lower photon energy window.

- The poor energy resolution of a NaI(Tl)-detector compared to modern solid-state detectors causes the possibility that photons with energies near the energy limits of a photon energy window are registered in the adjacent energy window.

- ^{238}U and ^{232}Th are parent radionuclides of complete decay series emitting photons throughout the complete energy spectrum.

The stripping factors between energy windows are determined in the laboratory with point sources in around 1 m distance to the detector. For the natural radionuclides ^{40}U, ^{238}U and ^{232}Th, these values are adjusted for infinite sources measured with 100 m ground clearance according to Schwarz (1991).

Prior to the exercises in 2020, detector RLL 001 was maintained by the manufacturer replacing two of the four NaI(Tl) crystals. As a change of spectral cross-talk could be expected from this maintenance, the laboratory measurements for the determination of the stripping factors described in PSI-report 18-04 were repeated in September 2020 between ARM20c and ARM20m. Table 4 shows the resulting stripping factors, which are stored in the header of all ERS 2.0 files under identifier ISWS_winname1_winname2 (see section 6).

"'from"'-window	"'to"'-window	Stripping factor
Uranium	Potassium	0.93
Thorium	Potassium	0.48
Cobalt	Potassium	0.07
Thorium	Uranium	0.36
Uranium	Thorium	0.05
Potassium	Caesium	0.45
Uranium	Caesium	3.16
Thorium	Caesium	1.65
Cobalt	Caesium	0.15
Potassium	Cobalt	0.76
Uranium	Cobalt	2.37
Thorium	Cobalt	0.68

Table 4: Stripping factors for relevant energy windows.

1.4 Data presentation

A first brief report (Kurzbericht) of the measurement results of ARM20c is compiled by the measurement team and published immediately after the end of the exercise on the homepage of NEOC. These reports are archived at `https://far.ensi.ch`.

Results of ARM20m and a further data evaluation of both parts of the exercise are published in the form of a PSI-report, within the responsibility of the FAR. These reports are also archived at `https://far.ensi.ch`.

For all measuring areas, a map of the total dose rate (measuring quantity H*(10) extrapolated to 1 m above ground) and the flight lines is presented together with a map of the Man-Made-Gross-Count (MMGC) ratio. A map of the ^{232}Th activity concentration (measuring quantity activity per wet mass) yields quality information as it can be expected that this quantity is constant over time. As an additional quality measure, an appendix with the basic parameters of the data evaluation is added to simplify a re-evaluation of the data in the future. If the MMGC-ratio indicates elevated values, maps of individual radionuclides are added based on the average photon spectrum over the affected area. In the case of large changes of topography in the measured area, a map of the terrestrial dose rate consisting of the total dose rate reduced of the altitude dependent cosmic component is included. In the case of measuring flights with the main purpose of mapping natural radionuclide concentrations, a supplementary map of the ^{40}K activity concentration (measuring quantity activity per wet mass) may also be presented.

Starting with this report, new discrete colour scales defined by the Swiss Expert Group for Aeroradiometrics (FAR) replace the gradient colour scale used in previous reports. The colours, their representation as red, green and blue (RGB) values are listed in Table 5 together with the represented ranges of measured values. The unit of dose rates used in previous reports, [nSv/h], was changed with the new representation to [μSv/h], the unit used to store dose rate values in the ERS 2.0 format (see PSI-report 18-04).

Colour	Red	Green	Blue	Dose rate $[\mu Sv/h]$	MMGC-ratio [ ]	Activity concentration [Bq/kg]	
						^{40}K	^{238}U, ^{232}Th, ^{137}Cs
	153	0	153	>10	>100	>10 000	> 5000
	204	0	102	5 - 10	50 - 100	5000 - 10 000	1000 - 5000
	204	0	0	2 - 5	15 - 50	2000 - 5000	500 - 1000
	255	0	0	0.5 - 2	9 - 15	1500 - 2000	250 - 500
	255	176	51	0.3 - 0.5	8 - 9	1000 - 1500	200 - 250
	255	235	51	0.2 - 0.3	7 - 8	800 - 1000	150 - 200
	230	255	128	0.15 - 0.2	unused	600 - 800	100 - 150
	173	255	153	0.1 - 0.15	unused	400 - 600	75 - 100
	073	255	106	0.08 - 0.1	6 - 7	200 - 400	50 - 75
	102	255	255	0.06 - 0.08	5 - 6	100 - 200	25 - 50
	77	148	255	0.04 - 0.06	unused	50 - 100	12.5 - 25
	51	102	179	< 0.04	< 5	< 50	< 12.5

Table 5: Quantification of the color scale.

2   Results of the exercise ARM20

The flights of the civil part ARM20c of the exercise were performed between June 12th and June 19th, 2020. An intercomparison with ground measurements was performed on Thun military training ground. This area is planned to be used as reference area for testing the performance of the ARM system. Altitude profiles over Lake Thun were used to quantify the influence of cosmic radiation and the helicopter background on the measurement system (see section 1.3.1).

According to the alternating schedule of the annual ARM exercises, the environs of the nuclear power plants Beznau (KKB) and Leibstadt (KKL) and the nuclear facilities of the Paul Scherrer Institute (PSI) and the Zwischenlager Würenlingen AG (Zwilag) were surveyed. Additional measurements were performed between Brugg and Zurich, over the lakeshore of Lake Zurich and over the town of St. Gallen.

The flights of the military part of the exercise ARM20m were performed from November 9th to November 13th. ARM20m contained test measurements over an area near the French border and a large region north of Lake Geneva to improve the aeroradiometric coverage of Switzerland.

Flight velocity of the Super Puma helicopters of the Swiss Air Force was around 30 m/s with a ground clearance of 90 m for all measuring flights. The counting interval of the spectra was one second.

Personnel of the military units Stab BR NAZ and NBC-EOD Centre of Competence performed the measurements supported by experts from ENSI, PSI, ETHZ, ABC Abwehr Einsatzkompanie and NEOC.

Flight parameters of the measuring flights are listed in Table 6 and an overview of the according flight lines is shown in Figure 12.

| Location	Flight number	Measuring time [s]	Length of run [km]	Area [km²]
	ARM20c			
Thun military training ground				
Flight A	Heli 1_20200618 1015	1094	38	5
Flight B	Heli 1_20200618 1130	1126	38	4
Flight C	Heli 1_20200618 1420	1330	46	5
Altitude profiles Lake Thun				
Profile A	Heli 1_20200618 1038	760	24	-
Profile B	Heli 1_20200618 1055	1748	46	-
KKB, KKL, PSI and Zwilag	Heli 1_20200615 0900	14 728	692	154
	Heli 1_20200615 1345			
	Heli 1_20200616 1345			
Brugg - Zürich	Heli 1_20200616 0835	13 929	628	566
	Heli 1_20200616 1430			
	Heli 1_20200616 1445			
Shore of Lake Zurich				
With rain	Heli 1_20200617 0830	7044	319	69
	Heli 1_20200617 0905			
Without rain	Heli 1_20200619 0834	4140	185	42
St. Gallen	Heli 1_20200617 1430	2734	130	31
	ARM20m			
Mont Pelé	Heli 1_20201111 1025	1169	54	11
North Lake Geneva	Heli 1_20201109 1015	53 049	2575	708
	Heli 1_20201109 1400			
	Heli 1_20201111 1350			
	Heli 1_20201112 0915			
	Heli 1_20201112 1330			
	Heli 1_20201112 1545			
	Heli 1_20201113 0930			
	Heli 1_20201113 1345			

Table 6: Flight data of ARM20.
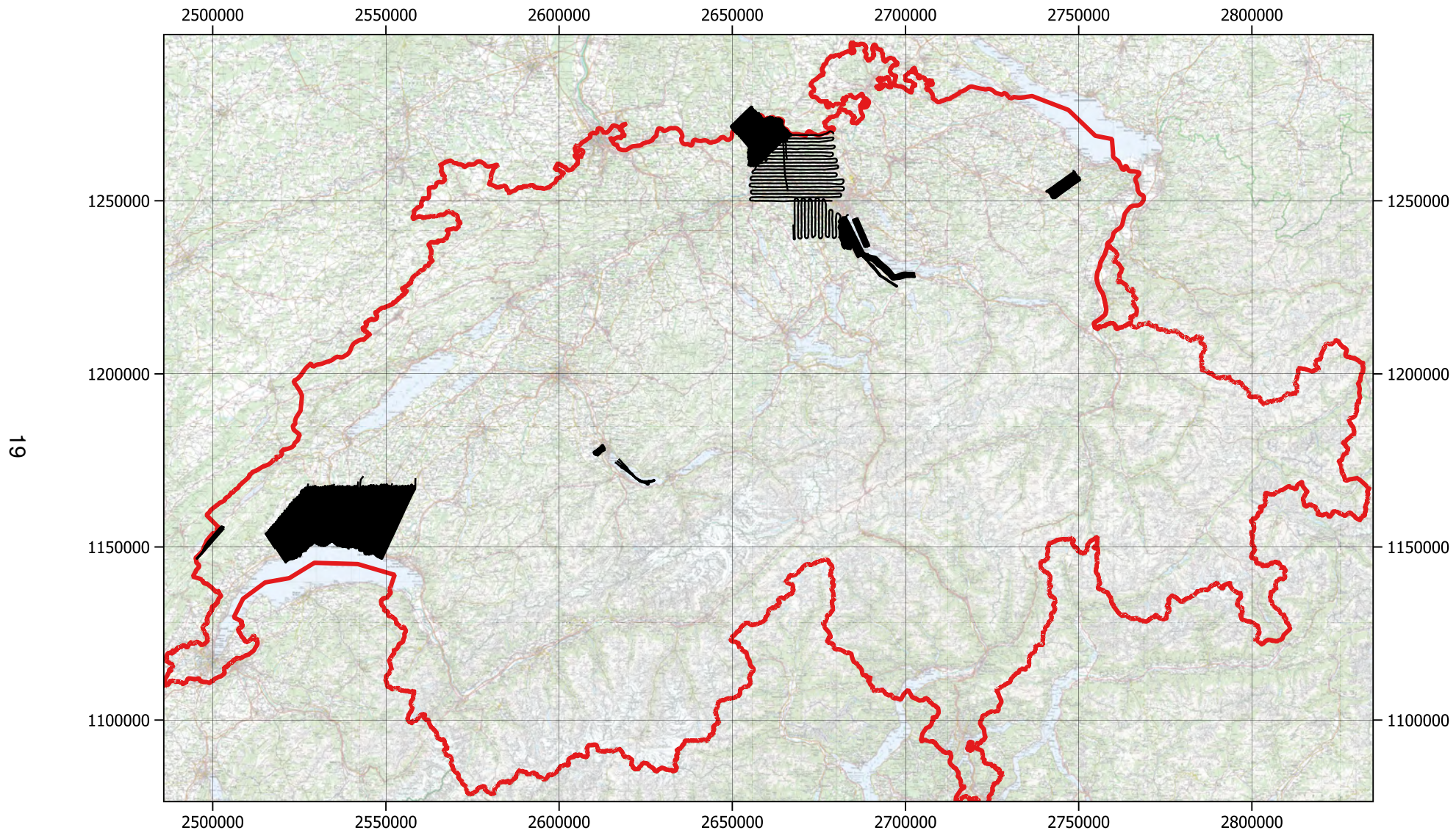
Figure 12: Overview of the measurement areas of ARM20. PK200©2020 swisstopo (JD100042).

2.1 ARM20c

2.1.1 Thun military training ground

The measurements at Thun military training ground were aimed at several targets:

- Intercomparison of in-situ measurements

- Comparison of aeroradiometric measurements with ground measurements

- Source search with manned and unmanned aerial vehicles and ground vehicles

Figure 13 shows the source locations and the points of in-situ ground measurements at Thun military training ground. The location, radionuclide and strength of the radioactive sources (Table 7) were selected to have negligible influence on the measurements in the area where in-situ measurements were performed. All teams performed measurements at point no. 7, where the dose rate was additionally monitored during the complete exercise with the Swiss reference instrument for ambient dose equivalent rate operated by the calibration laboratory for radiation protection instruments of PSI.
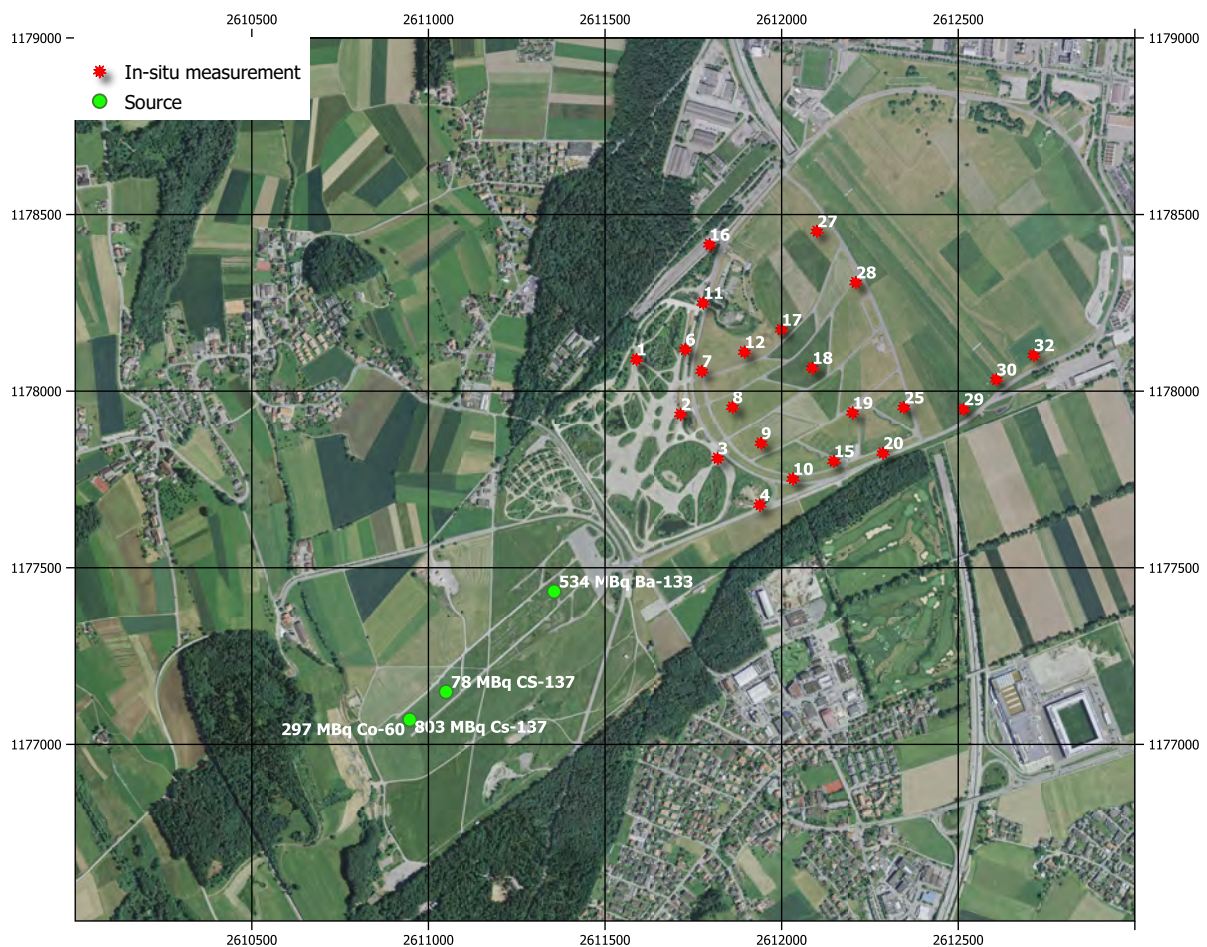

Figure 13: Overview of the measurement areas at Thun military training ground. Swissimage©2020 swisstopo (JD100042).

Radionuclide	Activity [MBq]	E-coordinate [m]	N-coordinate [m]
^{137}Cs	803	2610947	1177070
^{133}Ba	534	2611356	1177433
^{60}Co	297	2610947	1177070
^{137}Cs	78	2611050	1177149

Table 7: Location of the radionuclide sources placed in the exercise area.

Five gammaspectrometric in-situ-teams of the Federal Office for Public Health (FOPH), the Institute de Radiophysique (IRA), NBC-EOD, the emergency response teams of Spiez Laboratory and the Paul Scherrer Institute (PSI) participated in the exercise. Figure 14 shows some of the teams in the field. Figure 15 shows the measured raw values of the reference instrument (high pressure ionisation chamber) calculated using the manufacturer calibration.

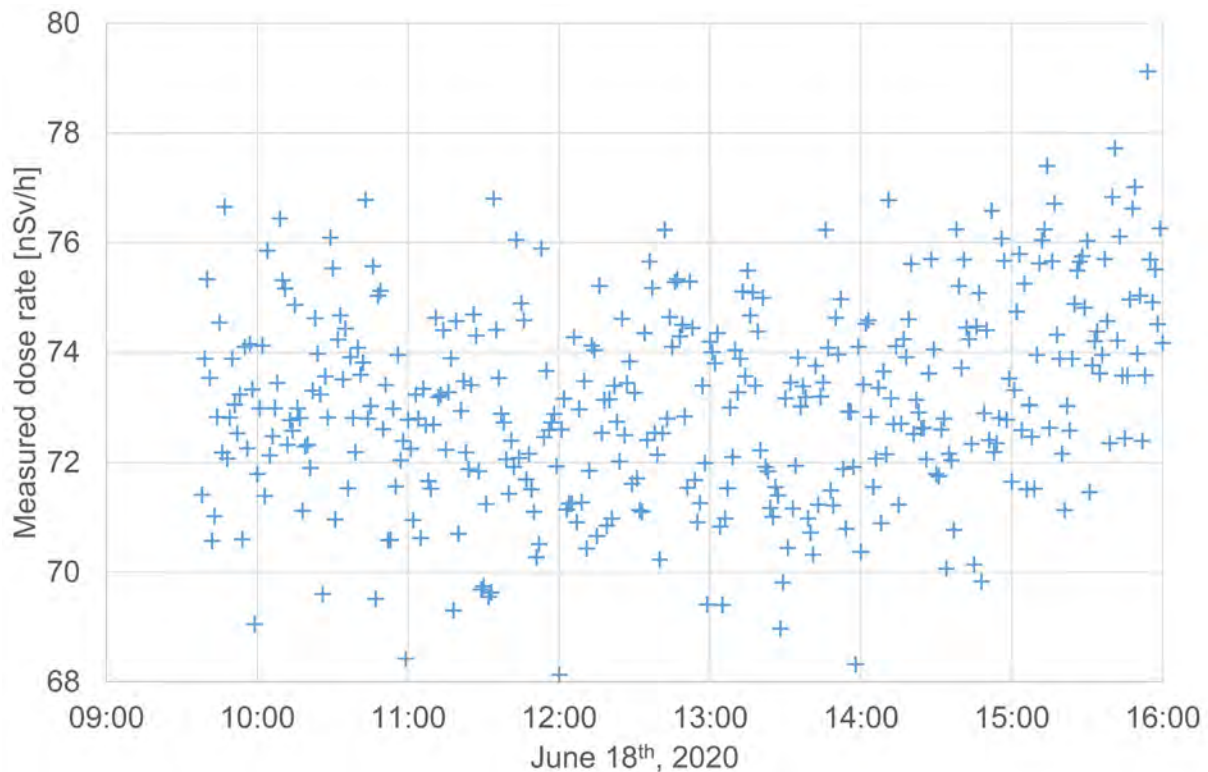Figure 14: In-situ teams at Thun military training ground.

Figure 15: Measured dose rates during the intercomparison at the reference point.

The measured values of the dose rate at the reference point show fluctuations due to counting statistics. No significant trend of the dose rate readings can be identified during the exercise. A slight increase of the dose rate at the end of the exercise may be caused by beginning rain with wet deposition of radon progeny on the ground. The raw dose rate values measured at point no. 7 were averaged over the whole exercise. The calibration factor, intrinsic background and response of the reference instrument for charged and neutral particles, which were determined with extensive measurements at the Physikalisch-Technische Bundesanstalt (PTB) in Braunschweig, Germany, were applied to this average value, yielding the reference ambient dose equivalent rate of 78.5 ± 2.4 nSv/h at reference point no. 7. Figure 16 shows the dose rates determined with direct doseratemeter measurements and the dose rates calculated from the activity concentrations measured with in-situ gamma spectrometry reported without associated uncertainty. All directly measured dose rates agree well within the measurement uncertainties specified by the participants with extension factor k=2. Table 8 summarises dose rates measured directly with a doseratemeter and derived from the in-situ measurements together with activity concentrations determined with in-situ gamma spectrometry by each team at the reference point. The variation of activity concentrations is larger than observed for the dose rate measurements, both between teams and radionuclides of the natural radioactive decay series.
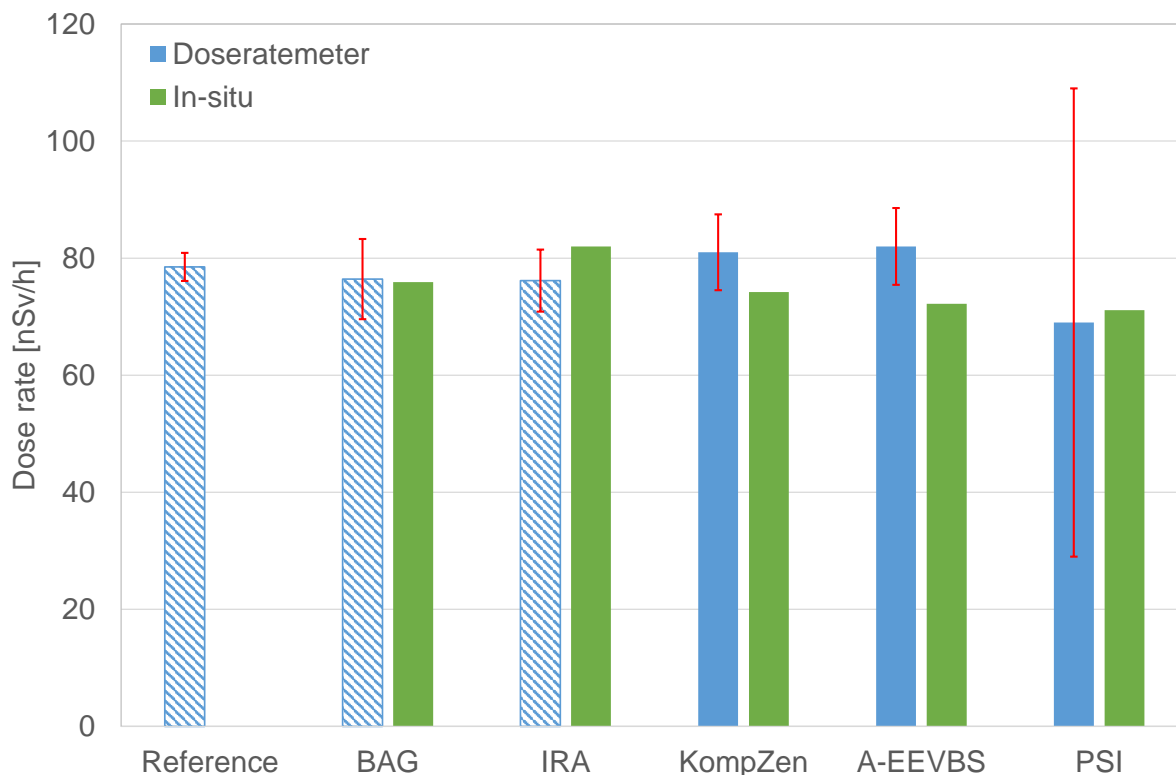
Figure 16: Comparison of dose rates at the reference point. Blue hatched: High pressure ionisation chamber, Blue solid: Szintillation detector.

Participant Parameter	FOPH		IRA		NBC-EOD		Spiez Laboratory		PSI	
Dose rate measured [nSv/h]	76	± 7	76	± 7	81	± 7	82	± 7	69	± 40
Dose rate in-situ [nSv/h]	76		82		74		72		71	
Nuclide	Activity concentration [Bq/kg]									
^{40}K	197	± 21	217	± 16	217	± 46	226	± 48	159	± 13
^{137}Cs	2.2	± 0.4	2.8	± 0.6	2.5	± 1.7	2.6	± 1.0	2.0	± 0.2
^{212}Pb	17	± 2	19	± 2	16	± 4	20	± 4	14	± 12
^{212}Bi	23	± 5	25	± 8	13	± 7	-		18	± 16
^{228}Ac	15	± 2	17	± 1	18	± 3	20	± 3	13	± 6
^{208}Tl	17	± 2	22	± 2	15	± 3	18	± 3	15	± 9
^{226}Ra	7	± 3	26	± 21	-		-		44	± 6
^{214}Pb	15	± 2	14	± 2	14	± 3	15	± 3	12	± 5
^{214}Bi	15	± 2	17	± 2	15	± 3	17	± 3	11	± 11

Table 8: Results of the ground measurements at the reference point no. 7. ^{208}Tl activity concentration divided by branching ratio for better comparison.

Measurements of all teams at the different measuring points are used for a comparison with airborne measurements. The dose rate was determined with doseratemeters and the activity concentrations with in-situ gammaspectrometry. At point 7, the reference dose rate and the average of activity concentrations measured by all teams was used.

These values were compared to the results of three aeroradiometric flights. The data points of the flight lines were selected according to their distance to the points of the in-situ measurements. While up to a maximum distance of 200 m to the next in-situ coordinate very similar averages are obtained from the aeroradiometric data, a maximum distance of 50 m to the next in-situ point was used in the further evaluations. The total dose rate obtained with the ground measurements could not be used for a comparison to the aeroradiometric data as a different contribution of cosmic radiation is added to the dose rate generated by radionuclides in the ground. Thus, the cosmic dose rate of 46 nSv/h used for the ground measurements was subtracted from the total dose rate of 77 nSv/h to determine the terrestrial dose rate of 31 nSv/h. This value can be compared directly with the terrestrial dose rate determined with the spectrum dose index (SDI) method (ERS identifier DHRS_GND). Table 10 shows the average values over the selected points for the three flights. The average over the three flights was used to calculate the ratio between airborne and ground measurements. The original calibration of activity concentrations for the Swiss aeroradiometric system was performed using mainly laboratory measurements. Thus, the determined activity concentrations were based on dried soil, characterised with the AD identifier in ERS formats. Starting with this report, activity concentrations are specified for soil in natural condition (ERS identifier AW) to render direct compatibility to in-situ measurements. As an additional advantage, dose rate conversion factors defined by the Federal Commission on Radiation Protection (KSR, 2010) can be used directly without assumptions on the water content of the soil for calculating the dose response of the different radionuclides. The activity concentrations based on the wet weight can be expected to be around 20% lower than the activity concentrations based on dry weight previously reported.

Point	Team	Dose rate [nSv/h]	Activity concentration [Bq/kg]			
			^{40}K	^{137}Cs	^{238}U	^{232}Th
1	FOPH	68 ± 5	102 ± 12	0.8 ± 0.3	13 ± 2	10 ± 2
2	FOPH	70 ± 6	110 ± 12	0.5 ± 0.2	14 ± 2	12 ± 2
3	FOPH	67 ± 5	87 ± 10	-	13 ± 2	10 ± 2
4	FOPH	73 ± 9	181 ± 20	1.7 ± 0.4	17 ± 2	18 ± 3
6	IRA	71 ± 5	121 ± 13	0.7 ± 0.7	15 ± 2	11 ± 3
7	Average	79 ± 2	203 ± 29	2.4 ± 0.8	15 ± 3	18 ± 5
8	IRA	80 ± 6	211 ± 21	5.5 ± 1.3	17 ± 3	17 ± 3
9	IRA	84 ± 6	250 ± 24	6.5 ± 1.4	19 ± 3	24 ± 5
10	IRA	85 ± 6	251 ± 23	7.3 ± 1.4	18 ± 3	22 ± 3
11	PSI	65 ± 38	117 ± 96	-	11 ± 5	9 ± 6
12	PSI	80 ± 47	118 ± 97	-	10 ± 5	9 ± 7
15	IRA	85 ± 6	224 ± 23	6.8 ± 1.6	23 ± 4	20 ± 5
16	PSI	55 ± 32	80 ± 66	-	16 ± 12	8 ± 6
17	Spiez Lab.	80 ± 6	280 ± 61	2.9 ± 1.2	17 ± 3	24 ± 4
18	Spiez Lab.	80 ± 6	188 ± 41	7.5 ± 2.0	15 ± 3	16 ± 3
19	Spiez Lab.	86 ± 7	201 ± 44	4.7 ± 1.5	15 ± 3	21 ± 4
20	Spiez Lab.	83 ± 7	251 ± 53	6.2 ± 1.6	20 ± 3	24 ± 4
25	Spiez Lab.	71 ± 6	210 ± 45	2.8 ± 0.9	21 ± 3	19 ± 4
27	NBC-EOD	78 ± 6	175 ± 39	6.6 ± 1.8	18 ± 3	16 ± 3
28	NBC-EOD	75 ± 6	173 ± 39	3.8 ± 1.3	14 ± 3	15 ± 5
29	NBC-EOD	88 ± 7	262 ± 57	6.5 ± 1.9	20 ± 4	23 ± 5
30	NBC-EOD	82 ± 7	247 ± 54	4.7 ± 1.5	18 ± 3	21 ± 6
32	NBC-EOD	83 ± 7	264 ± 56	7.1 ± 1.8	29 ± 4	21 ± 6
Aver.	All teams	77 ± 8	187 ± 63	4.5 ± 2.4	17 ± 4	17 ± 6

Table 9: Results of the ground measurements.

Several radionuclide sources were placed in the exercise area to train the search for radioactive sources. A ^{137}Cs- and a ^{60}Co-source located at the same coordinate (Table 7) were used to adjust the calibration factor for point source activity (ERS identifier AP). For this calibration, the measured point with the smallest distance to the sources was selected for all three flights. The minimum distance to the source is an important parameter for the determination of the source activity due to the inverse-square law between detector signal and distance between source and detector. The measured point source activities of all three flights were averaged and compared to the certified activities of the sources and the ratio between certified and measured activity calculated (Table 10). With the ratios of aeroradiometric measurements to in-situ results or certified activities, adjustments to the respective calibration factors were calculated and used for all further evaluations of this exercise. The according evaluation parameters are stored as header of the generated files in ERS 2.0 format (section 6).

The RLL systems are operated during flight using proprietary software of the manufacturer (Mirion). The results of the Mirion on-line evaluation software are listed in Table 11. The

terrestrial dose rate (DHSR_GND) determined with the Mirion software agrees well with the ground measurements. The deviation of the activity concentrations of the natural radionuclides (ERS-Identifier AW) determined with the Mirion system to the in-situ measurements was already observed comparing the Mirion software to the previous evaluation software MGS32 (see PSI report No. 20-01). The ^{137}Cs activity concentration determined with the Mirion system over the in-situ area was zero for all points.

The Mirion-software includes nuclide identification algorithms. Figure 17 shows screenshots of the nuclide identification tab of two alarm windows near the three detected and identified sources. The configuration of flight C (MMGC-alarm plus identification) was able to identify all source nuclides (^{137}Cs, ^{60}Co and [133]Ba), but did not provide values of estimated source activity for [133]Ba. The source activities determined during the flights with the Mirion-software are listed in Table 11, fitting closer to the certified source activities compared to the evaluation using the newly developed software AGS_CH with unadjusted calibration factors. The detection limits of the RLL system for point sources are given by the manufacturer of the RLL system to be 770 MBq for [133]Ba, 330 MBq for ^{137}Cs and 340 MBq for ^{60}Co, based on a ground clearance of 100 m and an averaging interval of five seconds. The nuclide identification algorithms included in the Mirion-software exceed the nuclide identification capabilities of the energy window method by far and thus improve considerably the assistance to the operators.

| ERS 2.0 Identifier	Flight A	Flight B	Flight C	Average	Ground	$\frac{Ground}{Airborne}$
DHSR_GND [nSv/h]	40	41	39	40	31	78 %
AW_K-40 [Bq/kg]	247	240	246	244	187	77 %
AW_U-238 [Bq/kg]	13	14	11	12	17	136 %
AW_Th-232 [Bq/kg]	21	21	20	21	17	82 %
AW_Cs-137 [Bq/kg]	8	11	8	9	5	51 %
AP_Cs-137 [MBq]	2217	2628	2378	2409	803	33 %
AP_Co-60 [MBq]	486	541	519	515	297	58 %

Table 10: Comparison of ground and airborne measurements evaluated with the AGS_CH software.

ERS 2.0 Identifier	Flight A	Flight B	Flight C	Average	Ground	$\frac{Ground}{Airborne}$
DHSR_GND [nSv/h]	32	33	31	32	31	96 %
AW_K-40 [Bq/kg]	136	129	132	132	187	142 %
AW_U-238 [Bq/kg]	13	15	12	13	17	127 %
AW_Th-232 [Bq/kg]	15	15	14	15	17	116 %
AP_Cs-137 [MBq]	1064	818	960	947	803	85 %
AP_Co-60 [MBq]	259	171	227	219	297	74 %

Table 11: Comparison of ground and airborne measurements evaluated with the Mirion Software.
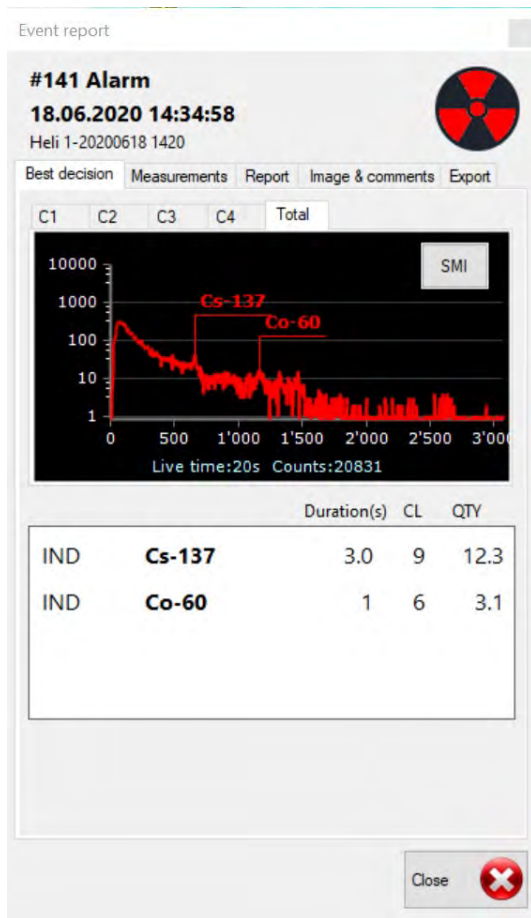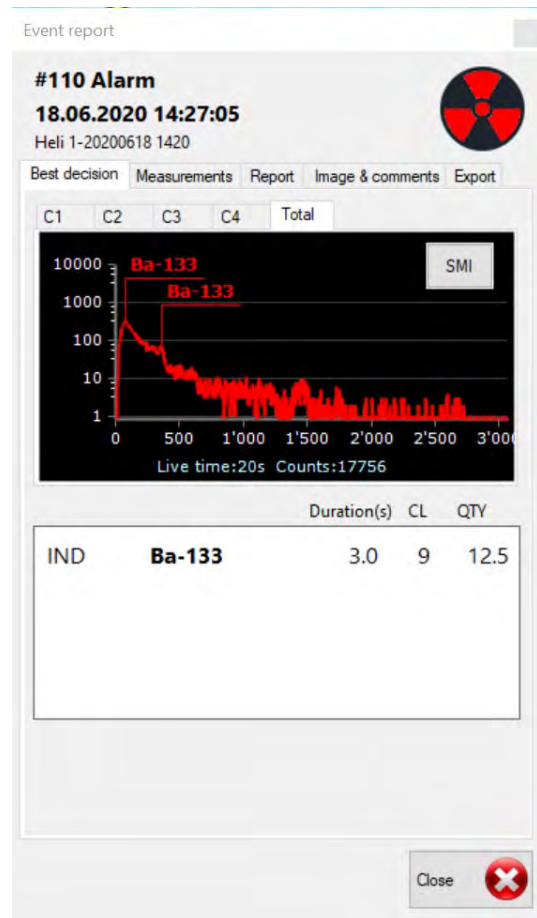
Figure 17: Screenshot of the nuclide identification tab of two alarm windows. a) Near [137]Cs- and ^{60}Co-source; b) Near [133]Ba-source.

The maps of the natural radionuclides (Figures 18 to 20) show a homogeneous distribution over the measuring area with a region of slightly lower readings extended north-south in the centre of the measuring area. This pattern is repeated in the dose rate map (Figure 21) with the exception of a dose rate increase over the strong [137]Cs- and ^{60}Co-sources placed in the exercise area. The location of the two strong sources can be seen more clearly in the map of the Man-Made-Gross-Count-ratio (MMGC-ratio) (Figure 22). The activity of the ^{137}Cs-source located at coordinates (2611050, 1177149) is well below the detection limit of the measuring system and is not indicated as expected. The photon emissions of the radionuclide [133]Ba are below the lower energy limit of the evaluation procedures of 400 keV. Thus, the location of the [133]Ba-source with an activity of 0.5 GBq is not visible in the MMGC-ratio map (Figure 22).
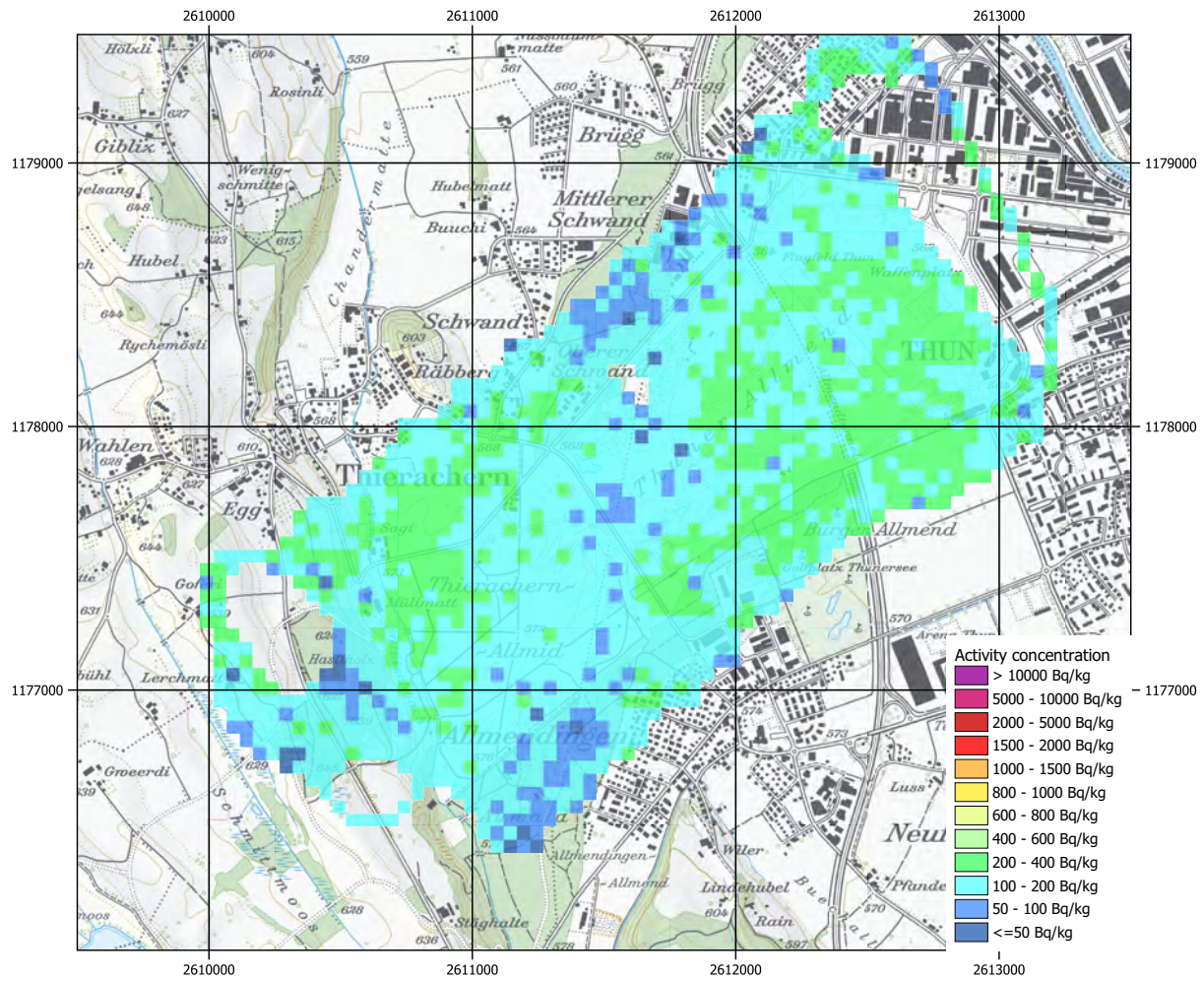
Figure 18: ^{40}K activity concentration measured over Thun military training ground. PK25©2020 swisstopo (JD100042).
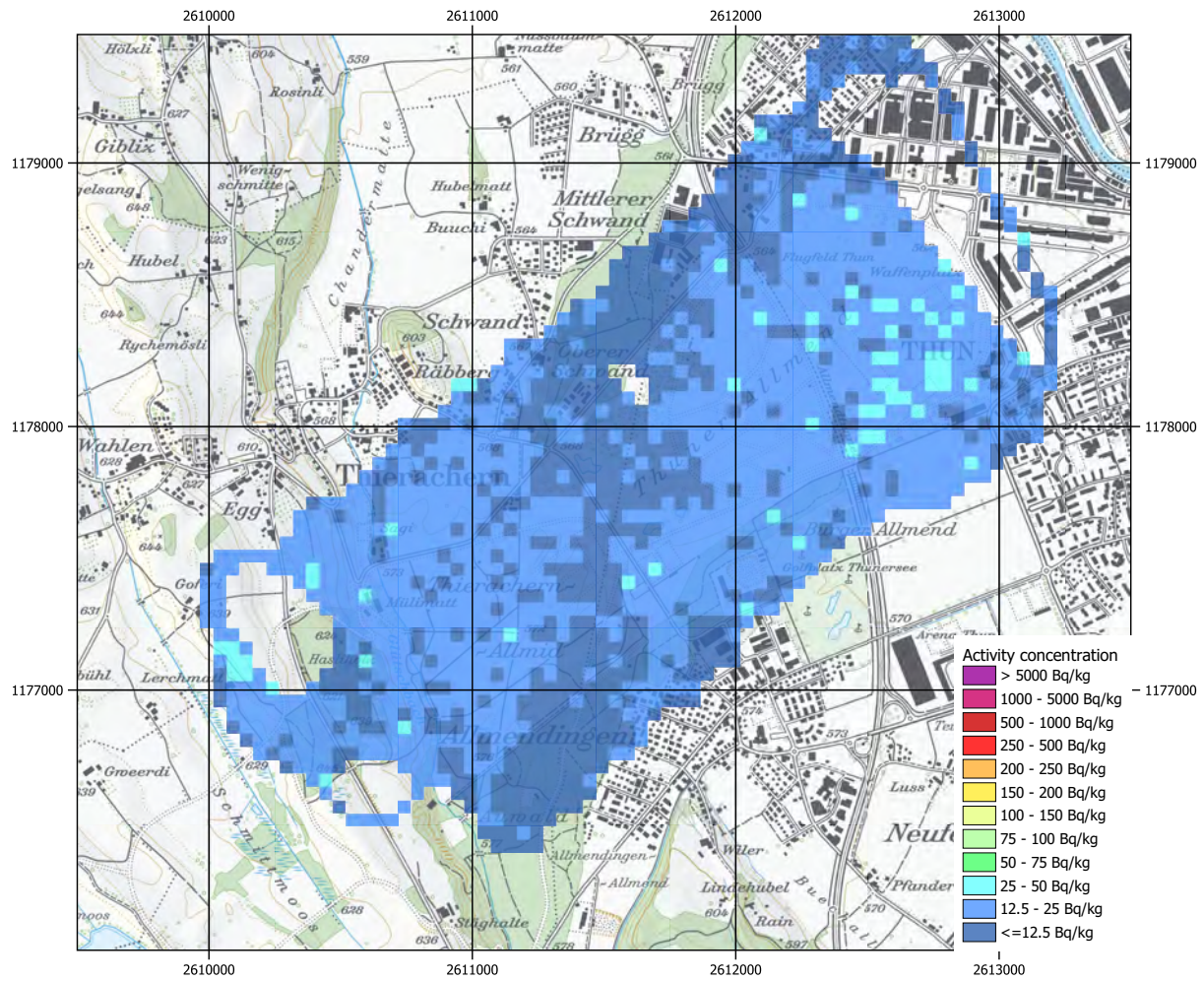
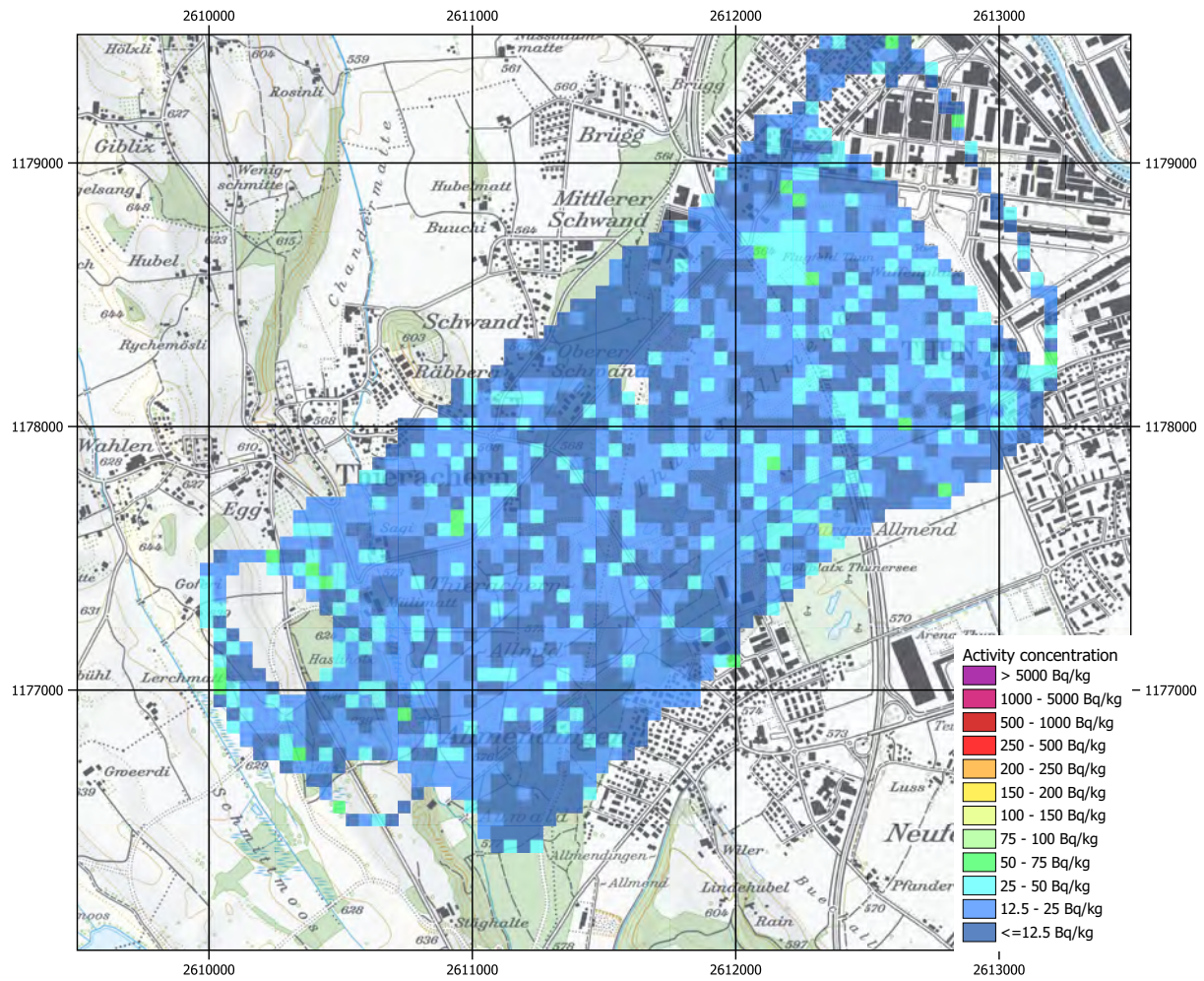Figure 19: ^{232}Th activity concentration measured over Thun military training ground. PK25©2020 swisstopo (JD100042).

Figure 20: ^{238}U activity concentration measured over Thun military training ground. PK25©2020 swisstopo (JD100042).
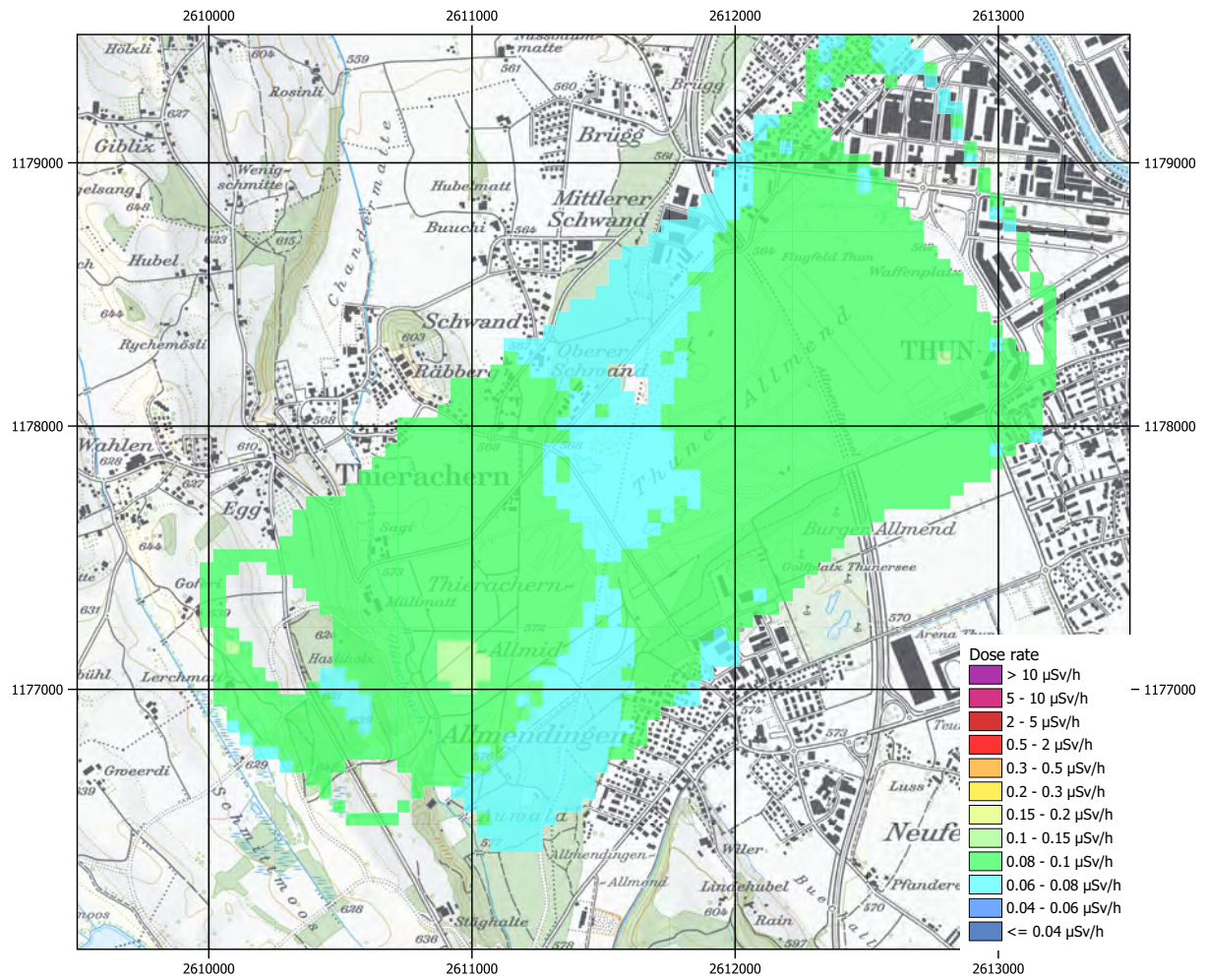
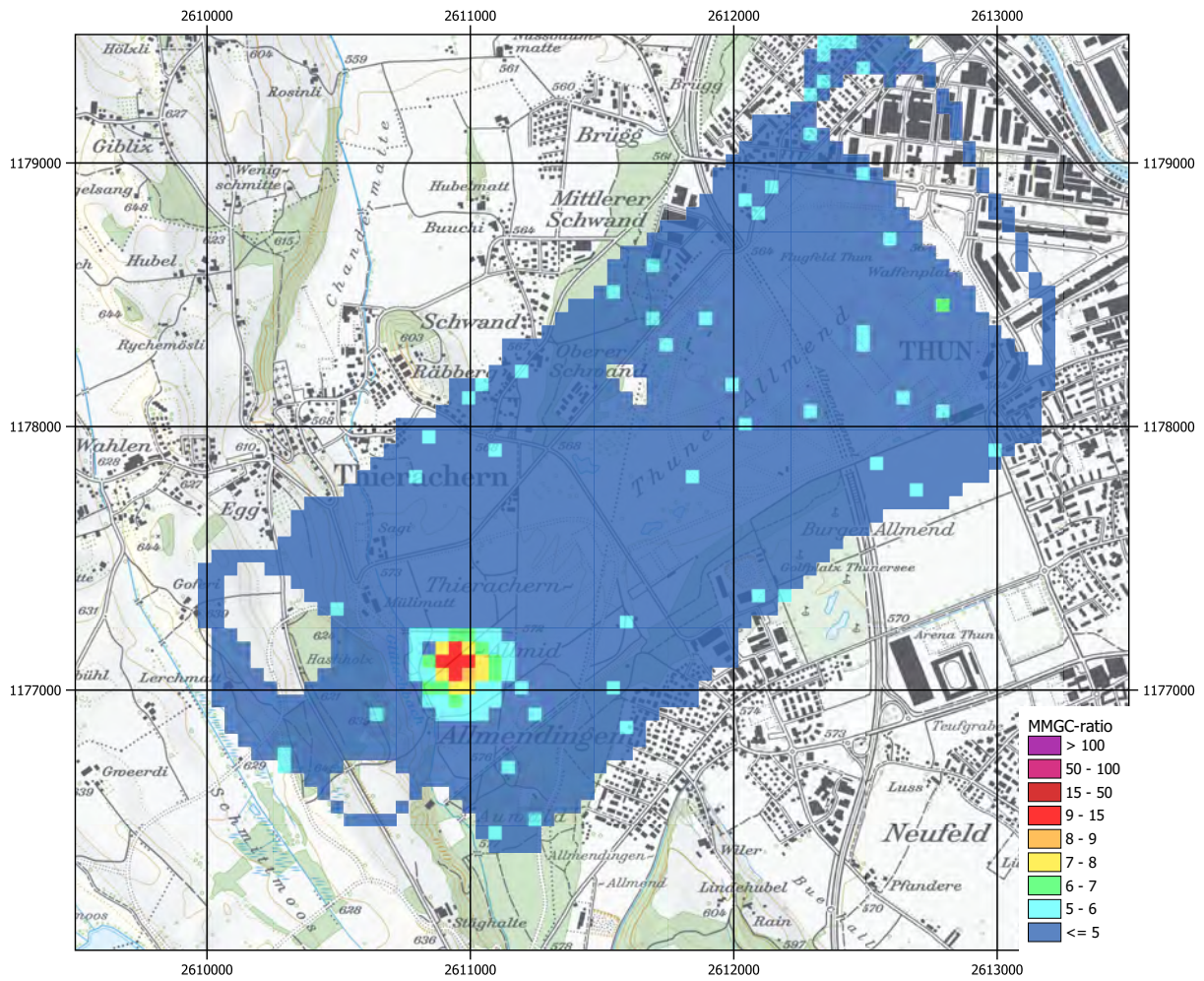Figure 21: Dose rate measured over Thun military training ground. PK25©2020 swisstopo (JD100042).

Figure 22: Man-Made-Gross-Count-ratio (MMGC-ratio) measured over Thun military training ground. PK25©2020 swisstopo (JD100042).

The sources were also searched with a drone equipped with the modular "Drones G" measuring system manufactured by Nuviatech Instuments (Figure 23). The Nuvia measurement system was operated by a team of Spiez Laboratory, whereas the drone was rented and operated by the Swissdrones company. Figure 24 shows the drone together with the Superpuma helicopter carrying the RLL system. Two search fligths were performed carrying alternatively a module with a 3 inch x 3 inch or a 2 inch x 2 inch NaI(Tl) detector. Ground clearance of the drone flights was 25 m, intended to close the gap between airborne gammaspectrometry and ground measurements. Global positioning system (GPS) coordinates were combined with radiological data like photon spectra and dose rate provided by the proprietary software of the NUVIA system. The application of the Nuvia Drones G system in combination with a Swissdrones drone was at the time of the exercise still under evaluation by Spiez Laboratory, so some teething troubles could be expected. During the first flight, the high resolution camera of the drone intended to monitor the flight path was misaligned. The dose rate measured with the 2 inch x 2 inch NaI detector during the second flight yielded negative values or values at least an order of magnitude lower than could be realistically expected.

The dose rate map measured with the drone and 3 x 3 inch NaI detector during the first flight (Figure 25) shows clearly the position of the strong ^{137}Cs- and ^{60}Co-sources. The starting point for the first drone flight was located accidentally near the position of the ^{133}Ba-source, also visible in the dose rate map in the upper right coordinate square of the map. The weak ^{137}Cs-source could not be identified from the dose rate map, giving an indication of the detection limit of the measuring system. However, the weak ^{137}Cs-source could be determined with an evaluation using the waterfall diagram and the graphical representation of the counts in nuclide-specific energy windows. The storage of spectra of the Nuvia system was corrupted during the first flight, inhibiting evaluation of additional parameters like the MMGC-ratio. In a second flight with the 2 inch x 2 inch NaI detector, the area around the ^{133}Ba-source was inspected. The location of ^{133}Ba source could be identified with an analysis of the spacial distribution of evaluated dose rates, albeit with much too low dose rate values. The camera mounted on the drone captured high resolution images during the flight. These images were assembled by the team of Spiez Laboratory to a single aerial view in GeoTIFF format during post-processing. Figure 26 shows the flightlines of drone flight two and the composite aerial view from the drone camera pictures around the location of the ^{133}Ba source. The source itself is too small to be detected in the aerial view.
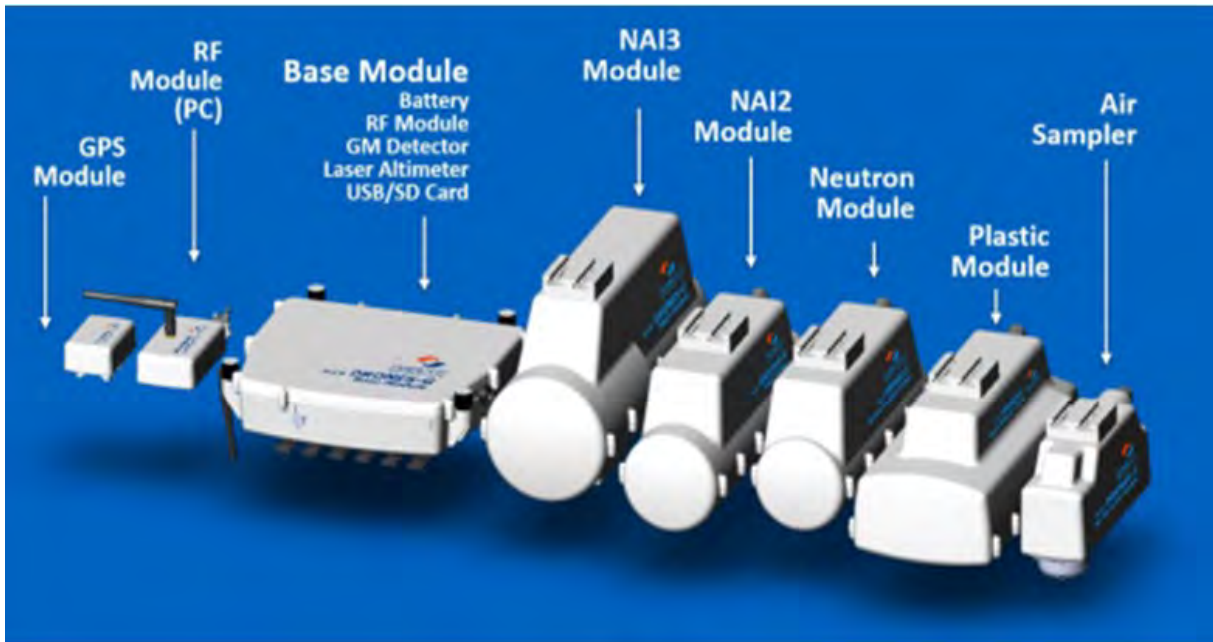
Figure 23: Picture of the Drones G modular measuring system.
©Nuviatech Instruments 2021.

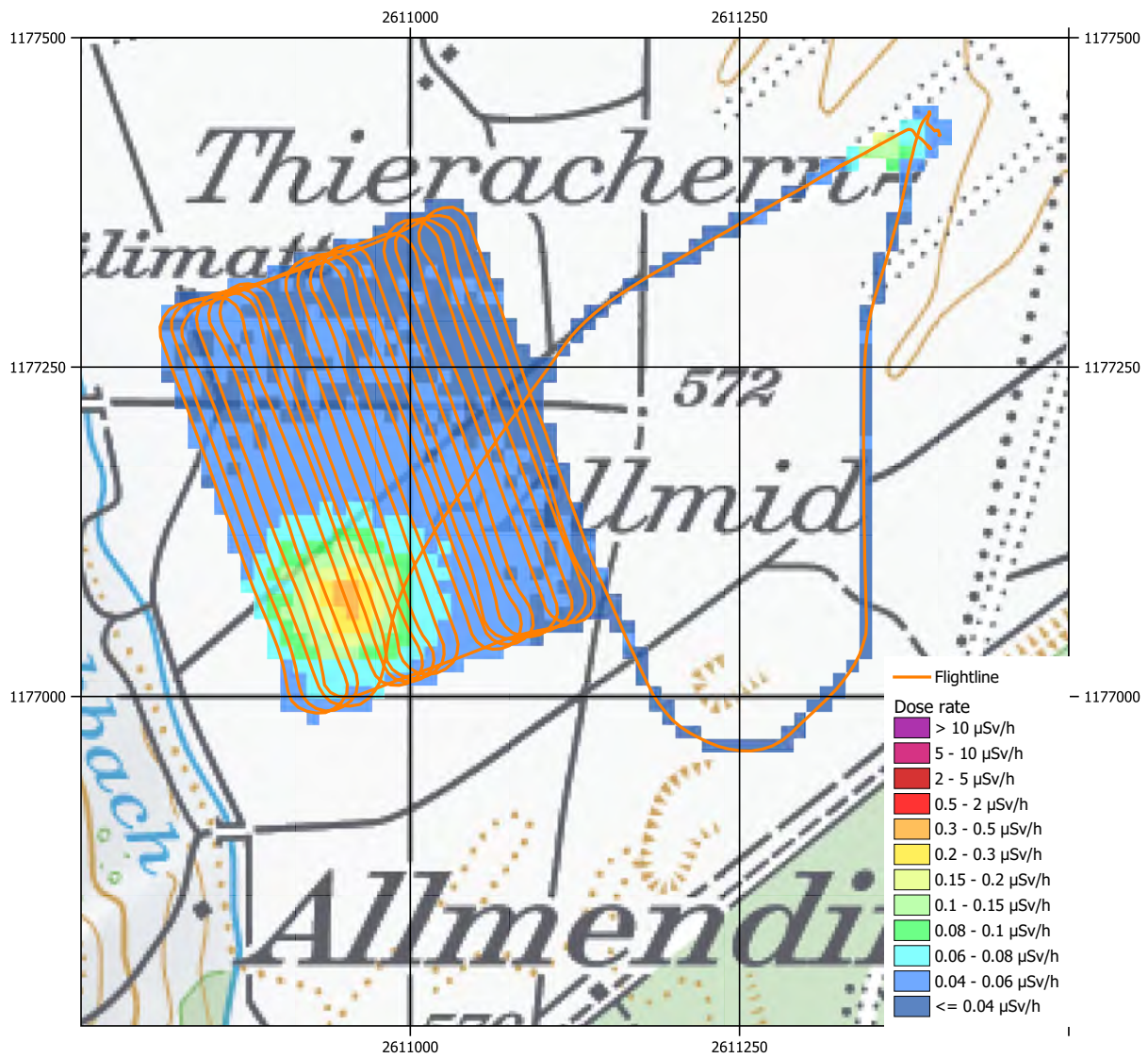Figure 24: Superpuma and drone at Thun military training ground.

Figure 25: Dose rate at Thun military training ground measured with a drone.
PK25©2020 swisstopo (JD100042).

Figure 26: Flight line and aerial view of the area around the [133]Ba source.
PK25©2020 swisstopo (JD100042).

An armoured car (Boden-Radiometrie, BoRa) is equipped with an identical measuring system as is used in the helicopter. The detectors are located in a fiberglass reinforced box mounted on the roof of the car (Figure 27). The car-borne measurement was performed by staff of the NBC-EOD. The software used for data acquisition and evaluation of the car-borne measurements is identical to the software used in the helicopter. The dose rate map measured with car-borne radiometry (Figure 28) clearly indicates the position of the strong ^{137}Cs- and ^{60}Co-sources and shows elevated values at the position of the ^{133}Ba-source. The map of the Man-made gross-count (MMGC) ratio (Figure 29) confirms the localisation of the strong ^{137}Cs- and ^{60}Co-sources, but does not improve localisation of the weak ^{137}Cs-source and the ^{133}Ba-source. Fortunately, the Mirion on-line data processing software used for the car-borne system includes the SIA nuclide identification algorithm also used in the helicopter. Alarm events were generated automatically for all four sources placed in the exercise area, giving location and nuclide identification.

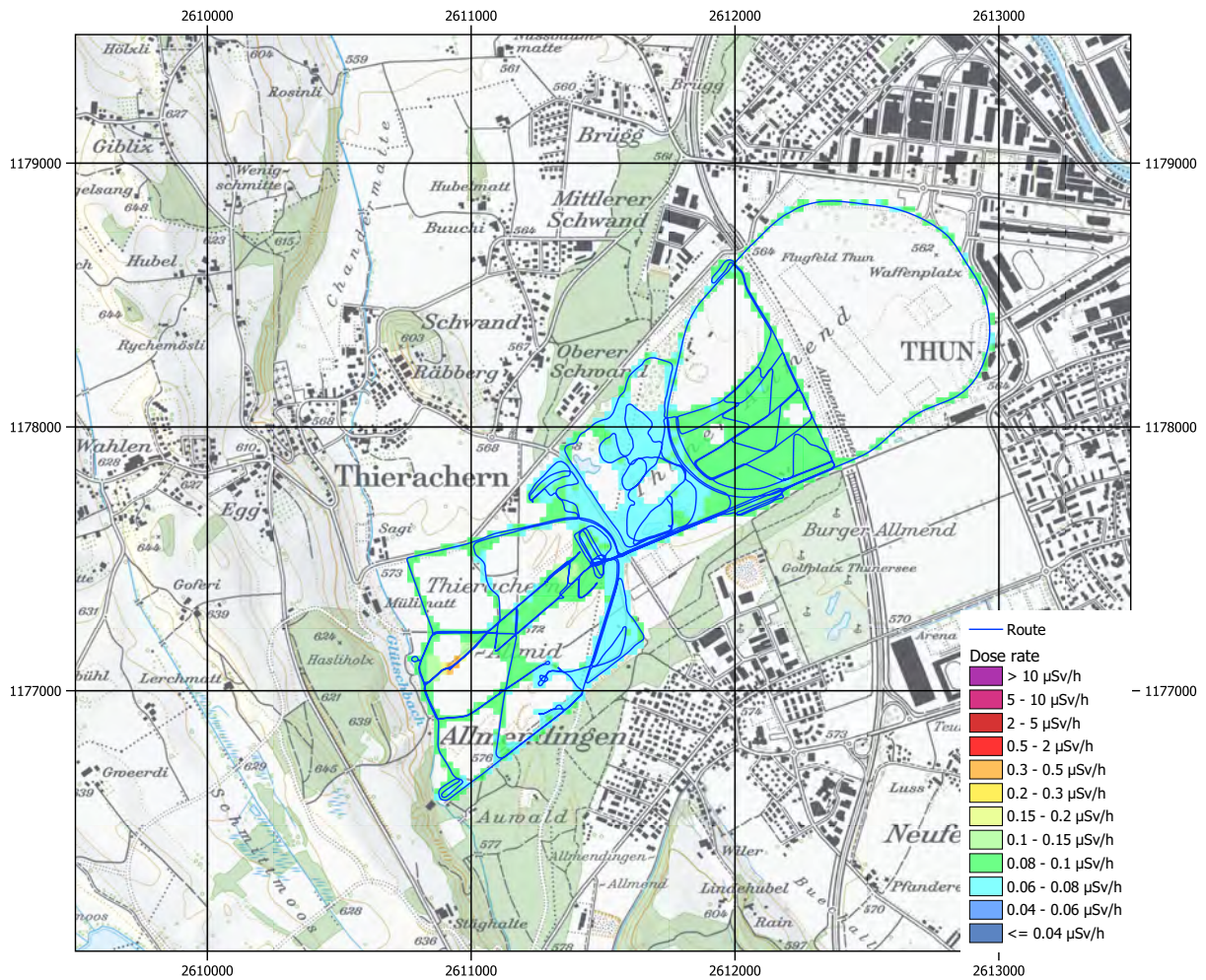Figure 27: Vehicle for ground measurements at Thun military training ground.

Figure 28: Dose rate at Thun military training ground measured with car-borne radiometry. PK25©2020 swisstopo (JD100042).
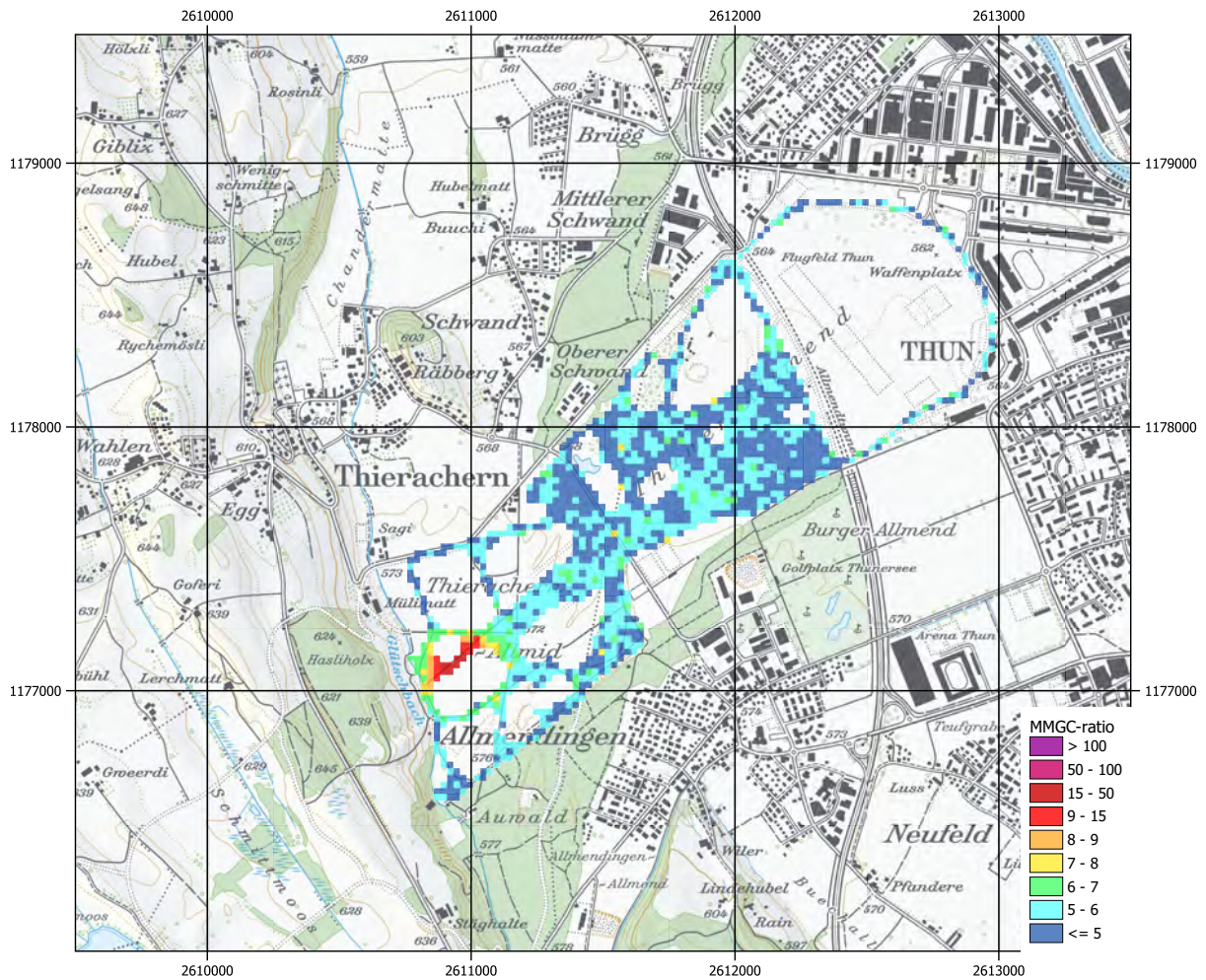
Figure 29: Man-made gross-count (MMGC) ratio at Thun military training ground measured with car-borne radiometry. PK25©2020 swisstopo (JD100042).

2.1.2 Altitude profiles Lake Thun

Figure 30 shows the flight lines of both altitude profiles over Lake Thun. The flight altitudes were flown as steps for Profile A whereas Profile B used a continuous ascent and descent (Figure 31). The evaluation of the altitude profiles together with previous altitude profiles over extended bodies of water is described in section 1.3.1.
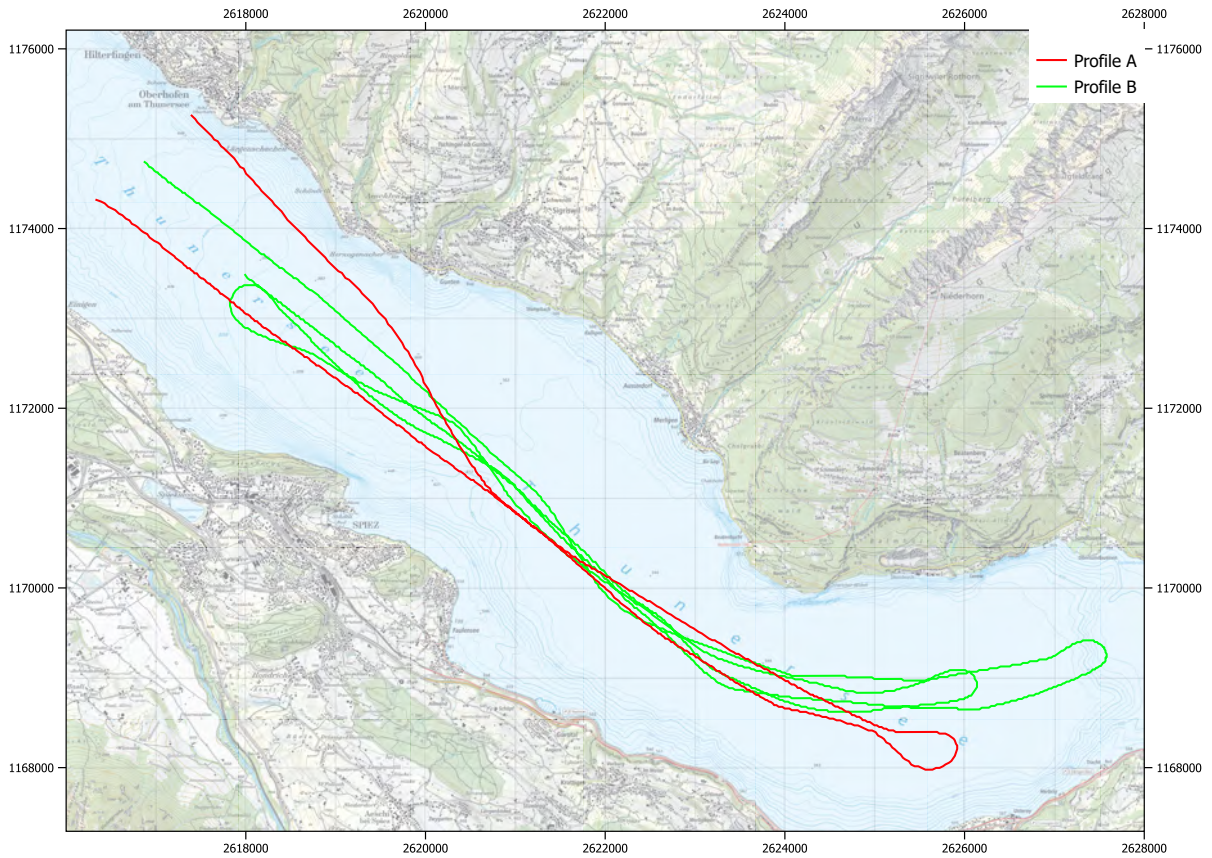
Figure 30: Flight lines of the altitude profiles over Lake Thun.
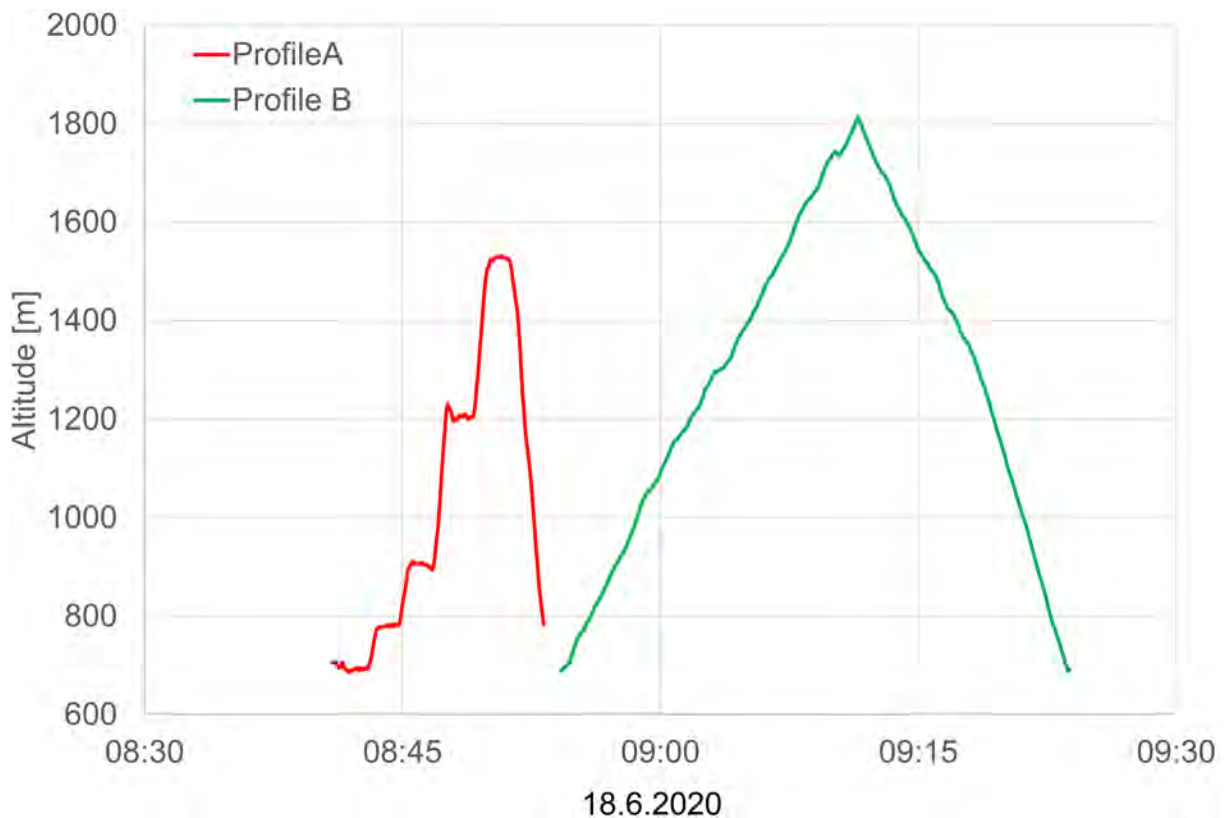Red: Profile A; Green: Profile B. PK25©2020 swisstopo (JD100042).

Figure 31: Altitude versus time of the altitude profiles.

40

2.1.3 Recurrent measurement area KKB, KKL, PSI and Zwilag

According to a biannual sequence of routine measurements, the environs of the nuclear power plants Beznau (KKB) and Leibstadt (KKL), and the nuclear facilities Paul Scherrer Institute and intermediate storage facility Zwilag were inspected in 2020. Following a request of German authorities, the measuring area was extended beyond the Rhine river into German territory.

The dose rate map (Figure 32) shows elevated values over the premises of KKL which are caused by high energy photon radiation of the activation product ^{16}N, a typical result for operating boiling water reactors. The man-made gross-count (MMGC) ratio, an indicator for the presence of man-made radionuclides, displays no significantly elevated readings (Figure 33). The activity concentration of the natural radionuclide ^{232}Th (Figure 34) shows slightly elevated values over the Rotbergegg due to an increased natural Thorium content already observed in the past. As the evaluation of photon energy windows is generally impaired by the presence of ^{16}N high energy photons, no activity concentrations of natural radionuclides are calculated over KKL premises. Otherwise, the variation of ^{232}Th is governed by the attenuation of terrestrial photons by water and the normal variation of the thorium content in soil and rock.
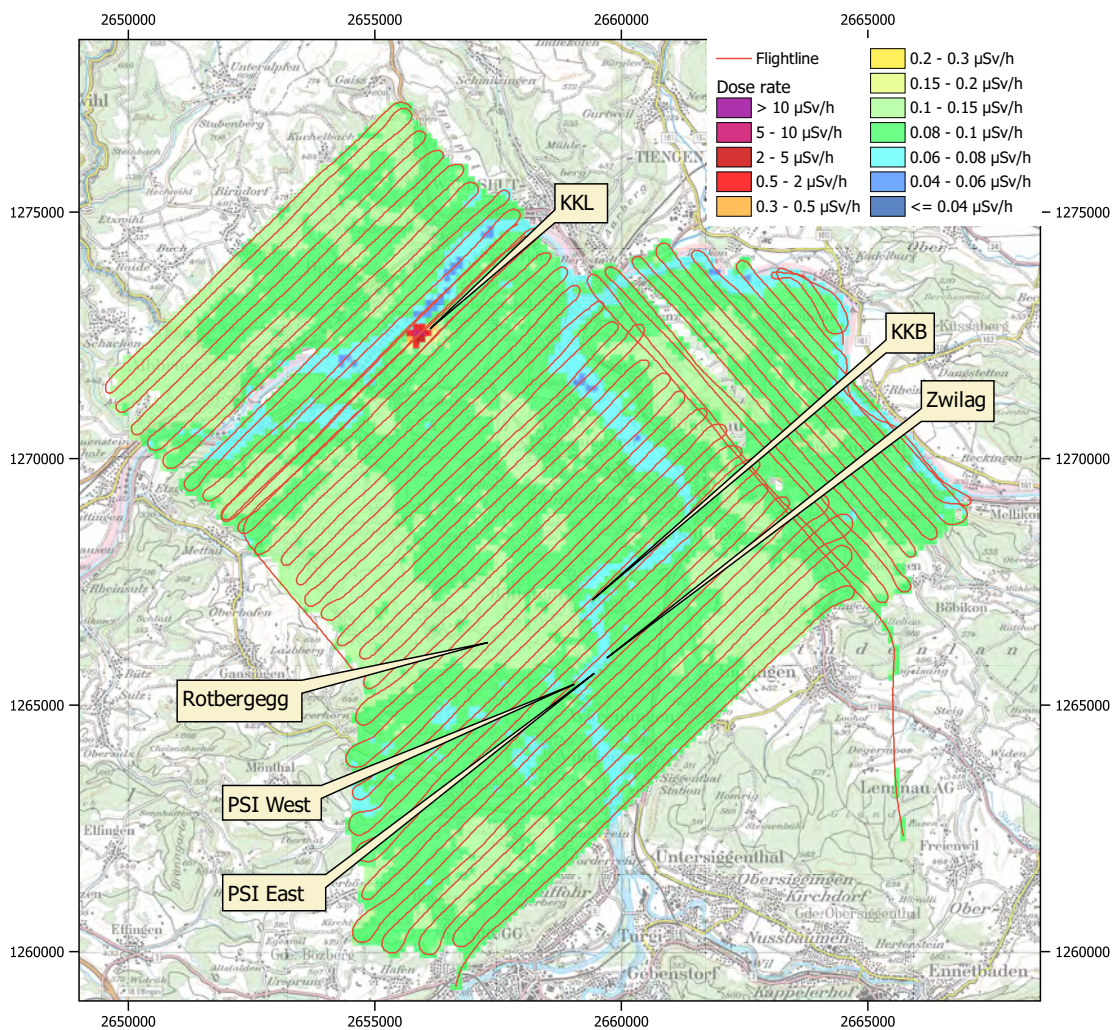

Figure 32: Dose rate in the measurement area KKB, KKL, PSI and Zwilag. PK100 ©2020swisstopo (JD100042).
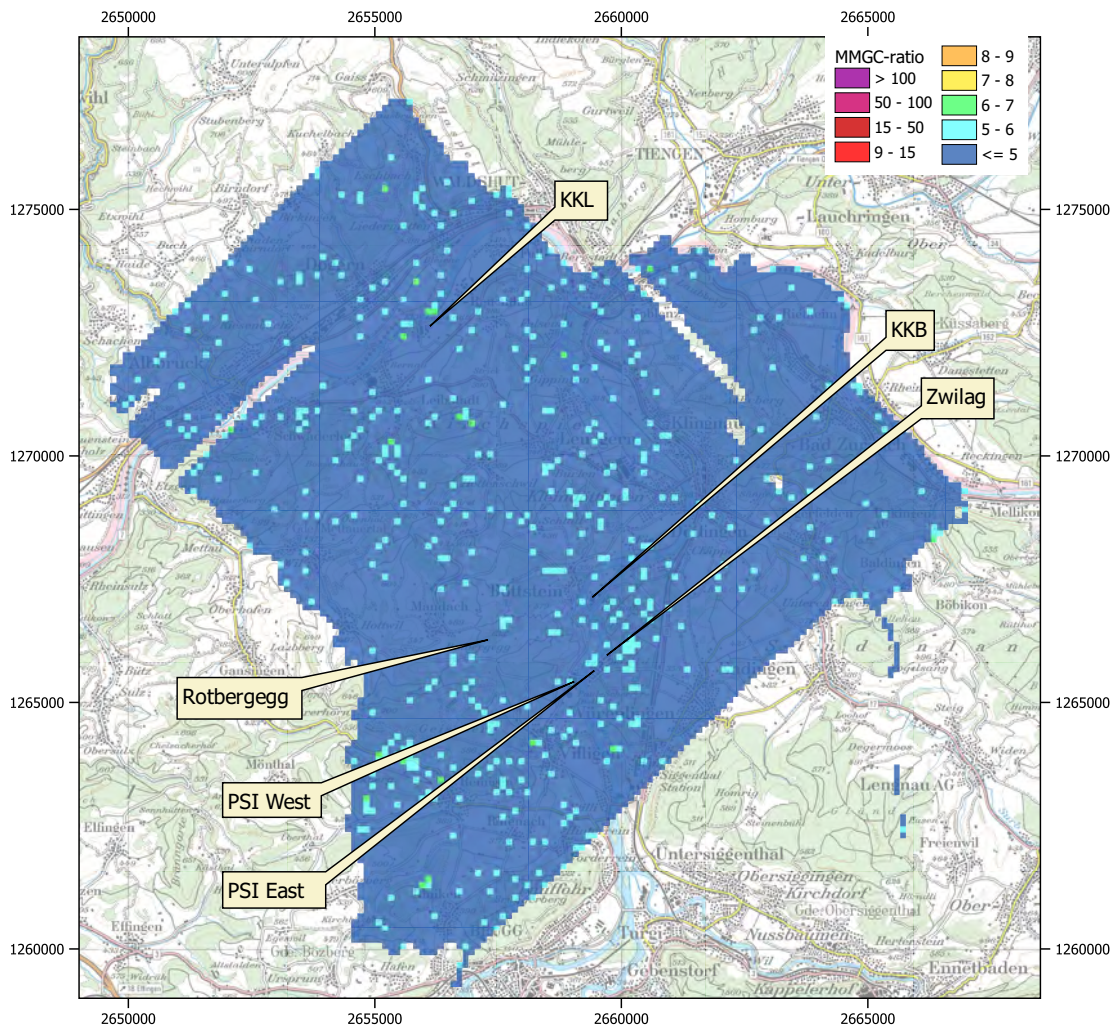
41

Figure 33: MMGC-ratio in the measurement area KKB, KKL, PSI and Zwilag. PK100 ©2020 swisstopo (JD100042).
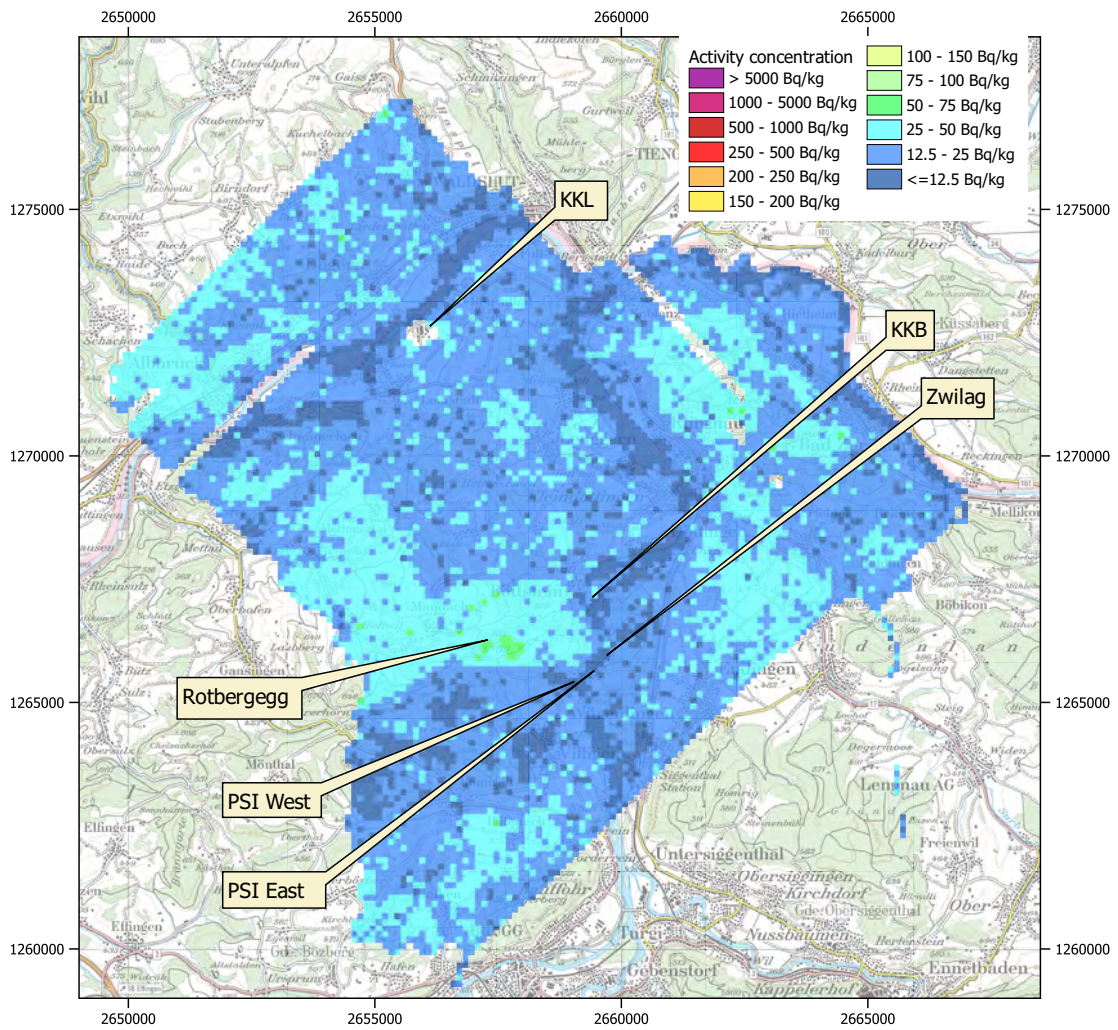
Figure 34: ^{232}Th activity concentration in the vicinity KKB, KKL, PSI and Zwilag. PK100 ©2020 swisstopo (JD100042).

2.1.4 Region between Brugg and Zürich

The region between Brugg and Zürich was measured to add information on sector 2 of the emergency management zone of KKL and KKB and to add to the aeroradiometric coverage of Swiss terrain. The dose rate map (Figure 35) and the map of ^{232}Th activity concentration (Figure 37) show typical values for northern Switzerland. The map of the MMGC-ratio (Figure 36) shows no indication for the presence of man-made radionuclides.
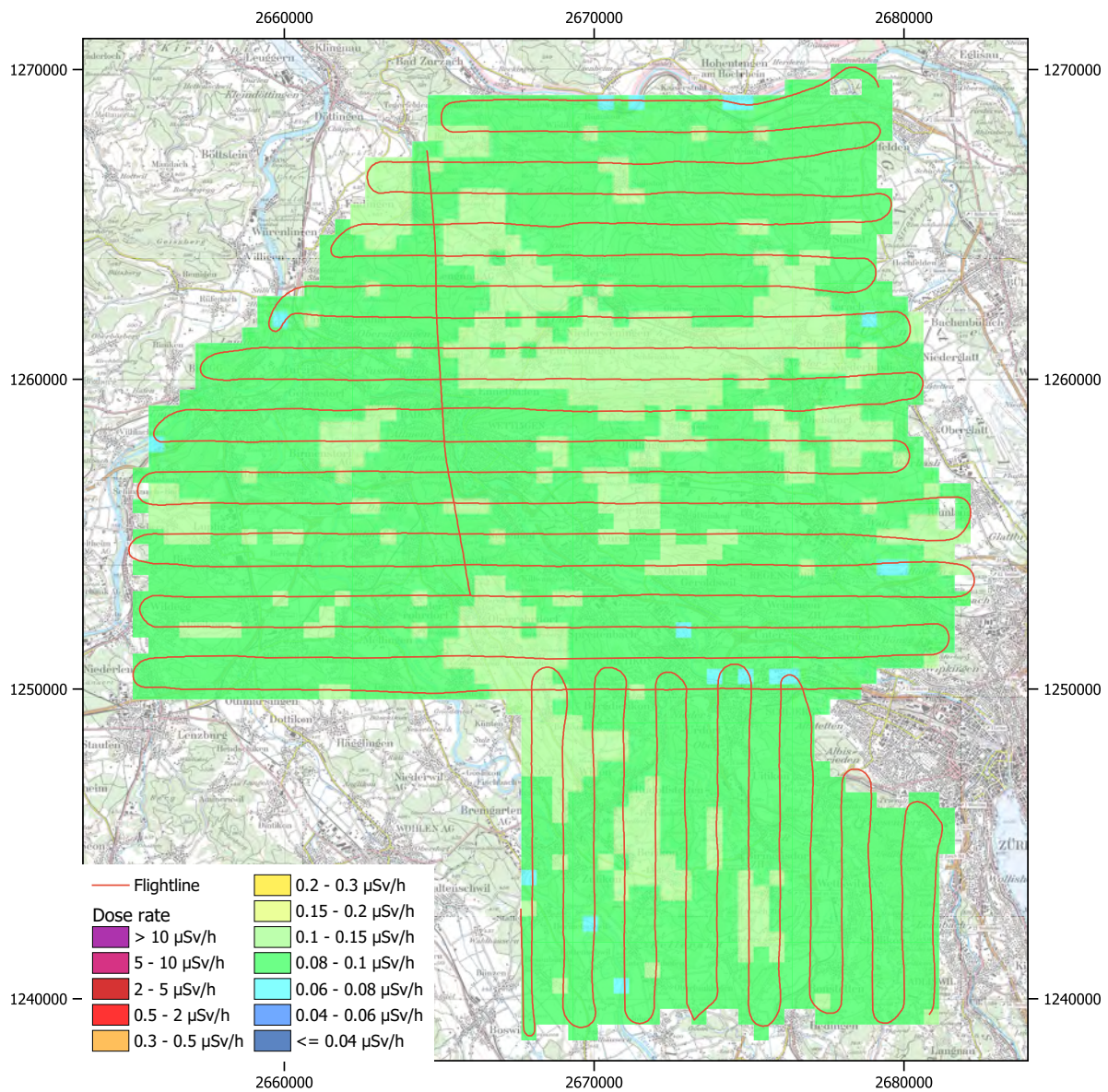

Figure 35: Dose rate in the region between Brugg and Zürich.
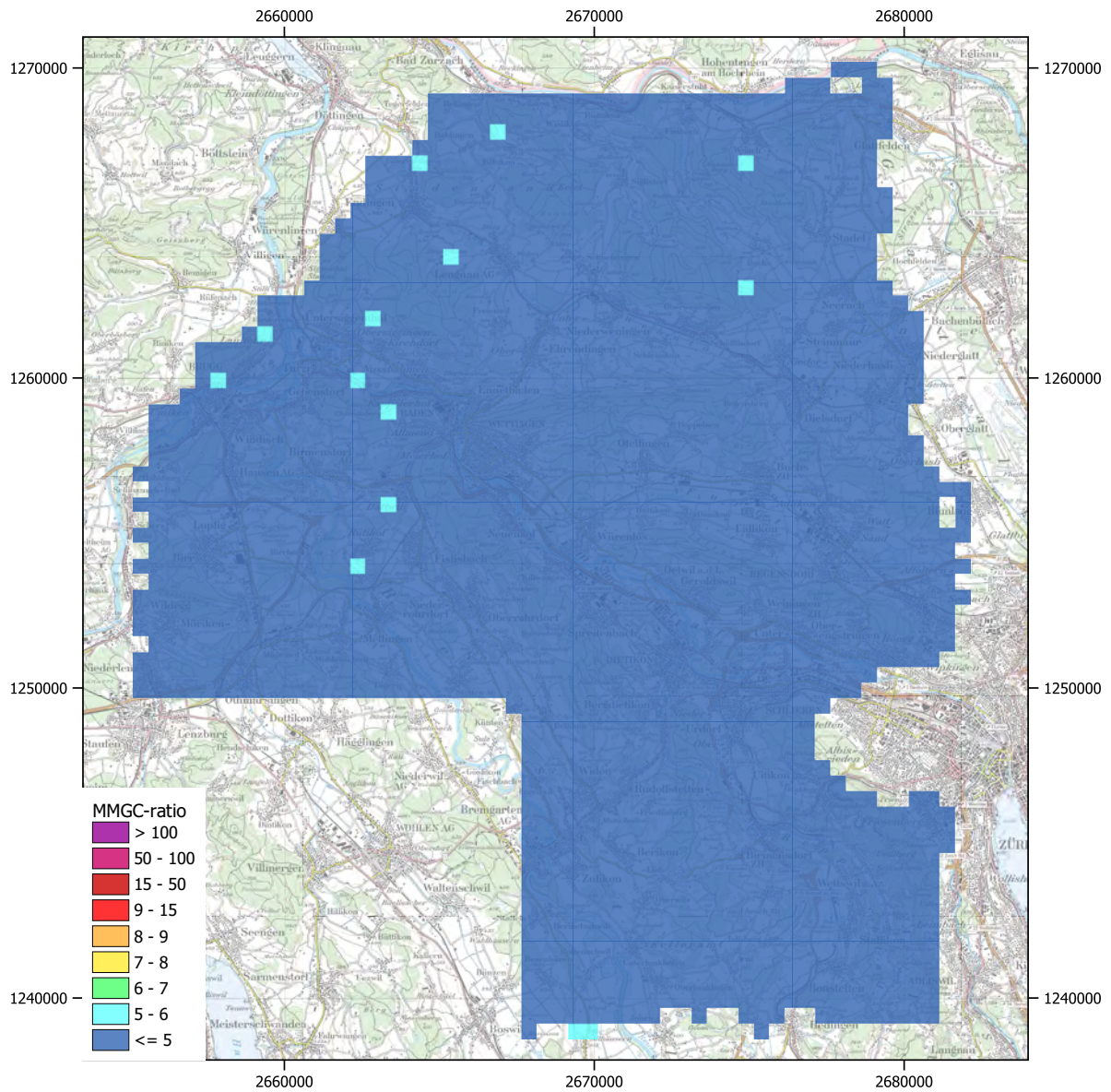PK100 ©2020 swisstopo (JD100042).

Figure 36: Man-made Gross-count (MMGC) ratio in the region between Brugg and Zürich. PK100 ©2020 swisstopo (JD100042).
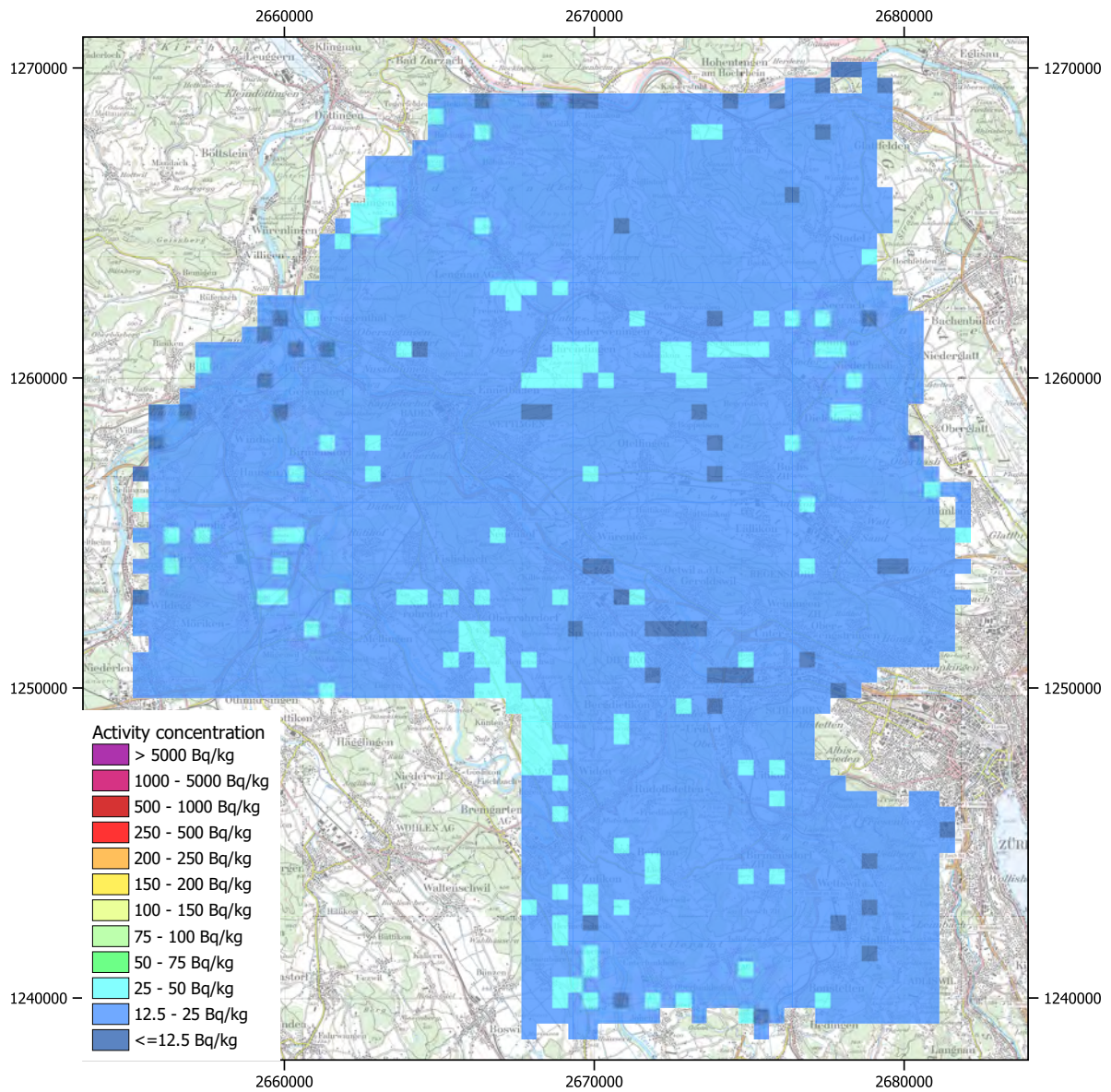
Figure 37: ^{232}Th activity concentration in the region between Brugg and Zürich. PK100 ©2020 swisstopo (JD100042).

2.1.5 Shore of Lake Zurich

Part of the shore of Lake Zurich was inspected during ARM20c to complement background measurements over Zurich and adjacent communities performed in 2012 and 2017. Two flights were performed on June 17th, but the second flight in the area south of Lake Zurich had to be cut short due to the start of heavy rain in the measurement area. The measurement was partly repeated on June 19th.

Airborne radioactive radon progeny is washed from the atmosphere together with rain or snow and deposited on the ground. This effect is clearly visible by comparing the maps of the short-lived radon progeny ^{214}Bi with and without rain (Figures 44 and 45, respectively). As the 1765 keV emission of ^{214}Bi is used to determine the ^{238}U activity concentration in soil and rock, the according activity concentration would be overestimated due to the radon progeny wash-out.

The additional radon progeny activity deposited on the ground increases also the dose rate as can be seen comparing the according maps (Figures 38 and 39, respectively). The measurement of the activity concentrations of the natural radionulides ^{40}K and ^{232}Th are not effected significantly (Figures 42 to 47) and show typical values for northern Switzerland. The values are lower over lake Zurich due to the absorption in the water layer of photons emitted by the terrestrial radionuclides. The maps of the MMGC-ratio (Figure 40 and Figure 41) show both no indication for the presence of man-made radionuclides. Some MMGC-ratios are slightly elevated due to very low count rates associated with natural radionuclides, like for example the yellow square at coordinate 2685356, 1243339 in Figure 40, where this signal is attenuated by the water layer.
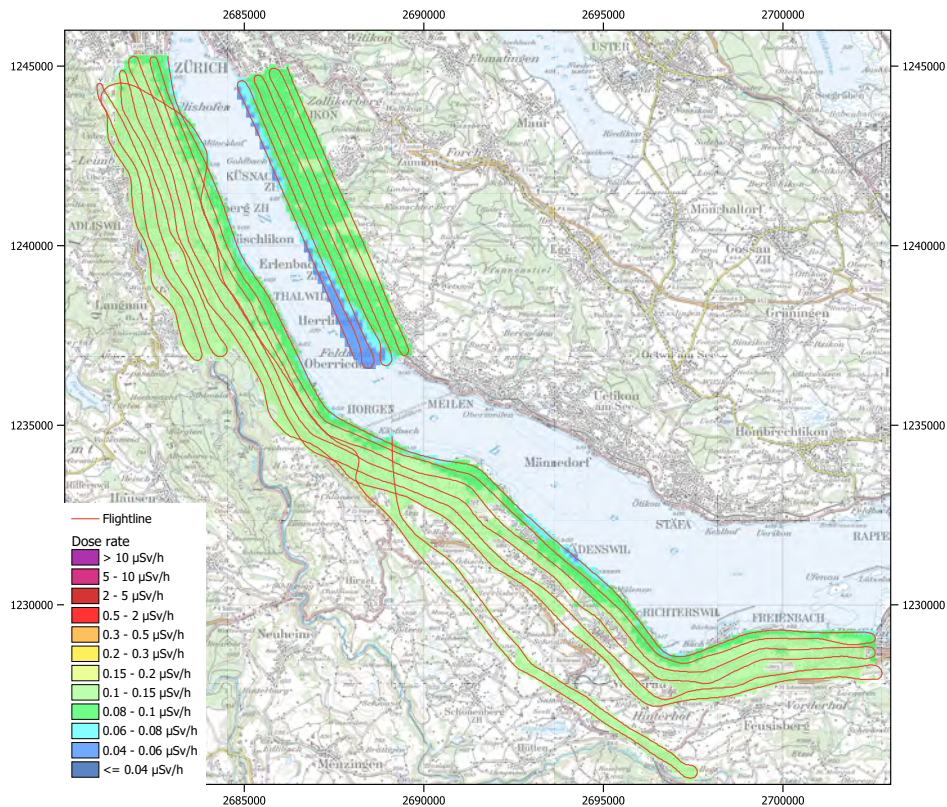
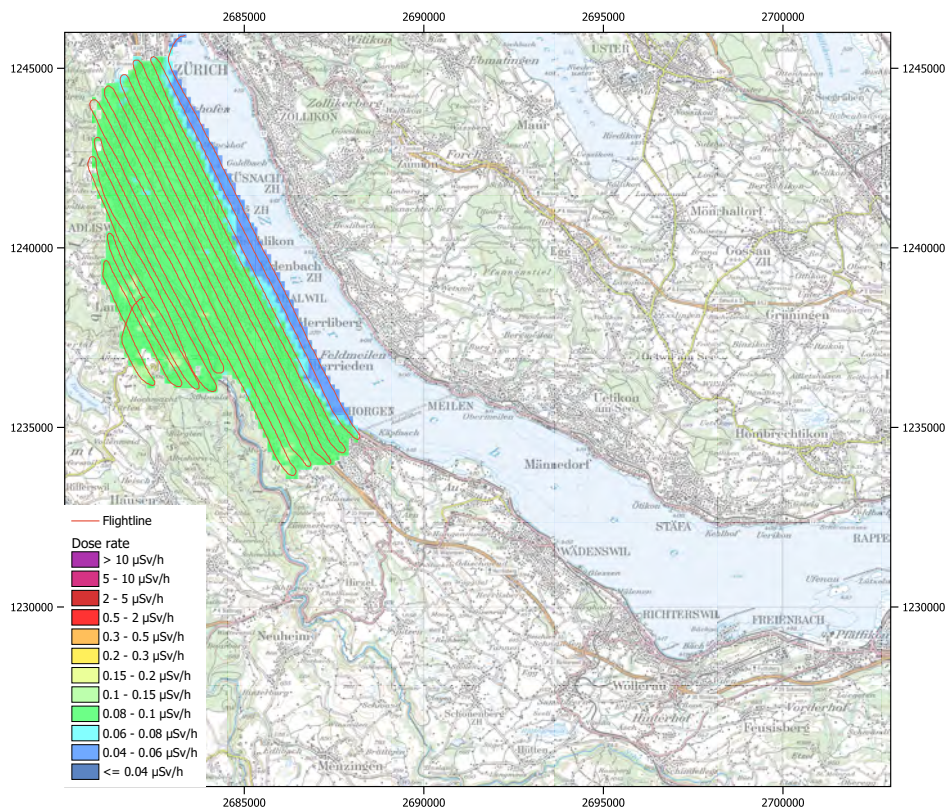Figure 38: Dose rate at the shore of Lake Zurich measured during rain. PK100 ©2020 swisstopo (JD100042).

Figure 39: Dose rate at the shore of Lake Zurich. PK100 ©2020 swisstopo (JD100042).
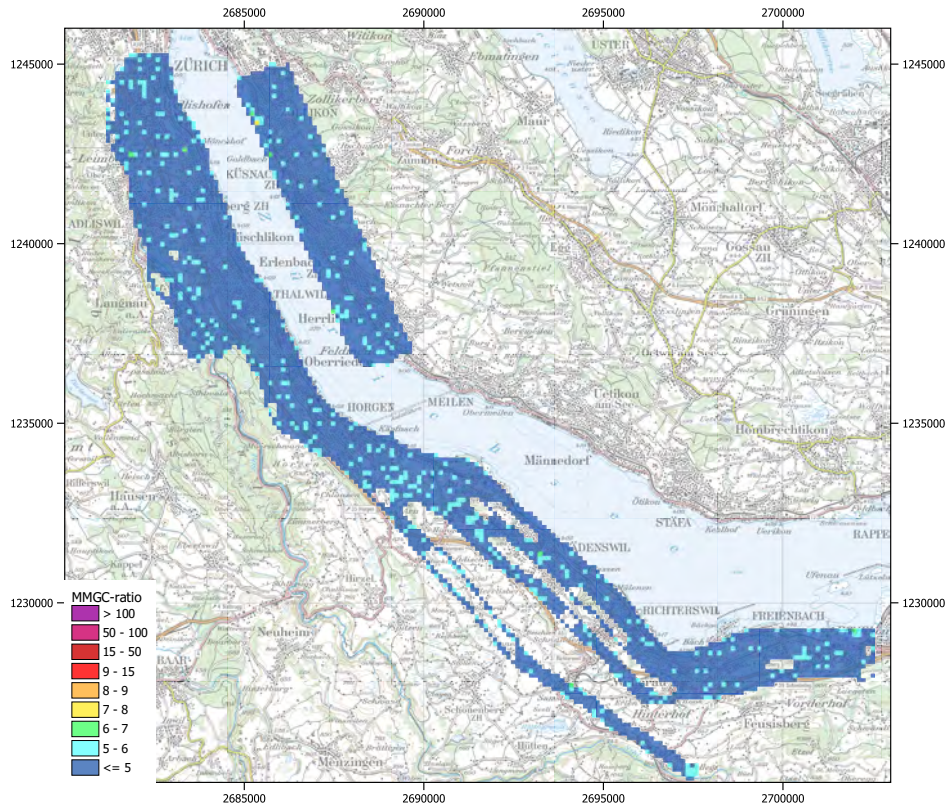
Figure 40: Man-made Gross-count (MMGC) ratio at the shore of Lake Zurich measured during rain. PK100 ©2020 swisstopo (JD100042).
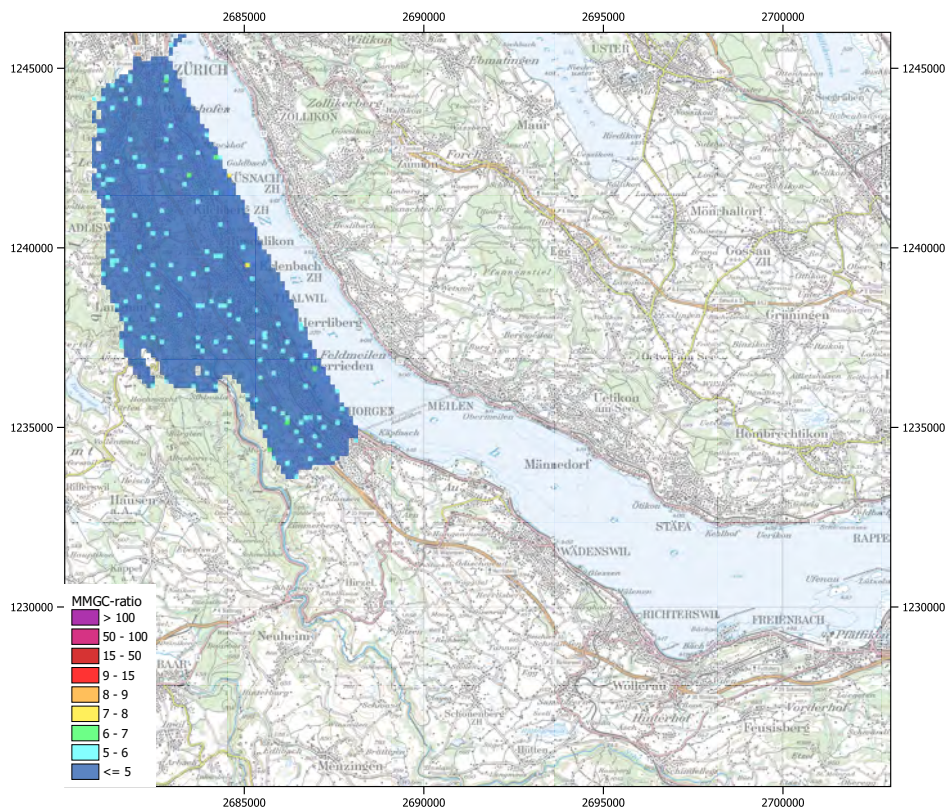

Figure 41: Man-made Gross-count (MMGC) ratio at the shore of Lake Zurich. PK100 ©2020 swisstopo (JD100042).
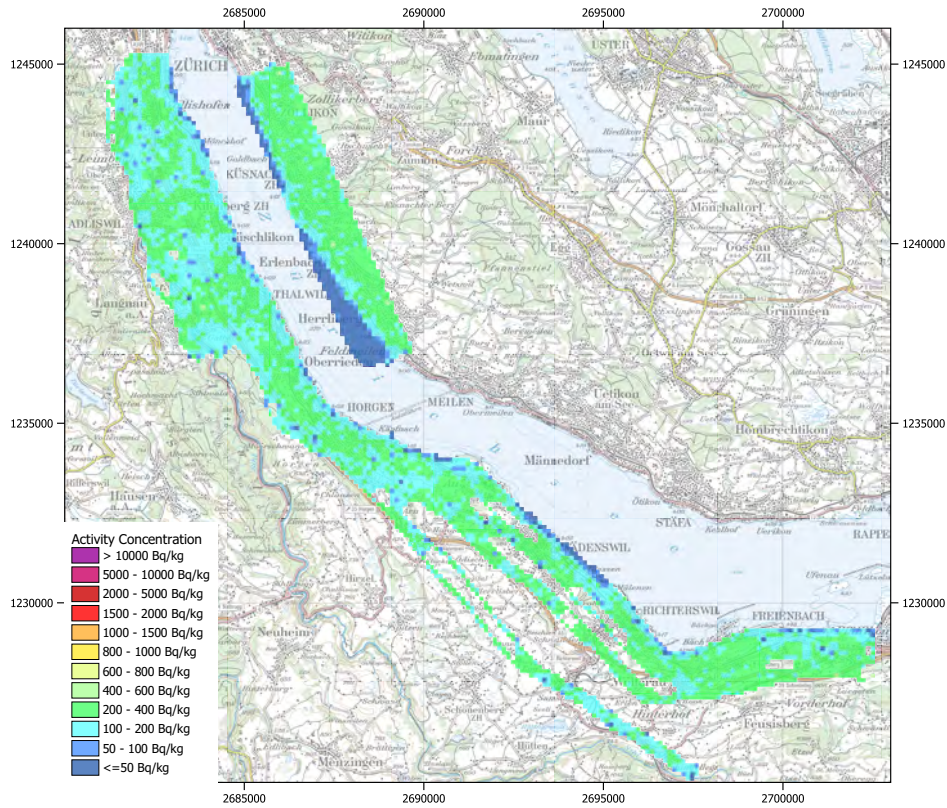
Figure 42: ^{40}K activity concentration at the shore of Lake Zurich measured during rain.
PK100 ©2020 swisstopo (JD100042).

Figure 43: ^{40}K activity concentration at the shore of Lake Zurich.
PK100 ©2020 swisstopo (JD100042).

Figure 44: ^{214}Bi activity concentration at the shore of Lake Zurich measured during rain. PK100 ©2020 swisstopo (JD100042).

Figure 45: ^{214}Bi activity concentration at the shore of Lake Zurich. PK100 ©2020 swisstopo (JD100042).
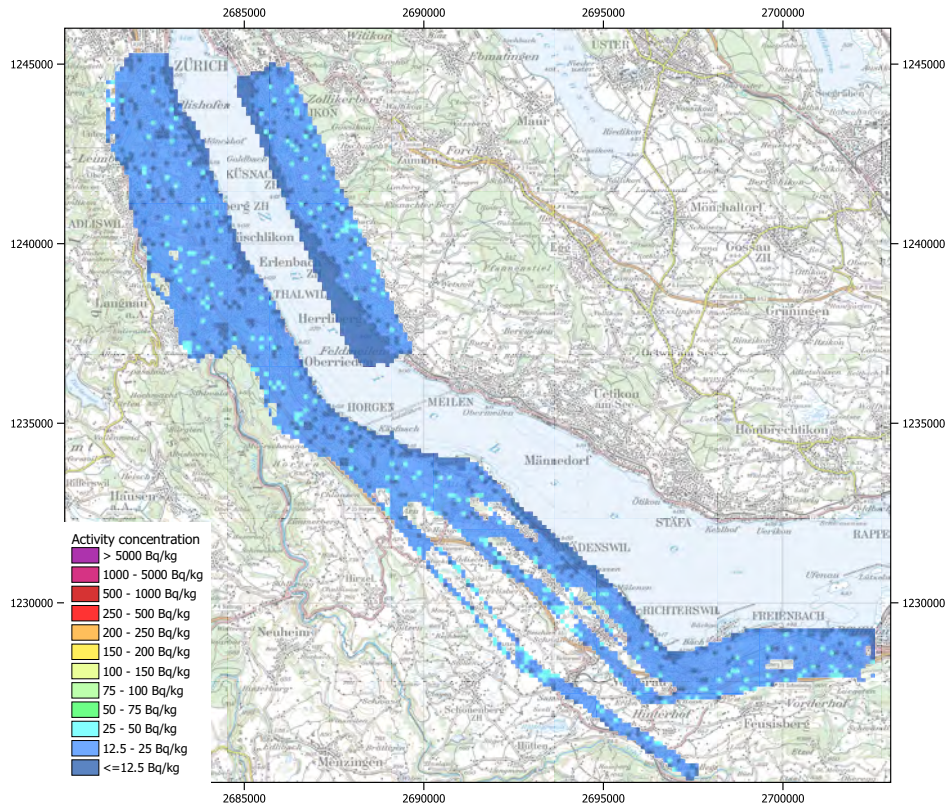
Figure 46: ^{232}Th activity concentration at the shore of Lake Zurich measured during rain. PK100 ©2020 swisstopo (JD100042).
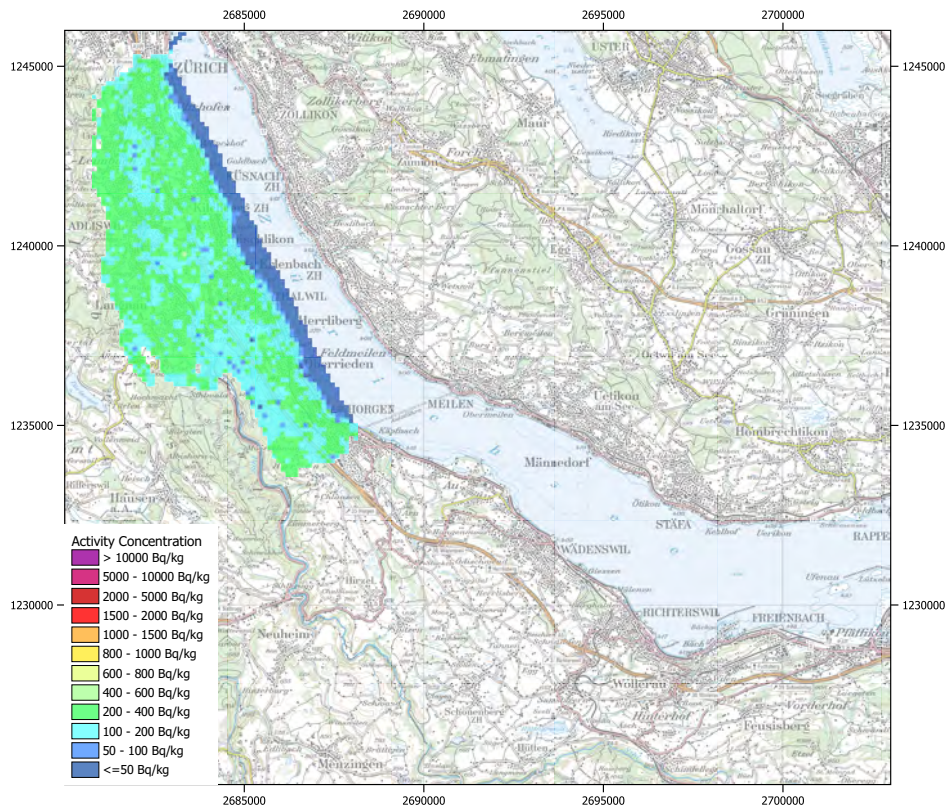

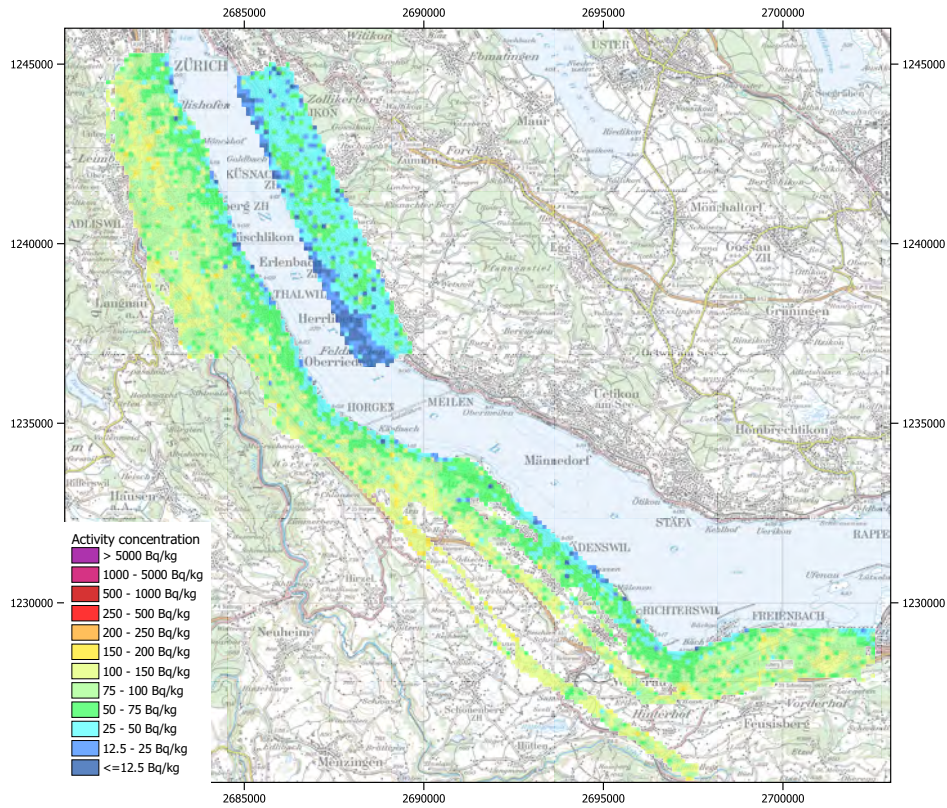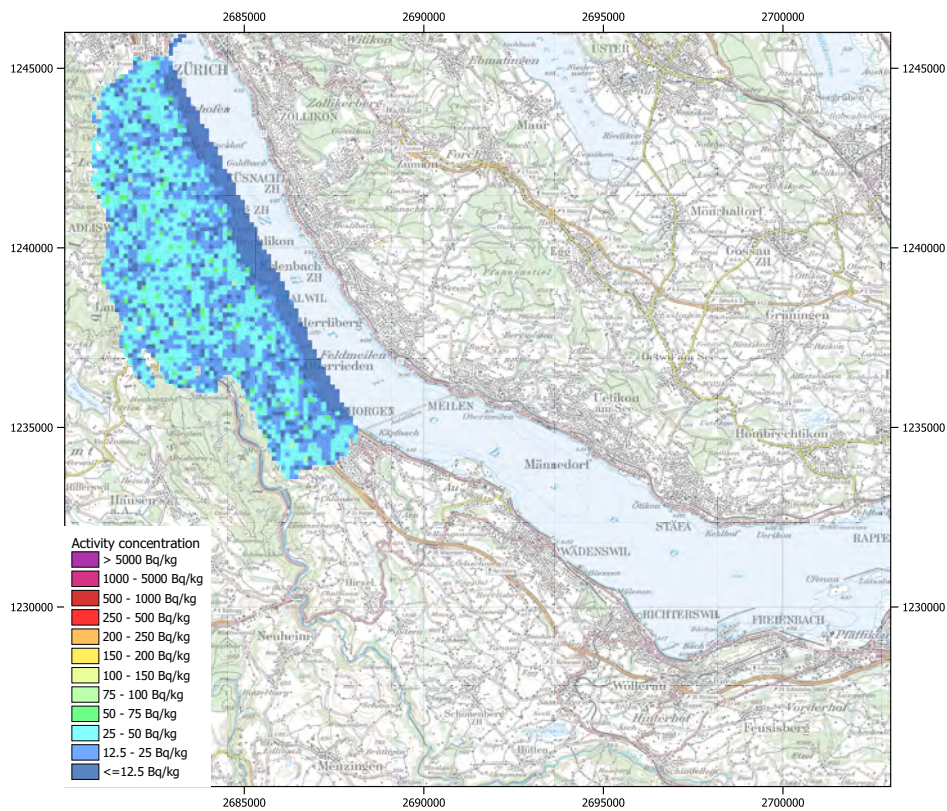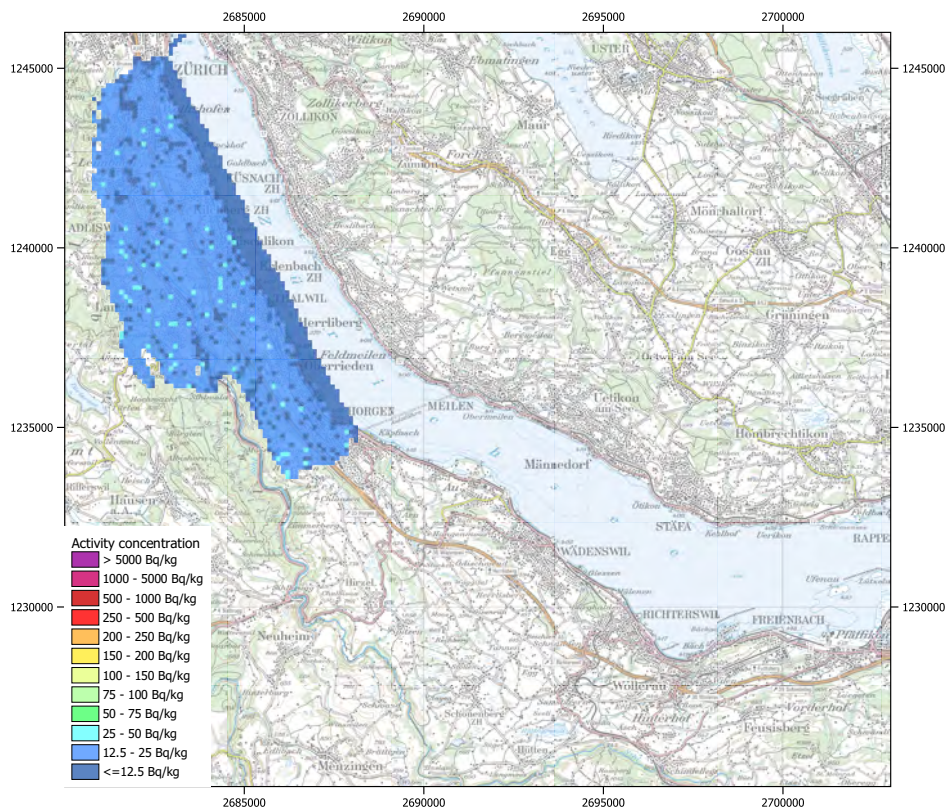Figure 47: ^{232}Th activity concentration at the shore of Lake Zurich. PK100 ©2020 swisstopo (JD100042).

2.1.6 St. Gallen

The series of radiological background measurements over Swiss cities was complemented with measurements over St. Gallen in eastern Switzerland. The maps of dose rate (Figure 48) and the ^{232}Th activity concentration (Figure 50) indicate no anomalies. The map of the MMGC-ratio (Figure 49) shows the low values associated with solely natural radionuclides.

Figure 48: Dose rate over the City of St. Gallen. PK100 ©2020 swisstopo (JD100042).

Figure 49: Man-made Gross-count (MMGC) ratio over the City of St. Gallen. PK100 ©2020 swisstopo (JD100042).
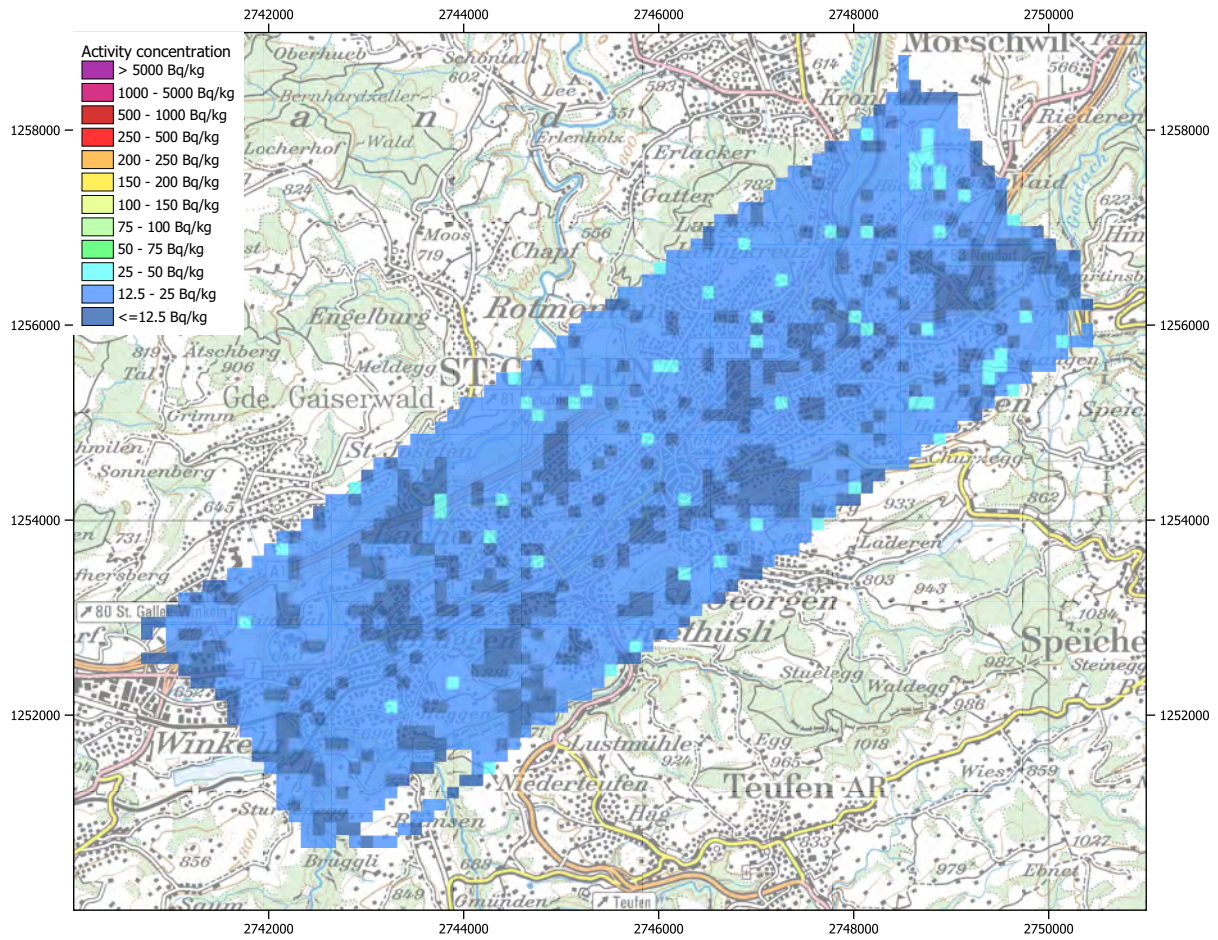
Figure 50: ^{232}Th activity concentration over the City of St. Gallen. PK100 ©2020 swisstopo (JD100042).

2.2 ARM20m

2.2.1 Mont Pelé
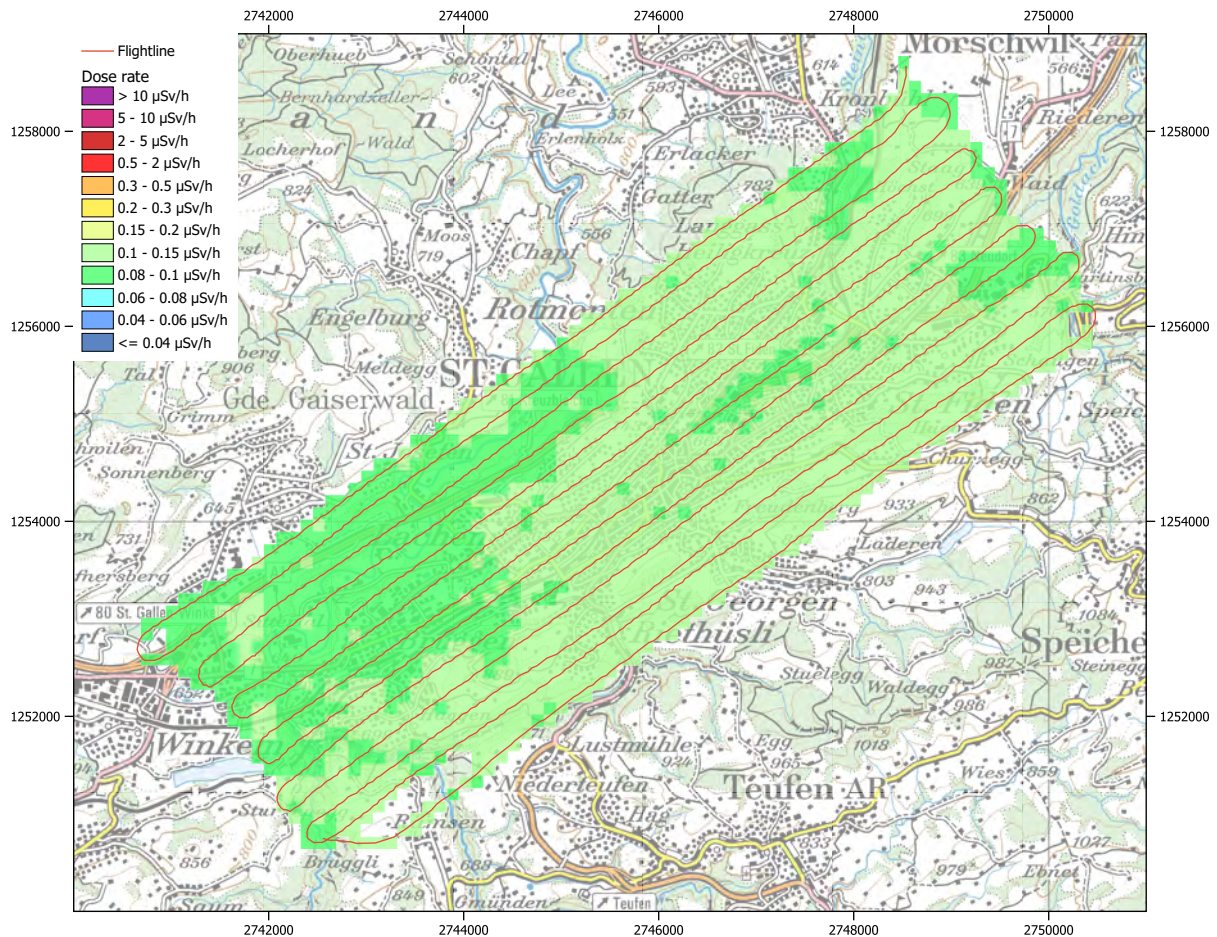
Besides the south and east of Switzerland, the westernmost part of Switzerland was exposed to some rain-out during the Chernobyl accident in 1986, depositing ^{137}Cs on the ground. A measurement flight in an area west of the mountains Noirmont and Mont Pelé near the French border in western Switzerland was performed to check on the still remaining ^{137}Cs activity in the ground. Neither dose rate map (Figure 51) nor the map of the MMGC-ratio (Figure 52) indicate significant ^{137}Cs activity concentrations. This result is confirmed by the map of ^{137}Cs activity concentrations (Figure 53). The activity concentration averaged over the complete measuring area of 14 Bq/kg or 250 Bq/m^2, respectively, is still below the detection limit of the RLL aeroradiometric system. The map of the natural radionuclide ^{232}Th shows slightly larger values toward the valley, while still remaining in a typical concentration range.
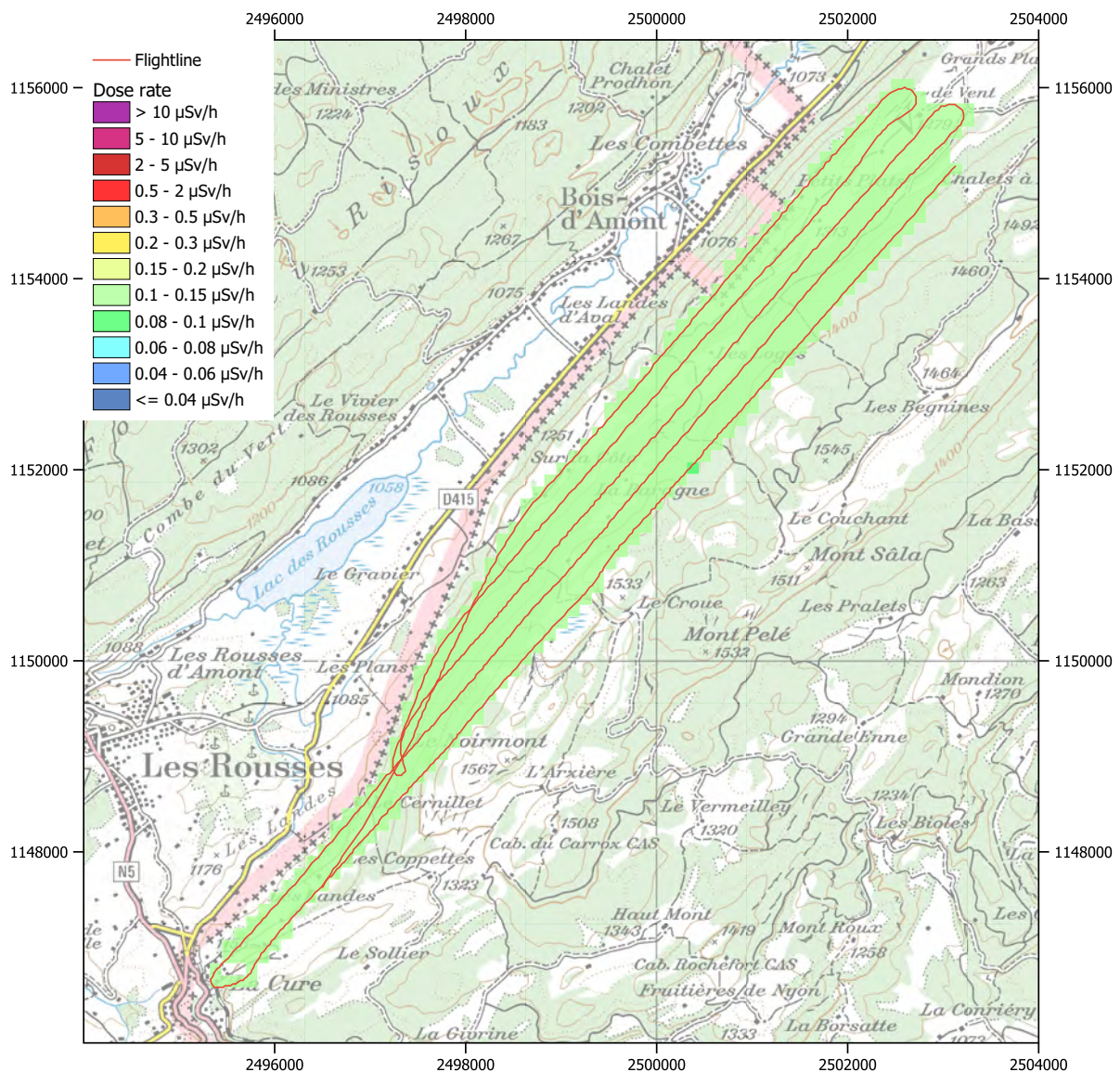
Figure 51: Dose rate near Mont Pelé. PK100 ©2020 swisstopo (JD100042).

Figure 52: Man-made Gross-count (MMGC) ratio near Mont Pelé.
PK100 ©2020 swisstopo (JD100042).

Figure 53: ^{137}Cs activity concentration near Mont Pelé.
PK100 ©2020 swisstopo (JD100042).
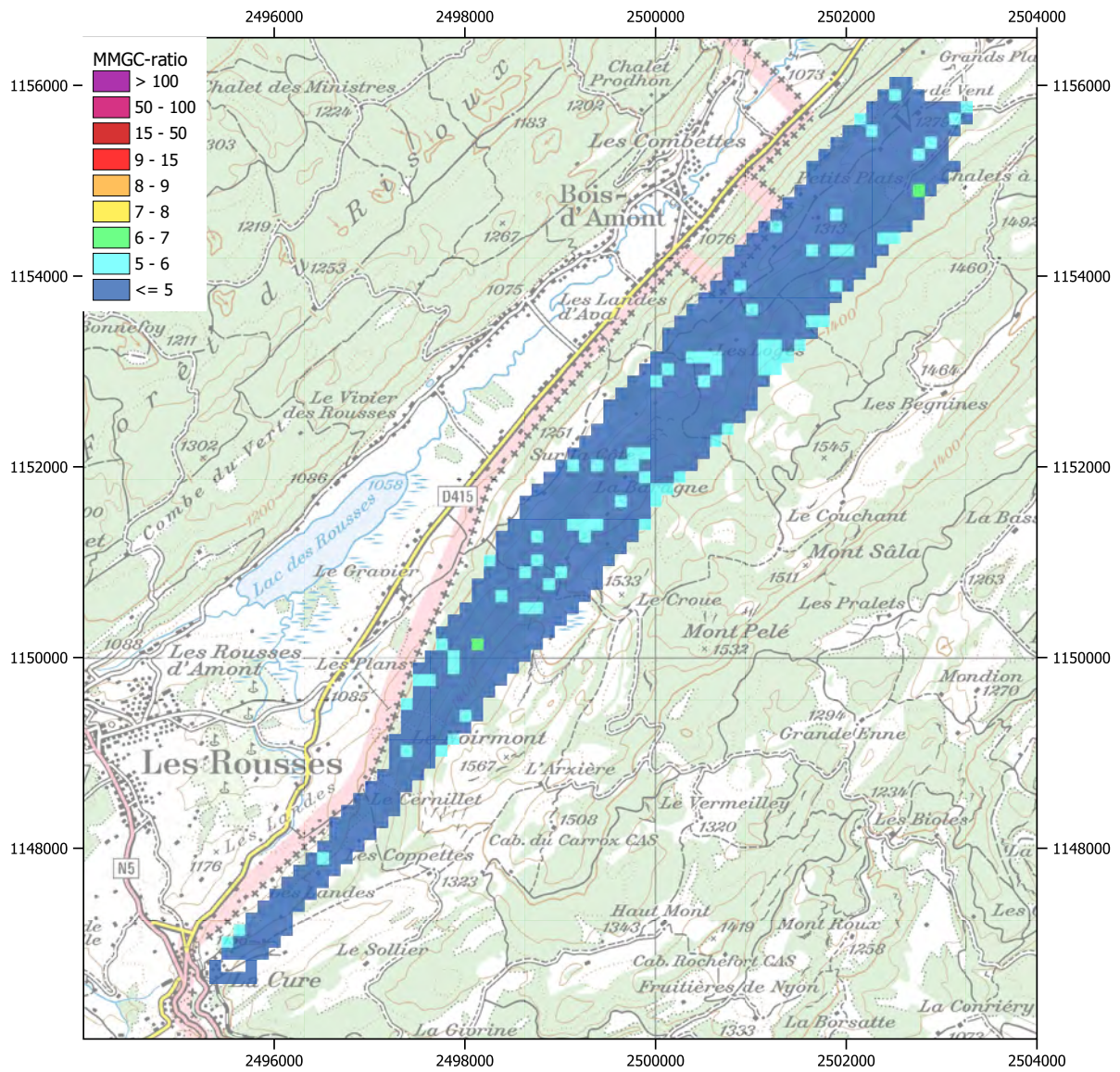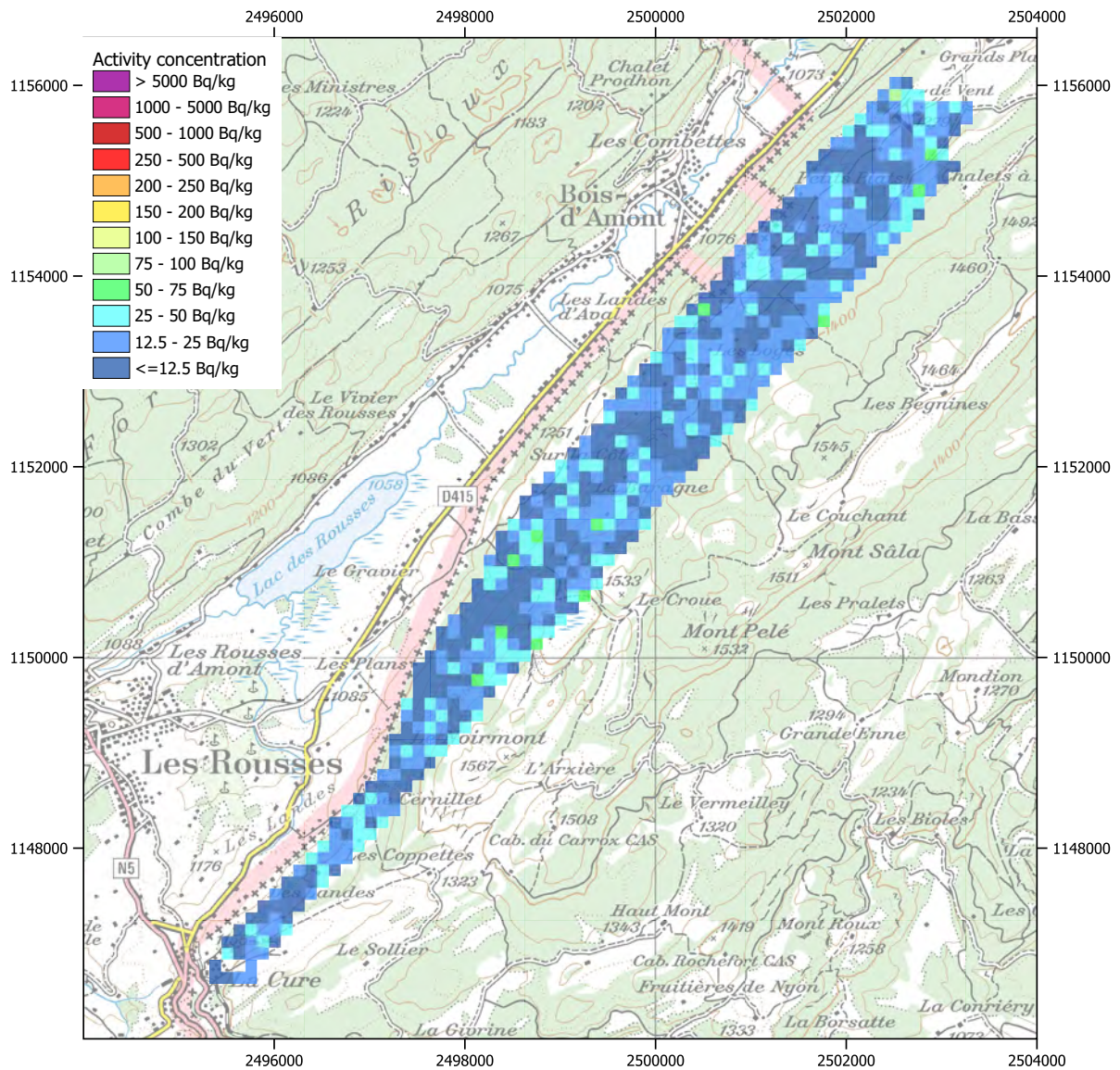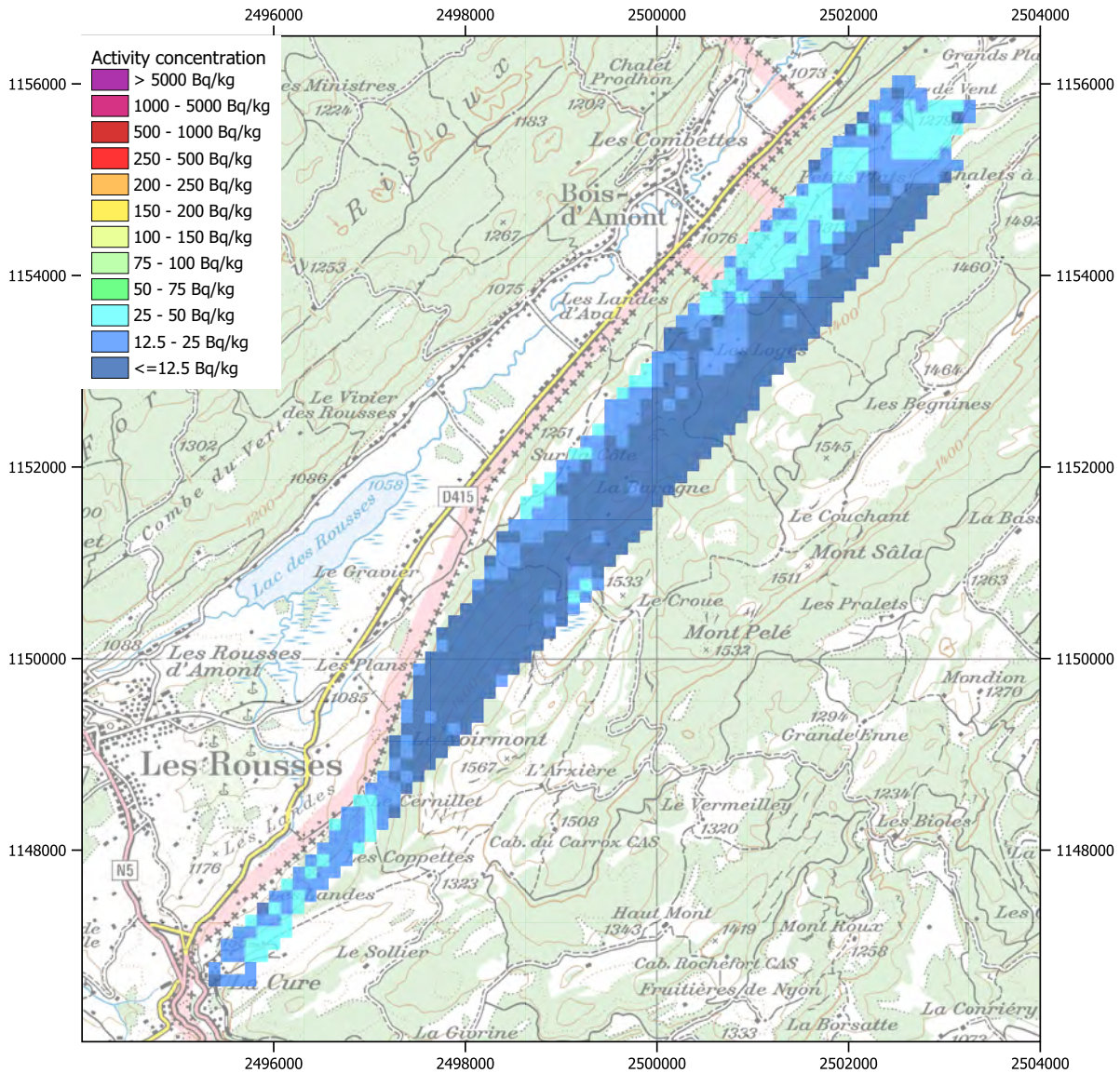
Figure 54: ^{232}Th activity concentration near Mont Pelé.
PK100 ©2020 swisstopo (JD100042).

2.2.2 Region north of Lake Geneva

A large region north of Lake Geneva was measured during the exercise ARM20m adding to the aeroradiometric coverage of Switzerland and complementing the series of background measurements over Swiss cities with the city of Lausanne. The map of the dose rate (Figure 55) shows clearly the influence of the photon attenuating water layer of Lake Geneva. The ^{232}Th activity concentration displays typical values, which are slightly lower in the centre of the measured area (Figure 56), reflecting the geology of the region (Figure 57). No presence of man-made radionuclides is indicated by the MMGC-ratio (Figure 58).

Figure 55: Dose rate north of Lake Geneva. PK100 ©2020 swisstopo (JD100042).

Figure 56: ^{232}Th activity concentration north of Lake Geneva. PK100 ©2020 swisstopo (JD100042).

Figure 57: Geology north of Lake Geneva. Legend see Figure 59. Geological map ©2020 swisstopo (JD100042).

Figure 58: Man-made Gross-count (MMGC) ratio north of Lake Geneva. PK100 ©2020 swisstopo (JD100042).

Figure 59: Legend of geological map (in German). Geological map ©2020 swisstopo (JD100042).

3 Conclusions

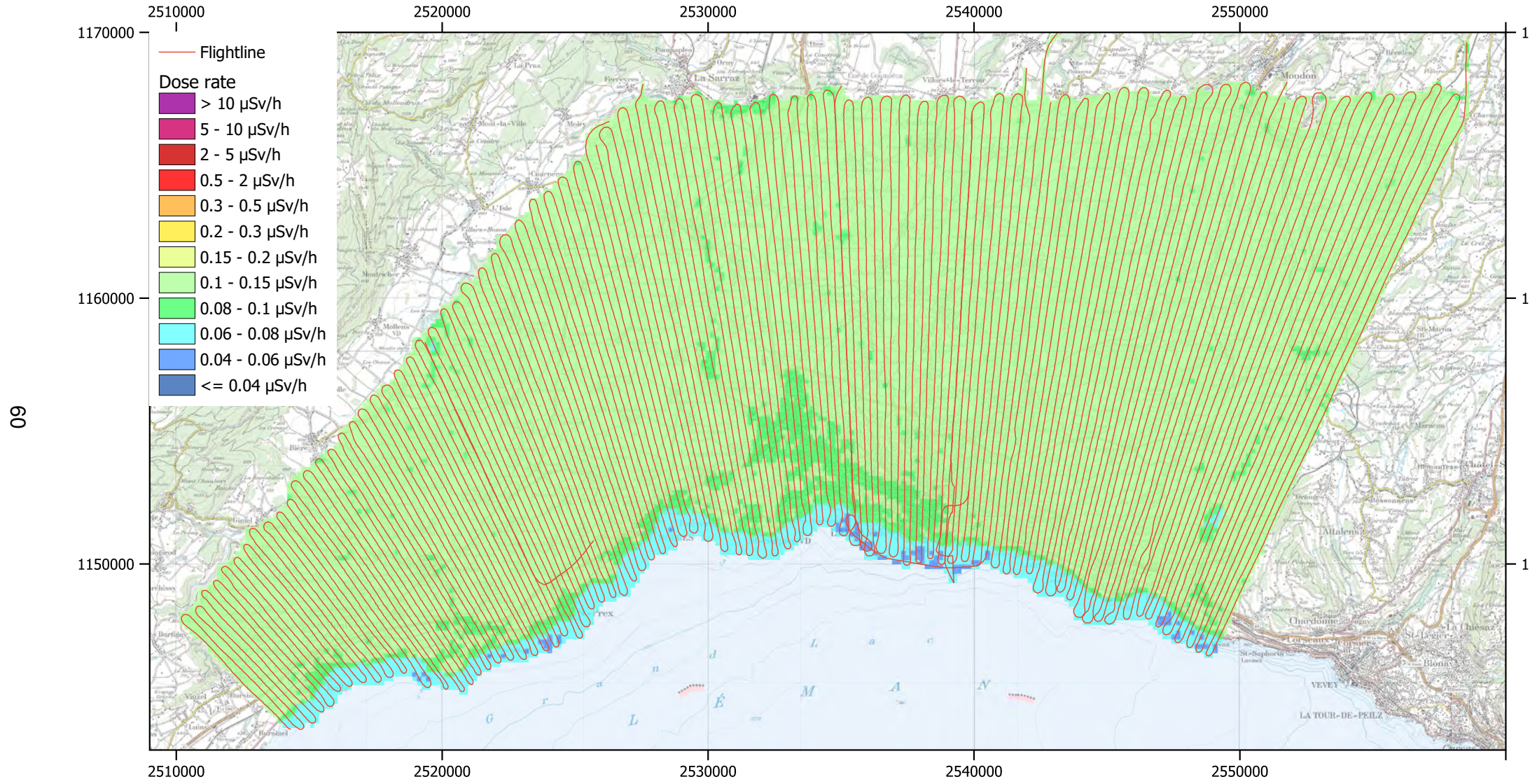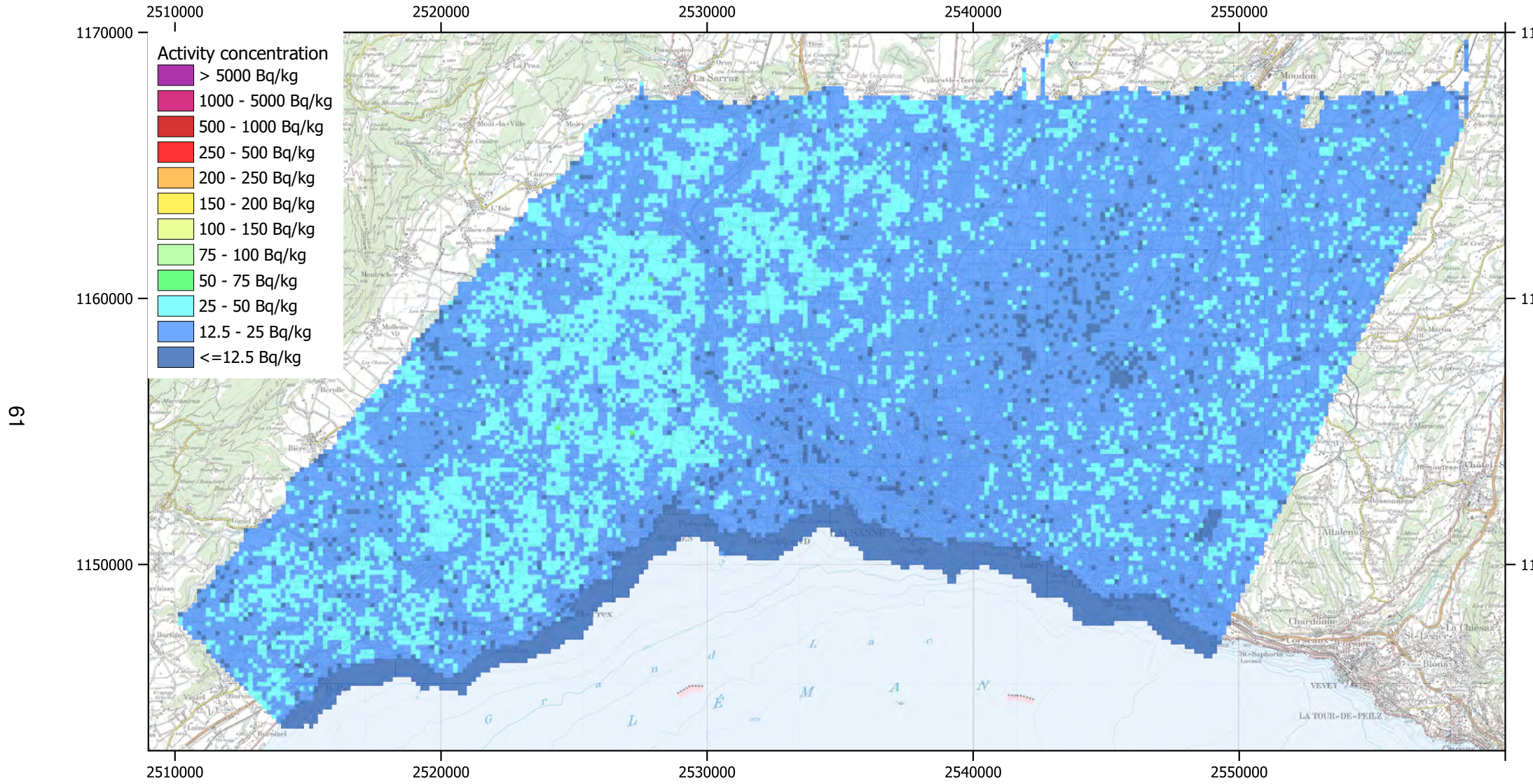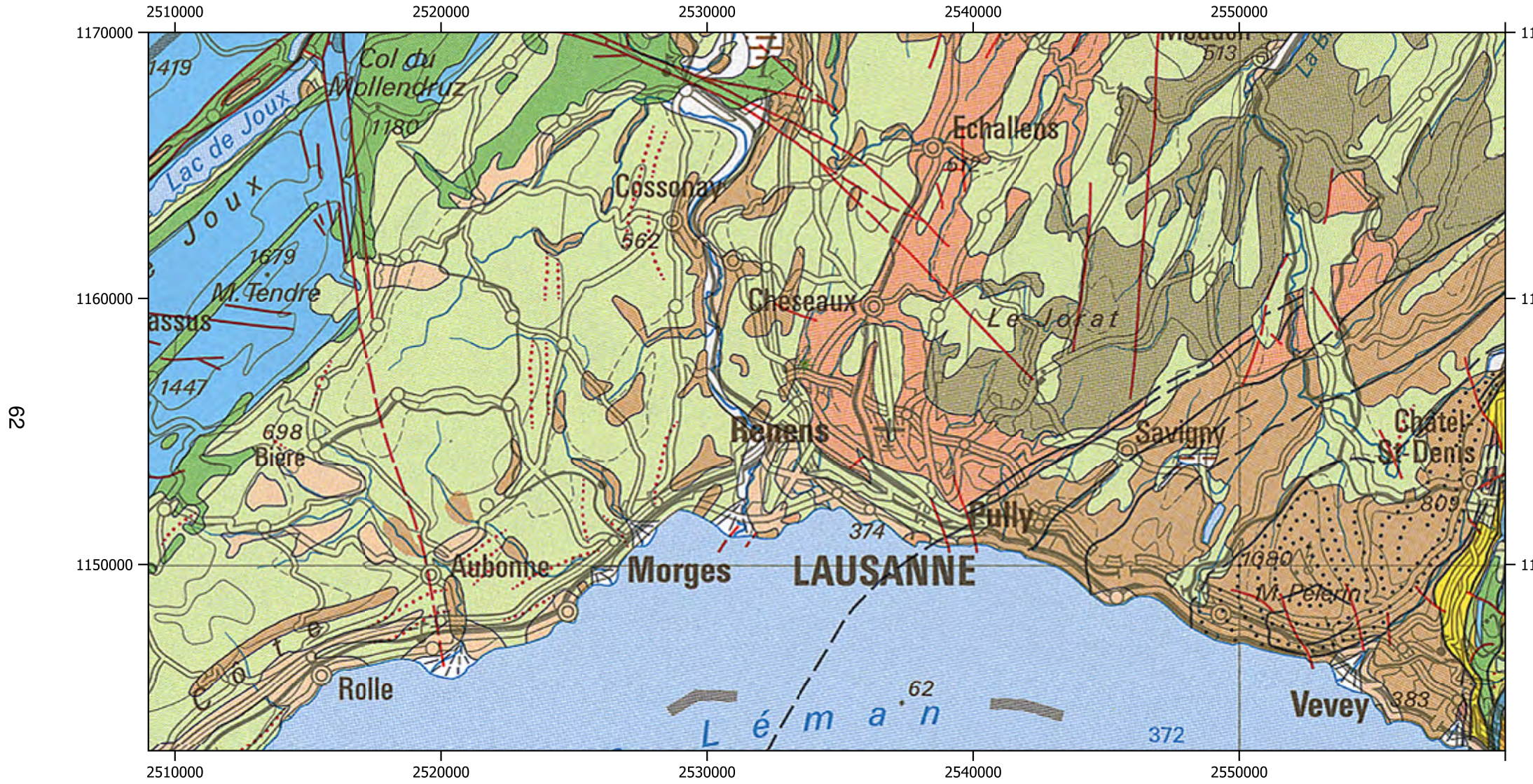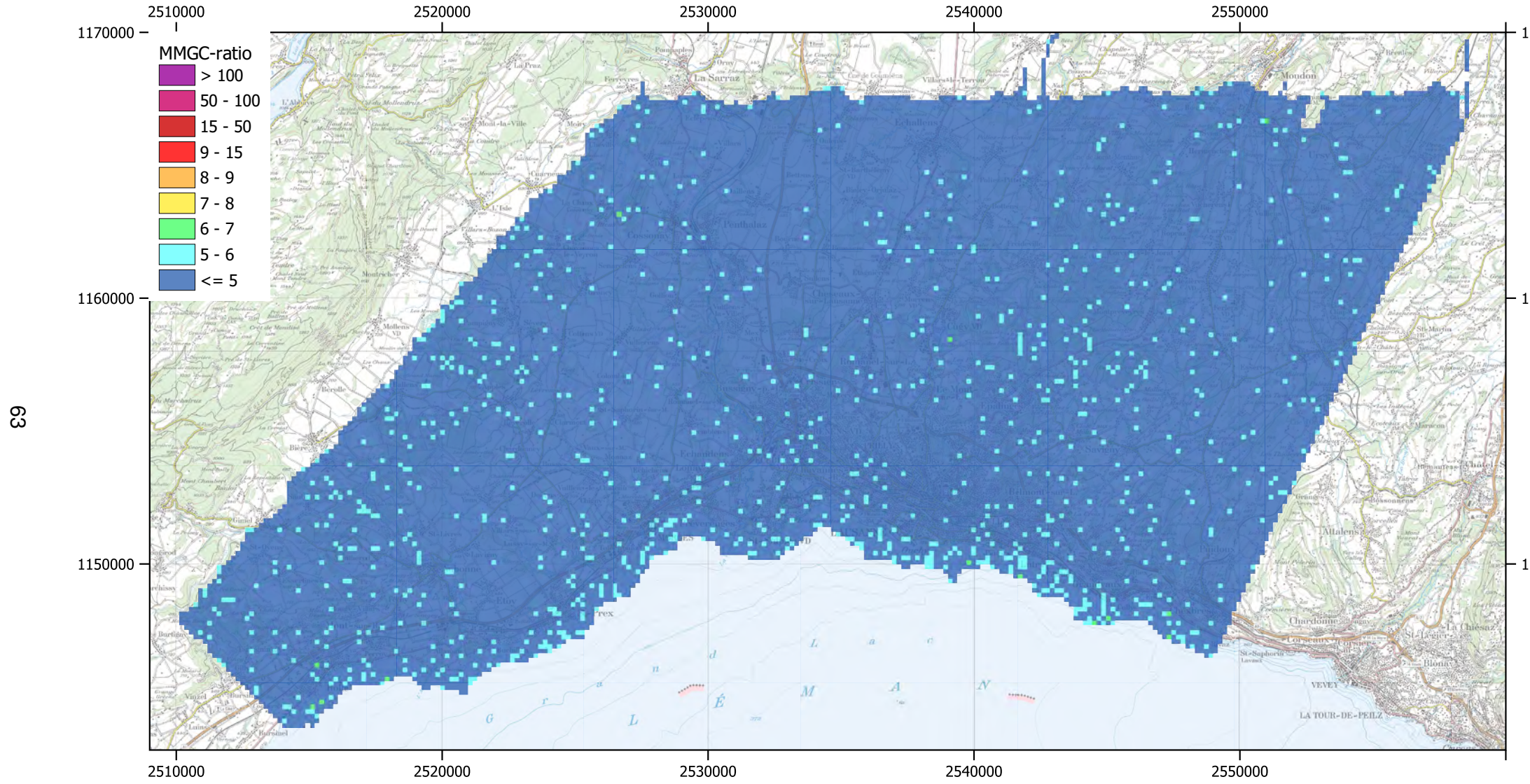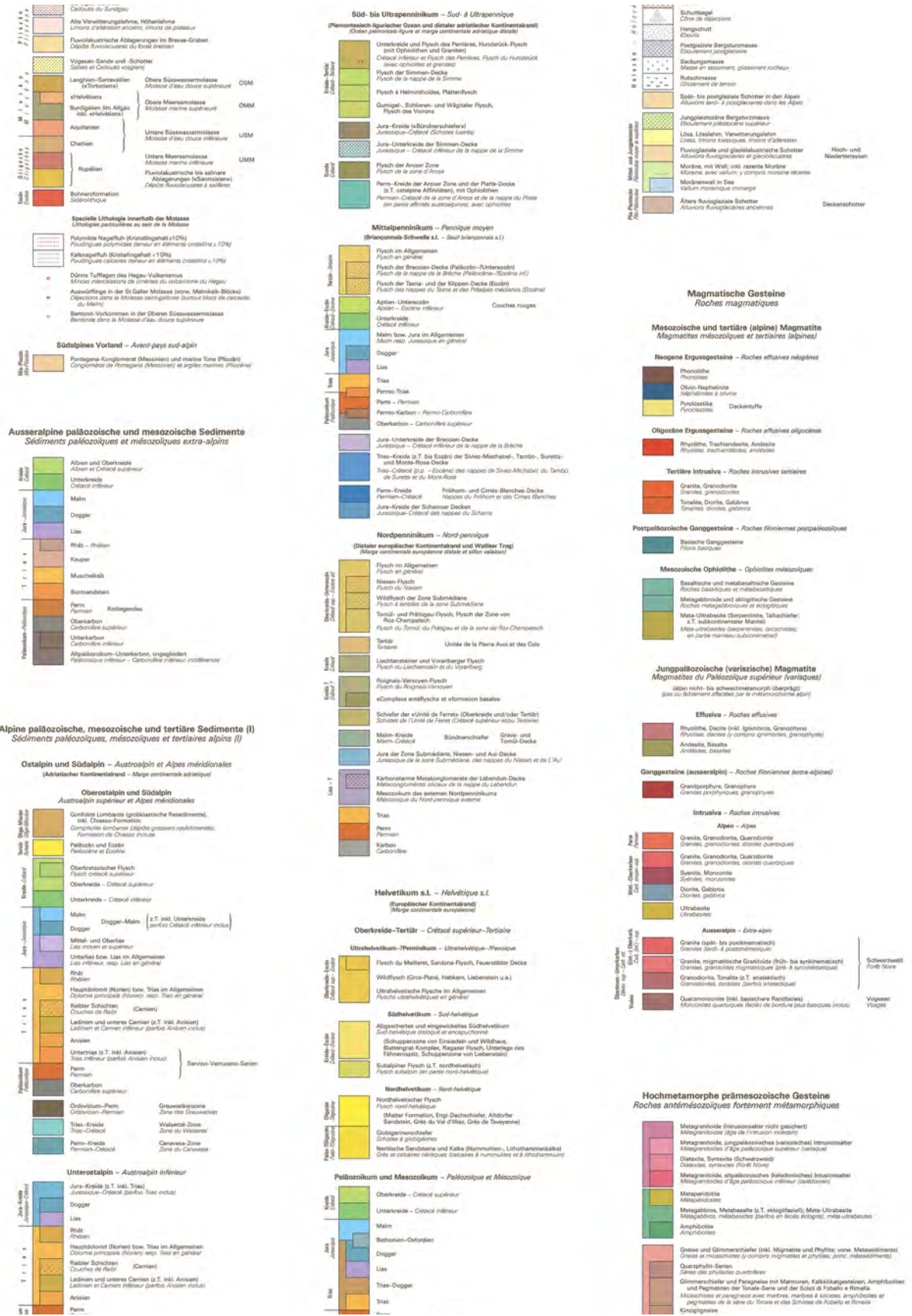Several changes were bundled into the present report. The data evaluation was performed with a new software developed in the .net environment. Raw data, evaluated data and parameters used in the evaluation for each measuring area are stored together in a single text file using the ERS 2.0 format description (see PSI report 18-04). The colour gradient scale used in previous reports was replaced with a discrete colour scale defined by the Swiss Expert Group for Aeroradiometrics (FAR). The reference soil mass was switched from dry weight to wet weight, as the importance of radio-analytical laboratory measurements as reference is diminished in comparison with in-situ gamma-spectrometric ground measurements.

The survey of the environs of the Swiss nuclear power plants Beznau (KKB) and Leibstadt (KKL) and the nuclear facilities of the Paul Scherrer Institute and the Zwischenlager Würenlingen AG showed no artificial radionuclides outside of the plant premises.

Measurements in an area between Brugg and Zurich, over the lakeshore of Lake Zurich and over the town of St. Gallen showed typical values of the natural radionuclides and no indication of man-made radionuclides.

Altitude profiles over Lake Thun were used together with altitude profiles measured in the past to improve the data evaluation procedure for the determination of system background and the influence of cosmic radiation. Deming regression was identified as best method to quantify the assumed linear dependency. The altitude range necessary for a complete evaluation should be at least 2 km. For smaller altitude ranges, the determination of just the intercept (system background) based on an average slope was considered the more robust approach.

A source search exercise and an intercomparison with ground measurements performed on Thun military training ground rendered revised calibration factors for the evaluation of count rates in the respective energy windows.

A fine-meshed survey of a large area north of Lake Geneva showed the influence of attenuation water layers and the underlying geology on the measurement results.

A flight near Mont Pelé in the west of Switzerland measured no ^{137}Cs activities remaining after the Chernobyl accident in 1986 above the detection limit of the aeroradiometric measuring system.

A previously detected rapid degradation of spectrometric performance was not repeated with the detector used in ARM20 after replacement of NaI(Tl) crystals by the manufacturer.

4 Literature

Bucher, B.: Methodische Weiterentwicklungen in der Aeroradiometrie. Dissertation Nr. 13973, ETH Zürich, 2001.

Eidgenössische Kommission für Strahlenschutz und Überwachung der Radioaktivität (KSR): Empfehlung betreffend der Verwendung von Umrechnungsfaktoren h*(10) für die Messung der Umgebungs-Äquivalentdosisleistung H*(10) mittels in situ Gammaspektrometrie, Bern, 2010.

Schwarz, G. F.: Methodische Entwicklungen zur Aerogammaspektrometrie. Beiträge zur Geologie der Schweiz, Geophysik Nr. 23, Schweizerische Geophysikalische Kommission, 1991.

5 Previous reports

Schwarz, G. F., Klingelé, E. E., Rybach, L.: Aeroradiometrische Messungen in der Umgebung der schweizerischen Kernanlagen. Bericht für das Jahr 1989 zuhanden der Hauptabteilung für die Sicherheit der Kernanlagen (HSK). Interner Bericht, Institut für Geophysik, ETH Zürich, 1990.

Schwarz, G. F., Klingelé, E. E., Rybach, L.: Aeroradiometrische Messungen in der Umgebung der schweizerischen Kernanlagen. Bericht für das Jahr 1990 zuhanden der Hauptabteilung für die Sicherheit der Kernanlagen (HSK). Interner Bericht, Institut für Geophysik, ETH Zürich, 1991.

Schwarz, G. F., Klingelé, E. E., Rybach, L.: Aeroradiometrische Messungen in der Umgebung der schweizerischen Kernanlagen. Bericht für das Jahr 1991 zuhanden der Hauptabteilung für die Sicherheit der Kernanlagen (HSK). Interner Bericht, Institut für Geophysik, ETH Zürich, 1992.

Schwarz, G. F., Klingelé, E. E., Rybach, L.: Aeroradiometrische Messungen in der Umgebung der schweizerischen Kernanlagen. Bericht für das Jahr 1992 zuhanden der Hauptabteilung für die Sicherheit der Kernanlagen (HSK). Interner Bericht, Institut für Geophysik, ETH Zürich, 1993.

Schwarz, G. F., Klingelé, E. E., Rybach, L.: Aeroradiometrische Messungen in der Umgebung der schweizerischen Kernanlagen. Bericht für das Jahr 1993 zuhanden der Hauptabteilung für die Sicherheit der Kernanlagen (HSK). Interner Bericht, Institut für Geophysik, ETH Zürich, 1994.

Schwarz, G. F., Rybach, L.: Aeroradiometrische Messungen im Rahmen der Übung ARM94. Bericht für das Jahr 1994 zuhanden der Fachgruppe Aeroradiometrie (FAR). Interner Bericht, Institut für Geophysik, ETH Zürich, 1995.

Schwarz, G. F., Rybach, L.: Aeroradiometrische Messungen im Rahmen der Übung ARM95. Bericht für das Jahr 1995 zuhanden der Fachgruppe Aeroradiometrie (FAR). Interner Bericht, Institut für Geophysik, ETH Zürich, 1996.

Schwarz, G. F., Rybach, L., Bärlocher, C.: Aeroradiometrische Messungen im Rahmen der Übung ARM96. Bericht für das Jahr 1996 zuhanden der Fachgruppe Aeroradiometrie (FAR). Interner Bericht, Institut für Geophysik, ETH Zürich, 1997.

Bucher, B., Rybach, L., Schwarz, G., Bärlocher, C.: Aeroradiometrische Messungen im Rahmen der Übung ARM97. Bericht für das Jahr 1997 zuhanden der Fachgruppe Aeroradiometrie (FAR). Interner Bericht, Institut für Geophysik, ETH Zürich, 1998.

Bucher, B., Rybach, L., Schwarz, G., Bärlocher, C.: Aeroradiometrische Messungen im Rahmen der Übung ARM98. Bericht für das Jahr 1998 zuhanden der Fachgruppe Aeroradiometrie (FAR). Interner Bericht, Institut für Geophysik, ETH Zürich, 1999.

Bucher, B., Rybach, L., Schwarz, G., Bärlocher, C.: Aeroradiometrische Messungen im Rahmen der Übung ARM99. Bericht für das Jahr 1999 zuhanden der Fachgruppe Aeroradiometrie (FAR). Interner Bericht, Institut für Geophysik, ETH Zürich, 2000.

Bucher, B., Rybach, L., Schwarz, G., Bärlocher, C.: Aeroradiometrische Messungen im Rahmen der Übung ARM00. Bericht für das Jahr 2000 zuhanden der Fachgruppe Aeroradiometrie (FAR). Interner Bericht, Institut für Geophysik, ETH Zürich, 2001.

Bucher, B., Rybach, L., Schwarz, G., Bärlocher, C.: Aeroradiometrische Messungen im Rahmen der Übung ARM01. Bericht für das Jahr 2001 zuhanden der Fachgruppe Aeroradiometrie (FAR). Interner Bericht, Paul Scherrer Institut, Villigen, Schweiz, 2002.

Bucher, B., Rybach, L., Schwarz, G., Bärlocher, C.: Aeroradiometrische Messungen im Rahmen der Übung ARM02. Bericht für das Jahr 2002 zuhanden der Fachgruppe Aeroradiometrie (FAR). Interner Bericht, Paul Scherrer Institut, Villigen, Schweiz, 2003.

Bucher, B., Rybach, L., Schwarz, G.: Aeroradiometrische Messungen im Rahmen der Übung ARM03. PSI-Bericht 04-14, ISSN 1019-0643, Paul Scherrer Institut, Villigen, Schweiz, 2004.

Bucher, B., Butterweck, G., Rybach, L., Schwarz, G.: Aeroradiometrische Messungen im Rahmen der Übung ARM04. PSI-Bericht 05-10, ISSN 1019-0643, Paul Scherrer Institut, Villigen, Schweiz, 2005.

Bucher, B., Butterweck, G., Rybach, L., Schwarz, G.: Aeroradiometrische Messungen im Rahmen der Übung ARM05. PSI-Bericht 06-06, ISSN 1019-0643, Paul Scherrer Institut, Villigen, Schweiz, 2006.

Bucher, B., Butterweck, G., Rybach, L., Schwarz, G.: Aeroradiometrische Messungen im Rahmen der Übung ARM06. PSI-Bericht 07-02, ISSN 1019-0643, Paul Scherrer Institut, Villigen, Schweiz, 2007.

Bucher, B., Guillot, L., Strobl, C., Butterweck, G., Gutierrez, S., Thomas, M., Hohmann, C., Krol, I., Rybach, L., Schwarz, G.: International Intercomparison Exercise of Airborne Gammaspectrometric Systems of Germany, France and Switzerland in the Framework of the Swiss Exercise ARM07. PSI-Bericht Nr. 09-07, ISSN 1019-0643, Paul Scherrer Institut, Villigen, Schweiz, 2009.

Bucher, B., Butterweck, G., Rybach, L., Schwarz, G.: Aeroradiometrische Messungen im Rahmen der Übung ARM08. PSI-Bericht Nr. 09-02, ISSN 1019-0643, Paul Scherrer Institut, Villigen, Schweiz, 2009.

Bucher, B., Butterweck, G., Rybach, L., Schwarz, G., Strobl, C.: Aeroradiometrische Messungen im Rahmen der Übung ARM09. PSI-Bericht Nr. 10-01, ISSN 1019-0643, Paul Scherrer Institut, Villigen, Schweiz, 2010.

Bucher, B., Butterweck, G., Rybach, L., Schwarz, G., Mayer, S.: Aeroradiometrische Messungen im Rahmen der Übung ARM10. PSI-Bericht Nr. 11-02, ISSN 1019-0643, Paul Scherrer Institut, Villigen, Schweiz, 2011.

Bucher, B., Butterweck, G., Rybach, L., Schwarz, G., Mayer, S.: Aeroradiometric Measurements in the Framework of the Swiss Exercise ARM11. PSI-Report No. 12-04, ISSN 1019-0643, Paul Scherrer Institut, Villigen, Switzerland, 2012.

Butterweck, G., Bucher, B., Rybach, L., Schwarz, G., Hödlmoser, H., Mayer, S., Danzi, C. Scharding, G.: Aeroradiometric Measurements in the Framework of the Swiss Exercise ARM12. PSI-Report No. 13-01, ISSN 1019-0643, Paul Scherrer Institut, Villigen, Switzerland, 2013.

Butterweck, G., Bucher, B., Rybach, L., Schwarz, G., Hohmann, E., Mayer, S., Danzi, C. Scharding, G.: Aeroradiometric Measurements in the Framework of the Swiss Exercise ARM13. PSI-Report No. 15-01, ISSN 1019-0643, Paul Scherrer Institut, Villigen, Switzerland, 2015.

Butterweck, G., Bucher, B., Rybach, L., Schwarz, G., Hohmann, E., Mayer, S., Danzi, C. Scharding, G.: Aeroradiometric Measurements in the Framework of the Swiss Exercises ARM14 and FTX14. PSI-Report No. 15-02, ISSN 1019-0643, Paul Scherrer Institut, Villigen, Switzerland, 2015.

Butterweck, G., Bucher, B., Rybach, L., Schwarz, G., Hofstetter-Boillat, B., Hohmann, E., Mayer, S., Danzi, C. Scharding, G.: Aeroradiometric Measurements in the Framework of the Swiss Exercises ARM15, GNU15 and the International Exercise AGC15. PSI-Report No. 15-04, ISSN 1019-0643, Paul Scherrer Institut, Villigen, Switzerland, 2015.

Butterweck, G., Bucher, B., Rybach, L., Poretti, C., Maillard, S., Schwarz, G., Hofstetter-Boillat, B., Hohmann, E., Mayer, S., Scharding, G.: Aeroradiometric Measurements in the Framework of the Swiss Exercises ARM16 and LAURA. PSI-Report No. 17-01, ISSN 1019-0643, Paul Scherrer Institut, Villigen, Switzerland, 2017.

Butterweck, G., Bucher, B., Gryc, L., Debayle, C., Strobl, C., Maillard, S., Thomas, M., Helbig, A., Krol, I., Chuzel, S., Couvez, C., Ohera, M., Rybach, L., Poretti, C., Hofstetter-Boillat, B., Mayer, S., Scharding, G.: International Intercomparison Exercise of Airborne Gamma-Spectrometric Systems of the Czech Republic, France, Germany and Switzerland in the Framework of the Swiss Exercise ARM17. PSI-Report No. 18-04, ISSN 1019-0643, Paul Scherrer Institut, Villigen, Switzerland, 2018.

Butterweck, G., Bucher, B., Rybach, L., Poretti, C., Maillard, S., Schindler, M., Hofstetter-Boillat, B., Mayer, S., Scharding, G.: Aeroradiometric Measurements in the Framework of the Swiss Exercises ARM18 and the International Exercise CONTEX 2018. PSI-Report No. 19-01, ISSN 1019-0643, Paul Scherrer Institut, Villigen, Switzerland, 2019.

Butterweck, G., Bucher, B., Rybach, L., Poretti, C., Maillard, S., Schindler, M., Hofstetter-Boillat, B., Mayer, S., Scharding, G.: Aeroradiometric Measurements in the Framework of the Swiss Exercise ARM19. PSI-Report No. 20-01, ISSN 1019-0643, Paul Scherrer Institut, Villigen, Switzerland, 2020.

The reports since 1994 can be found and downloaded from the FAR website `https://far.ensi.ch`.

6 Evaluation parameters

The parameters used for data evaluation are stored in the header section of each generated ERS 2.0 file. The header section used in the current exercise is listed below.

```
V 2.0
HSW AGS_CH_V0.0
/* Parameters used for data evaluation-------------------------------------------------------------------------------
/* No data value;MND -999
/* Energy calibration;ISE0 0;ISE1 3;ISE2 0
/* Energy windows--------------------------------------------------------------------------------------------------
ISW Total;ISWE1_Total 401;ISWE2_Total 2997;ISWB_Total 78.2;ISWC_Total 5.55;ISWT_Total 0.006;ISWRA_Total 0;ISWRB_Total 0
ISW K-40;ISWE1_K-40 1369;ISWE2_K-40 1558;ISWB_K-40 6.3;ISWC_K-40 0.30;ISWT_K-40 0.008;ISWRA_K-40 0;ISWRB_K-40 0
ISW U-238;ISWE1_U-238 1664;ISWE2_U-238 1853;ISWB_U-238 3.6;ISWC_U-238 0.23;ISWT_U-238 0.0055;ISWRA_U-238 0;ISWRB_U-238 0
ISW Th-232;ISWE1_Th-232 2407;ISWE2_Th-232 2797;ISWB_Th-232 0.0;ISWC_Th-232 0.28;ISWT_Th-232 0.006;ISWRA_Th-232 0;ISWRB_Th-232 0
ISW Cs-137;ISWE1_Cs-137 600;ISWE2_Cs-137 720;ISWB_Cs-137 12.5;ISWC_Cs-137 0.58;ISWT_Cs-137 0.01;ISWRA_Cs-137 0;ISWRB_Cs-137 0
ISW Co-60;ISWE1_Co-60 1100;ISWE2_Co-60 1400;ISWB_Co-60 7.1;ISWC_Co-60 0.65;ISWT_Co-60 0.008;ISWRA_Co-60 0;ISWRB_Co-60 0
ISW MMGC1;ISWE1_MMGC1 400;ISWE2_MMGC1 1400;ISWB_MMGC1 0;ISWC_MMGC1 0;ISWT_MMGC1 0.006;ISWRA_MMGC1 0;ISWRB_MMGC1 0
ISW MMGC2;ISWE1_MMGC2 1400;ISWE2_MMGC2 2997;ISWB_MMGC2 0;ISWC_MMGC2 0;ISWT_MMGC2 0.0065;ISWRA_MMGC2 0;ISWRB_MMGC2 0
ISW LOW;ISWE1_LOW 100;ISWE2_LOW 400;ISWB_LOW 0;ISWC_LOW 0;ISWT_LOW 0.02;ISWRA_LOW 0;ISWRB_LOW 0
ISW MID;ISWE1_MID 720;ISWE2_MID 2997;ISWB_MID 0;ISWC_MID 0;ISWT_MID 0.015;ISWRA_MID 0;ISWRB_MID 0
ISW SDI;ISWE1_SDI 240;ISWE2_SDI 2997;ISWB_SDI 51.4;ISWC_SDI 4.19;ISWT_SDI 0.0053;ISWRA_SDI 0;ISWRB_SDI 0
/* Stripping factors------------------------------------------------------------------------------------------------
ISWS_U-238_K-40 0.931
ISWS_Th-232_K-40 0.478
ISWS_Co-60_K-40 0.067
ISWS_Th-232_U-238 0.362
ISWS_U-238_Th-232 0.049
ISWS_K-40_Cs-137 0.450
ISWS_U-238_Cs-137 3.161
ISWS_Th-232_Cs-137 1.654
ISWS_Co-60_Cs-137 0.154
ISWS_K-40_Co-60 0.758
ISWS_U-238_Co-60 2.370
```

```
ISWS_Th-232_Co-60 0.684
/* Conversion factors--------------------------------------------------------------------------
ISWA_AW_K-40 5.58
ISWA_AW_U-238 3.57
ISWA_AW_Th-232 1.22
ISWA_AW_Cs-137 1.02
ISWA_AA_Cs-137 17.8
ISWA_AP_Cs-137 2511000
ISWA_AP_Co-60 1505000
ISD_SDI 5.65E-08
ISWD_K-40 0.000289
ISWD_U-238 0.00197
ISWD_Th-232 0.000971
ISWD_Cs-137 0.000191
/* Corrections and additional Identifiers-------------------------------------------------------------------
/* Topographic correction;MTC Y
/* Radon correction;MRC N
/* Definition of additional Identifiers for corrected altitude and ground clearance and an indicator for a new flight
DEFINE&PZ_korr Corrected altitude im m; DEFINE&PH_korr Corrected ground clearance in m
DEFINE&New_Flight Switch for data composed of several flights
/*
/*
```